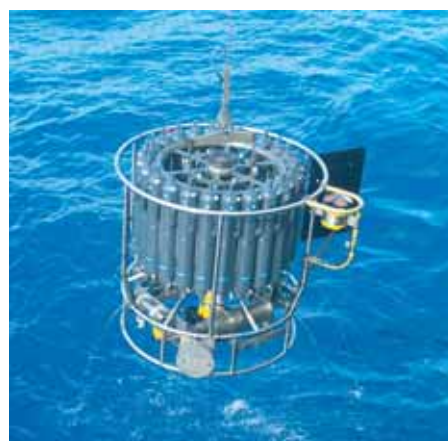# Extreme Climate Events
and Euro-Atlantic Atmospheric Blocking
in Present and Future Climate Model Simulations

Jana Sillmann

Hinweis

Die Berichte zur Erdsystemforschung werden vom Max-Planck-Institut für Meteorologie in Hamburg in unregelmäßiger Abfolge herausgegeben.

Sie enthalten wissenschaftliche und technische Beiträge, inklusive Dissertationen.

Die Beiträge geben nicht notwendigerweise die Auffassung des Instituts wieder.

Die "Berichte zur Erdsystemforschung" führen die vorherigen Reihen "Reports" und "Examensarbeiten" weiter.

Notice

The Reports on Earth System Science are published by the Max Planck Institute for Meteorology in Hamburg. They appear in irregular intervals.

They contain scientific and technical contributions, including Ph. D. theses.

The Reports do not necessarily reflect the opinion of the Institute.

The "Reports on Earth System Science" continue the former "Reports" and "Examensarbeiten" of the Max Planck Institute.

Extreme Climate Events
and Euro-Atlantic Atmospheric Blocking
in Present and Future Climate Model Simulations

Dissertation zur Erlangung des Doktorgrades der Naturwissenschaften
im Departement Geowissenschaften der Universität Hamburg
vorgelegt von

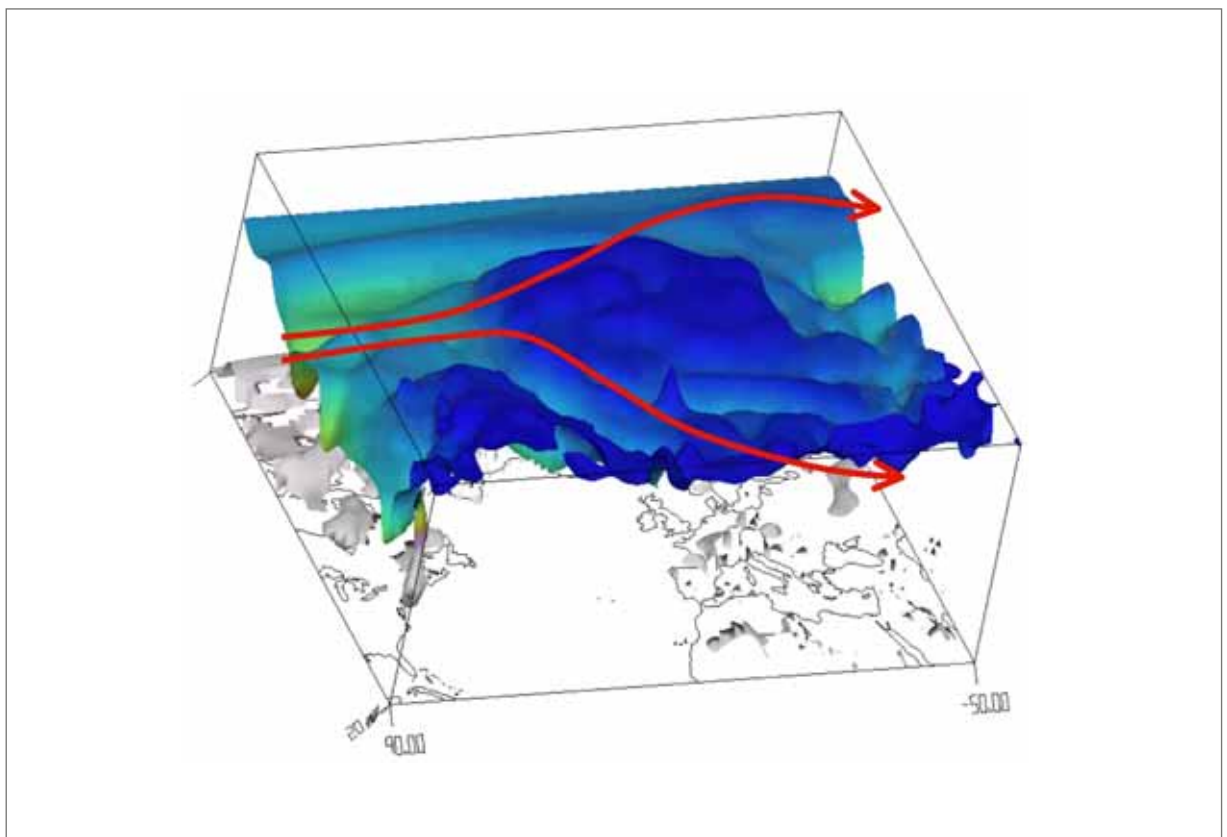## Jana Sillmann

aus Bad Salzungen

Hamburg 2008

Jana Sillmann
Max-Planck-Institut für Meteorologie
Bundesstrasse 53
20146 Hamburg
Germany

Als Dissertation angenommen
vom Department Geowissenschaften der Universität Hamburg

auf Grund der Gutachten von
Prof. Dr. Guy Brasseur
und
Dr. Erich Roeckner

Hamburg, den 30. Januar 2009
Prof. Dr. Jürgen Oßenbrügge
Leiter des Departments für Geowissenschaften

Extreme Climate Events
and Euro-Atlantic Atmospheric Blocking
in Present and Future Climate Model Simulations

Jana Sillmann

Hamburg 2008

All models are wrong, but some are useful.
George Edward Pelham Box (1976)

Abstract

The study focuses on the analysis of the occurrence and changes of extreme temperature and precipitation events in global climate simulations of the present and future climate. Two approaches are followed to identify and analyze these extreme events in data of the global climate model ECHAM5/MPI-OM.

First, indices for extreme events, which capture moderate and statistical robust extreme events, are calculated on the basis of model data and are compared with indices from the global observational dataset HadEX. This comparison shows that the model is able to realistically capture the observed climatological large-scale patterns of the extreme indices, although the quality of the simulations depends on the index and region under consideration. In the future climate, as represented by the IPCC emission scenarios B1 and A1B, all considered temperature-based indices (yearly minimum and maximum temperatures and frequency of tropical nights) encounter a significant increase worldwide. The precipitation-based indices (max. 5-day precipitation amount and 95th percentile of precipitation) also increase significantly, particularly in those regions that are relatively wet already in present climate. Analogously, dry spells increase especially in regions with dry conditions under present climate. The future changes of the indices reveal distinct regional and seasonal patterns as shown exemplarily in three European regions.

Further, it is investigated whether the occurrence of extreme events and their changes in a warming climate are related to large-scale circulation patterns. This study particularly concentrates on the influence of Euro-Atlantic atmospheric blocking on extreme events in Europe. First, it is analyzed how well the model is able to represent blocking conditions in summer and winter by comparing blocking frequencies and their spatial and seasonal distributions with ERA-40 re-analysis data. Secondly, correlations between blocking frequency and selected monthly indices for extreme events are calculated. Blocking frequencies and their seasonal distribution are well captured by the model and especially for the winter minimum temperature significant correlations with blocking events are found in central Europe. In the future climate, the blocking frequency is slightly diminished but the influence on the European winter climate remains robust.

The second approach to identify extremes in global model data concentrates on the statistical modeling of extreme values. Here, the Generalized Extreme Value distribution (GEV) is fitted to monthly minima (maxima) of winter minimum (maximum) temperatures in Europe. The behavior of the distribution's parameters and 20-year return values are analyzed for present and future climate conditions. Compared to the extreme indices, similar regional warming patterns in Europe can be found in the A1B scenario. Finally, an attempt is made to improve the fit of the GEV by conditioning the parameters on a covariate derived from Euro-Atlantic atmospheric blocking. It is demonstrated that including atmospheric blocking as covariate improves the GEV fit particularly to the minimum temperature data in certain regions of Europe. This has also considerable impact on the return values.

Contents

List of Figures

List of Tables

Chapter 1

Introduction

1.1 Motivation

Extreme events occur within the natural variability of the climate (IPCC (2007)). However, events like the hurricane Katrina of 2005 in southeastern U.S.A., the heat wave of 2003 in central Europe, or the Elbe flood of 2002 in central and eastern Europe have demonstrated how susceptible our present society is to the destructiveness of such extreme events and how climate can produce conditions that are outside the coping range of our society (McGregor et al. (2005)). Statistics of insurances (e.g., MunichRe (2002)) have further illustrated that the costs of damages due to extreme climate events have exponentially risen in the last decades. This statistic is, however, strongly related to higher technology standards and higher population densities in risk-prone areas compared to past decades and to a corresponding rise in insured infrastructure (Beniston & Stephenson (2004)). Thus, this statistic does not indicate whether extreme climate events have increased due to anthropogenic climate change. Hence, the scientific study of the nature of extreme climate events is essential to gain an understanding of their possible occurrence and dimensions in present and future climate. The knowledge gained can enable us to develop reliable prediction methods as well as adaptation and mitigation strategies to avoid unnecessary human and financial losses.

1.2 Extreme climate events - a general introduction

A unique definition of an extreme event is difficult to formulate (e.g., Beniston & Stephenson (2004)). In general we can characterize an extreme event as a very seldom (as rare as or rarer than the 10th or 90th percentile of the observed probability density function according to IPCC (2007)) and very intense event with severe impacts on society and biophysical systems. The severity of a particular extreme event, however, highly depends on the vulnerability and adaptability of the system under consideration (Meehl et al. (2000)).

In particular, an extreme climate event can be classified as a pattern of extreme
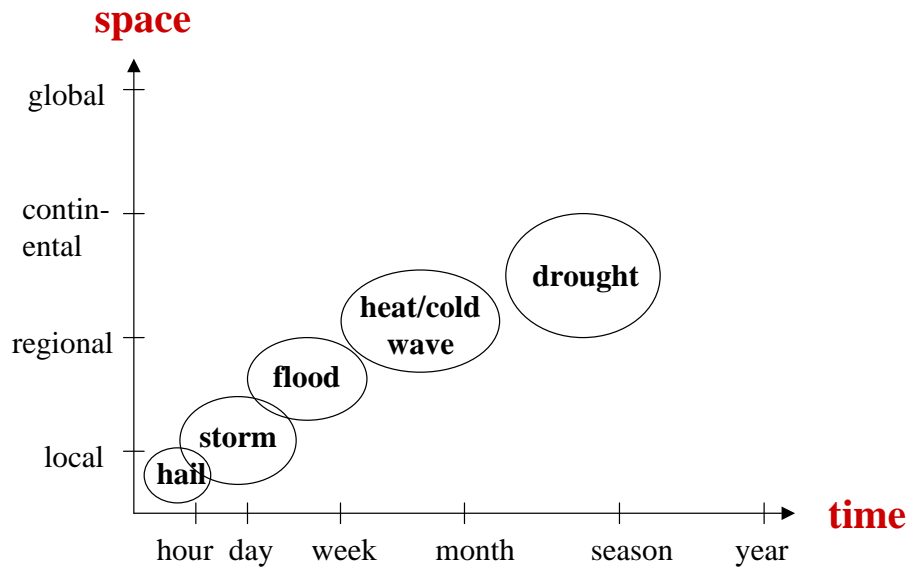
Figure 1.1— Spatial and temporal scale of extreme climate events

weather that persists for some time, especially if it yields an average or total that is itself extreme (e.g., drought or heavy rainfall over several days or a season) (IPCC (2007)). Extreme climate events can occur on different spatial and temporal scales as illustrated in figure 1.1 and can involve one or more climate variables (e.g., temperature, precipitation, wind, etc.), which define their complexity. Due to the fact that extreme events are scarce, we need long data records to analyze their characteristics and possible changes in a warming climate. Single extreme events cannot be simply and directly attributed to anthropogenic climate change, since there is always the finite chance that the considered event could have occurred naturally (IPCC (2007)). Further, the more scarce the event, the more difficult it is to identify long-term changes.

Observational datasets would be an optimal basis for the analysis of extreme events. However, observed temperature and precipitation data records are in the most cases too short, do not uniformly cover the whole planet and suffer from inhomogeneities, e.g., due to changes in observing practices. These limitations make it difficult to use observational datasets for a global or even regional study of extreme events (IPCC (2007)). To circumvent the aforementioned limitations, we can make use of long present and future climate simulations from a state-of-the-art global atmosphere-ocean coupled general circulation model (CGCM). The fast development of CGCMs in the last decades regarding their complexity and resolution as well as the inclusion of more and more physical processes makes them a fundamental tool for studying various aspects of the climate. The current resolution of a CGCM as used e.g., for the Forth Assessment Report of the Intergovernmental Panel on Climate Change (IPCC AR4) (IPCC (2007)) corresponds to a grid box size of approximately 200km (mid-latitudes). This model resolution allows us to

study particularly large-scale climate extreme events of a single or more climate variables, such as floods, heat and cold waves as well as droughts (see also figure 1.1). Small-scale extreme weather events (such as hail or storms) cannot be resolved by a CGCM with the described resolution. To assess these events, regional climate models and statistical downscaling methods can be applied (see e.g., Beniston et al. (2007); Friederichs & Hense (2007); Leckebusch et al. (2006); Woth et al. (2006); Katz et al. (2002); Wilby et al. (1998)).

1.3 Assessment of extreme events in climate data

A particular interest in the study of extreme climate events arose not more than two decades ago (e.g., Mearns et al. (1984); Katz & Brown (1992); Karl et al. (1993)). At that time also the discussion awoke how to assess extreme climate events in climate data and how to make the results comparable for different regions, models, and climate change simulations.

Basically, there exist two approaches, a parametric and a non-parametric, for the diagnostic analysis of extreme events in climate data. The non-parametric approach is established by the definition of indices for extreme events that characterize moderate and statistical robust extreme events with short return periods (Karl et al. (1999)). Subsequently, the Expert Team on Climate Change Detection Monitoring and Indices developed a set of 27 indices based on daily minimum and maximum temperature and precipitation data (Peterson (2005)). Various studies have been accomplished with a selection of these indices using observational data (e.g., Frich et al. (2002); Klein Tank & Koennen (2003)) or climate model simulations (e.g., Alexander et al. (2006); Sillmann & Roeckner (2008)). This approach made it further possible to quantitatively analyze moderate extreme events in future climate model simulations and to perform model inter-comparison studies (Tebaldi et al. (2006)) as well as compare model results with observations (e.g., Kiktev et al. (2003); Sillmann & Roeckner (2008)). However, this approach only considers absolute extreme values and lacks the ability to extrapolate the results towards damage-relevant extremes with much larger return periods than those observed (Frei (2003)).

The parametric approach based on the extreme value theory, in fact, enables such extrapolation of extreme events with long return periods and allows studies considering all features of the extreme's distribution. The extreme value theory goes back to the extremal limit theorem of Fisher & Tippett (1928), which states that the distribution of the maxima (or minima) of a sample of random variables approaches one of three limiting forms as sample size increases. Gnedenko (1943) has defined this theorem in full generality. Gumbel (1958) was then one of the first promoting the extreme value theory as a tool for modeling the extremal behavior of observed physical processes. Leadbetter et al. (1983) further achieved some great advances of the applicability of extreme value techniques by extending the extreme value theory to non-stationary processes and broadening the characterization of the extremal behavior. A detailed description of various methods regarding the

statistical modeling of extreme events is given in, e.g., Palutikof et al. (1999); Coles (2001); Katz et al. (2002).

The classical extreme value theory is based on the block maxima approach, where the maxima (or minima) of a given a sample of random variables (e.g., temperature, precipitation, or wind speed) are drawn from intervals (blocks) of distinct length (e.g., month, season, year). The distribution of these maxima or minima asymptotically converges to the Generalized Extreme Value (GEV) distribution as block length goes to infinity. The advantage of this approach is its fairly straightforward application requiring only a few decisions during parameter calculation (Palutikof et al. (1999)).

Another approach making more efficient use of the available data is based on threshold models where the distribution of maxima or minima that exceed some high threshold (e.g., Peaks Over Threshold (POT) approach) converge to a family of distribution called Generalized Pareto Distribution (GPD) (Coles (2001)). In practice, some drawbacks are however associated with the threshold models making it difficult to apply those to large (spatial extension) climate data sets. The difficulties concern the lack of reliable or recommendable automatic techniques for threshold selection (Davison & Smith (1990); Palutikof et al. (1999)) and also the trade-off between choosing the threshold high enough, but still ensuring a large enough number of exceedances for a reliable parameter estimation (Katz et al. (2005)). Furthermore, climate variables such as temperature exhibit clustering that has to be taken care of even for high thresholds (Coles (2001)).

In recent years, the idea of including covariates in the extreme value distribution evolved to improve the statistical modeling of extreme values (e.g., Coles (2001); Katz et al. (2002, 2005)). So far, only a few studies in climate research followed this approach, which concentrate yet exclusively on a time trend as covariate to take into account anthropogenic climate change in the simulation of extreme temperature and precipitation events (e.g., Kharin & Zwiers (2000, 2005); Nogaj et al. (2007)).

Katz et al. (2002) however points out that the GEV distribution can be regarded as valuable method for statistical downscaling of extreme values in CGCM data if one can find one or more appropriate covariate(s) arising from large-scale circulation variables (e.g., mean sea level pressure, sea surface temperature, or potential vorticity, etc.). Thus, finding appropriate covariates remains a challenge in climate research.

1.4   Atmospheric blocking and its connection with extreme climate events focusing on Europe

According to Corti et al. (1999) most atmospheric changes are attributable to changes in the frequency of the global atmospheric flow regimes. In various recent studies, it has also been presumed (e.g., Klein Tank & Koennen (2003); Haylock & Goddess (2004); Cassou et al. (2005)) that large-scale circulation patterns have an influence on the occurrence and distribution of extreme events. State-of-the-art

CGCMs, and in particular the ECHAM5/MPI-OM (Jungclaus et al. (2006)), perform well in simulating large-scale atmospheric variables as a study of Van Ulden & van Oldenborgh (2006) points out. Consequently, it is of major concern to use this skill of the CGCMs to explore the nature of extreme climate events and to improve their prediction by investigating their link to large-scale atmospheric conditions (Yiou et al. (2007)).

The European climate strongly depends on the atmospheric circulation, in particular the alternation between westerlies bringing moist maritime air from the Atlantic to the European continent and the easterlies being responsible for dry and cold (warm) weather in winter (summer) (Van Ulden & van Oldenborgh (2006)). In this respect atmospheric blocking plays a key role in the European flow variability due to its capability to disturb predominant cyclonic westerly flow. Atmospheric blocking conditions are in general defined as anti-cyclonic quasi-stationary high-pressure systems persisting for several days up to weeks. They act as an important counterpart to the North Atlantic Oscillation (NAO) (Cassou et al. (2004); Terray et al. (2004); Yiou & Nogaj (2004)) and explain approximately 15% of the European climate variability (Scherrer et al. (2006)). Concerning its large spatial extent and long temporal existence, atmospheric blocking has an ample influence on the seasonal winter climate in Europe (e.g., Beniston et al. (1994); Lupo et al. (1997)). In winter, atmospheric blocking can be responsible for anomalous dry and cold weather conditions at its core (Tyrlis & Hoskins (2008)) and wet conditions around the block (Trigo et al. (2004); Rex (1950a)).

Pioneer work, concerning a detailed climatology of blocking frequency and deriving a subjective detection method for blocking occurrence, has been done by Elliott & Smith (1949) and Rex (1950a,b). Most subjective detection methods are based on the latitudinal (1D) or latitudinal and longitudinal (2D) gradient of the absolute (e.g., Tibaldi & Molteni (1990); Lupo & Smith (1995)) or anomaly field (e.g., Shukla & Mo (1983); Sausen et al. (1995)) of the geopotential height at 500 hPa (Z500). However, blocking indicators based on geopotential height are not able to capture the dynamical features of atmospheric blocking, thus making model validation difficult (Doblas-Reyes et al. (2002)).

Recently, blocking indicators based on dynamical variables, such as potential temperature or potential vorticity have been developed (Tyrlis & Hoskins (2008); Pelly & Hoskins (2003b)). According to Schwierz et al. (2004), a dynamical-based index should be consistent with the intrinsic blocking features, such as spatial scale and structure, amplitude, life cycle, duration, movement as well as geographical location. A quasi three-dimensional approach to capture all of these features is the dynamical blocking indicator based upon the potential vorticity (PV) anomaly field averaged over the tropopause level (2 pvu) between 500 and 150hPa (Schwierz et al. (2004); Croci-Maspoli et al. (2007b)).

Figure 1.2 illustrates the basic concept (following the dynamical approach) of a blocked situation at a specific time over the Euro-Atlantic region where the colored (green to blue) surface represents the height of the dynamical tropopause. Dark
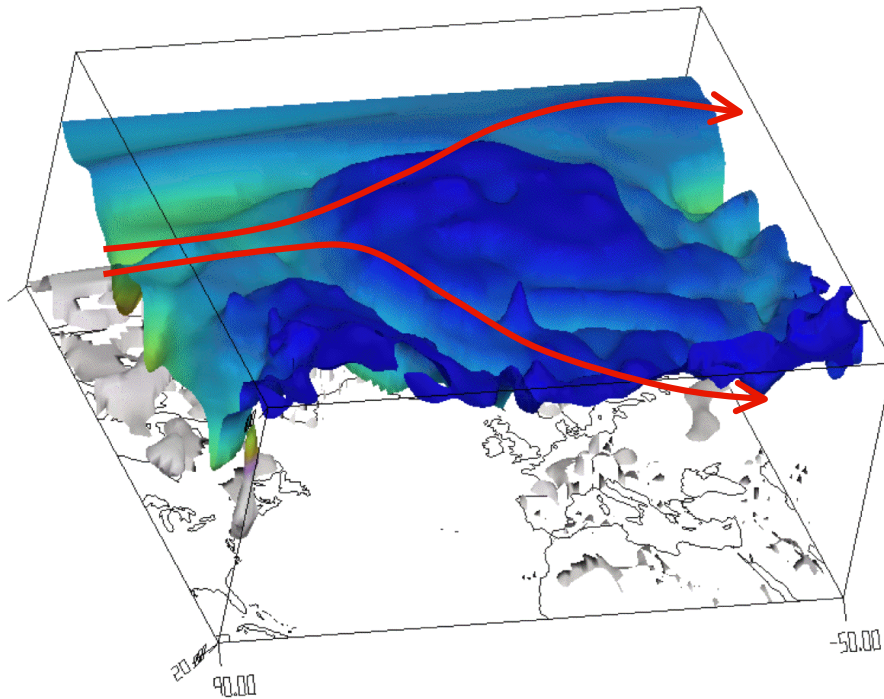
Figure 1.2— Example of an Euro-Atlantic atmospheric blocking situation (January 23th, 1987 00UTC) (Croci-Maspoli (2005)). Please find a detailed description in the text.

blue regions indicate an elevation of the tropopause aligned with strong negative PV-anomalies (PV < -1.3 pvu). Thus, the westerly flow, indicated by the red arrows, is blocked and changes its path to the north and south of the blocked region resulting in a more cellular flow with a significant meridional component. The dynamical blocking detection method by Schwierz et al. (2004) tracks these negative PV-anomalies from their genesis to their lysis, requiring a minimum lifetime of 5 days and a spatial extension of at least $1.8 \cdot 10^6$ km^2. Consequently, this blocking indicator is beneficial for blocking life time studies, model validations, and allows further insight in the dynamics of blocking events in climate change experiments.

1.5   Scope of the thesis

The scope of this dissertation is the assessment of large-scale extreme temperature and precipitation events by different methods as described in section 1.3. The focus lies primarily on the analysis of CGCM data, in particular on climate simulations performed with the ECHAM5/MPI-OM of the Max Planck Institute for Meteorology, Hamburg (Roeckner et al. (2006a)). Furthermore, this thesis aims to introduce a method of including information about a large-scale atmospheric pattern, namely atmospheric blocking, in the statistical modeling of extreme temperature events. The following aspects will be addressed in the thesis:

- Is the model able to realistically represent extreme climate events in the present climate?

- What changes regarding extreme climate events can we expect under anthropogenic climate change in future climate model simulations?

- Are there regional and seasonal differences attached to the changes in extreme events under anthropogenic climate change?

- Can we find associations between large-scale atmospheric circulation patterns, in particular atmospheric blocking, and present and future climate extreme events?

- Do these associations change under anthropogenic climate change?

- Can we use the associations between large-scale atmospheric circulation patterns and climate extremes for improvement of the statistical modeling of extreme values?

1.6 Thesis outline

The thesis is structured in 3 chapters (besides the general introduction and summary), each addressing a subset of the questions mentioned above. One chapter is already published, one is submitted and the other one is in preparation for publication. Thus, each chapter forms a largely independent study with a corresponding introduction as well as a model and methodology description section, but with some reference to the previous chapters concerning the results. This structure implies a partial overlap of some contents between the chapters.

Chapter 2 concentrates on the non-parametric approach by assessing extreme events in climate model data with indices for climate extremes. It mainly addresses the question whether the model can represent observed extreme temperature and precipitation events and how extreme events change globally in future climate model simulations. Also regional and seasonal differences are analyzed with focus on Europe. This chapter has been published in *Climatic Change*[1].

Chapter 3 deals with the associations between Euro-Atlantic atmospheric blocking and extreme temperature and precipitation events in Europe. Associations are studied by means of composite maps and correlation analysis. This chapter is submitted to *Geophysical Research Letters*[2]

---

[1]Sillmann, J. and E. Roeckner, 2008, Indices of extreme events in projections of anthropogenic climate change, Climatic Change, 86:83-104.

[2]Sillmann, J. and M. Croci-Maspoli, 2008, Euro-Atlantic blocking and extreme events in present and future climate simulations, submitted to Geophysical Research Letters.

Chapter 4 comprises the statistical modeling of extreme temperature events in present and future climate model simulations. This chapter also concentrates on Europe. An attempt of statistical downscaling is made by including Euro-Atlantic atmospheric blocking as covariate in the GEV distribution, which is fitted to the CGCM data. This chapter is in preparation for submission to *Climate Dynamics* with M. Kallache and M. Croci-Maspoli as co-authors.

Chapter 5 summarizes the results from the previous chapters by answering the questions mentioned in section 1.5. Furthermore, the main findings of this thesis are concluded and an outlook is given for further research.

Chapter 2

Indices for extreme events in projections of anthropogenic climate change[1]

Abstract

Indices for temperature and precipitation extremes are calculated on the basis of the global climate model ECHAM5/MPI-OM simulations of the 20th century and SRES A1B and B1 emission scenarios for the 21st century. For model evaluation, the simulated indices representing the present climate were compared with indices based on observational data. This comparison shows that the model is able to realistically capture the observed climatological large-scale patterns of temperature and precipitation indices, although the quality of the simulations depends on the index and region under consideration. In the climate projections for the 21st century, all considered temperature-based indices, yearly minimum (maximum) of the minimum (maximum) temperature and the frequency of tropical nights, show a significant increase worldwide. Similarly, extreme precipitation, as represented by the maximum 5-day precipitation and the 95th percentile of precipitation, is projected to increase significantly in most regions of the world, especially in those that are relatively wet already under present climate conditions. Analogously, dry spells increase particularly in those regions that are characterized by dry conditions in present-day climate. Future changes in the indices exhibit distinct regional and seasonal patterns as identified exemplarily in three European regions.

---

[1]published in *Climatic Change*, 2008, with E. Roeckner as co-author.

2.1 Introduction

Nowadays a major worry of mankind is anthropogenic climate change and its socioeconomic impacts. Global surface temperature has significantly risen during the last century and will continue to rise unless greenhouse gas emissions are drastically reduced (IPCC (2001)). The impacts of climate change are manifold and vary regionally, even locally, in their severity. However, immediate damages to humans and their properties are not obviously caused by gradual changes in temperature or precipitation but mainly by so-called extreme climate events. The rare occurrence of extremes makes it necessary to investigate long data records to determine significant changes in the frequency and intensity of extreme events. To this end, coupled atmosphere-ocean general circulation models (AOGCMs) are appropriate tools to simulate past, present, and future climate states. Thus, AOGCMs are able to generate long time series that can be used for model evaluation and also for analyses of possible future changes in extreme events.

There are various methods to characterize extreme events, for instance by means of percentile-, threshold- or duration-based indices, or by analyzing the statistical behavior of the tail of a weather element's probability distribution. The focus of this study is on the non-parametric approach. Indices for climate extremes based on daily temperature and precipitation data were defined by an international committee to assess extremes in temperature and precipitation and to make a global and multi-model comparison possible (Folland et al. (1999); Karl et al. (1999); Nicholls & Murray (1999)). Frich et al. (2002) defined ten key indices, which should be statistically robust with fairly short return periods and represent a wide variety of climate aspects. Several studies subsequently focused on the analysis of this set of key indices. However, the definitions and usefulness of some of these indices, although meant to be globally valid, became the subject of discussion and, as a result, definitions of some indices as well as their calculations were reconsidered (Alexander et al. (2006); Zhang et al. (2005); Tebaldi et al. (2006); Kiktev et al. (2003); Haylock & Goddess (2004), etc.). Several studies to date have concentrated on the analysis of indices for climate extremes based on observational data from weather stations (e.g., Frich et al. (2002); Klein Tank & Koennen (2003)), while others focused primarily on the changes of extremes in future climate projections (e.g., Meehl et al. (2000); Meehl & Tebaldi (2004); Tebaldi et al. (2006)).

The objectives of the present study are, first, to investigate whether the model is able to capture the observed spatial and temporal patterns of extreme temperature and precipitation events and, second, to analyze the changes of extreme indices in future climate projections. The paper is organized as follows. The model and the experiments are briefly described in section 2.2, followed by a discussion of the climate indices selected for this study in section 2.3. The results are presented in section 2.4, which has two parts. In sub-section 2.4.1 the simulated indices are compared with the observed ones, whilst the changes obtained in future climate projections are presented in sub-section 2.4.2. A discussion of the main results in section 2.5 concludes this paper.

2.2   Model description and experiments

All model-based indices described in this paper were calculated from data generated with the coupled AOGCM ECHAM5/MPI-OM developed at the Max Planck Institute for Meteorology (Jungclaus et al. (2006)). The atmospheric component ECHAM5 (Roeckner et al. (2003)) has a horizontal resolution of 63 wave numbers in spectral space (T63), corresponding to $1.875°$x$1.875°$ in grid-point space, and 31 vertical levels. The oceanic component of the coupled model (MPI-OM) is a GCM with integrated sea ice model (Marsland et al. (2003)). It has a nominal horizontal resolution of $1.5°$ and 40 vertical levels. The coupled model does not employ flux adjustments.

The model experiments analyzed in this study include a 500-year pre-industrial control run (CON), three 20th century simulations (20C) initialized at different states of CON, and three realizations of the IPCC scenarios A1B and B1, respectively, initialized at year 2000 of the respective 20C experiments. In CON, the greenhouse gas concentrations were kept constant at levels for the year 1860 and anthropogenic sulfate aerosols were set to zero. In the 20C runs, greenhouse gases (CO_2, CH_4, N_2O, CFCs, O_3) and sulfate aerosols were prescribed year to year according to observations and chemical transport model results, respectively. In the future scenario experiments, greenhouse gas and sulfate aerosol concentrations were prescribed year to year according to the scenarios A1B and B1 in the Special Report on Emissions Scenarios (SRES) (Nakicenovic & Swart (2000)) of the Intergovernmental Panel on Climate Change (IPCC). A1B is the part of the A1 family that describes a balance across all energy sources, resulting in a total radiative forcing of about 6 Wm^{-2} in year 2100 compared to pre-industrial times (IPCC (2001)). B1 describes a storyline with rapid changes in economic structures toward a service and information economy with reductions in material intensity and the introduction of clean and resource-efficient technologies, resulting in a total radiative forcing of about 4 Wm^{-2} in year 2100 (IPCC (2001)).

2.3   Methodology

Daily 2-meter maximum and minimum temperature (T2MAX and T2MIN, respectively) as well as precipitation data were used to calculate 27 indices for climate extremes as defined by the Expert Team on Climate Change Detection Monitoring and Indices (ETCCDMI), which is jointly sponsored by the World Meteorological Organization (WMO) Commission of Climatology (CCl) and the Climate Variability and Predictability (CLIVAR) project (Peterson (2005)). An excerpt of these indices can be seen in Table 2.1. CLIVAR also provided the basic computer software used for the calculation of these indices (FclimDex), which was modified for the needs of gridded climate model data. The threshold-based indices that have to be calculated relative to a base period were calculated according to the bootstrap method outlined by Zhang et al. (2005).

All indices mentioned in this paper were calculated on an annual basis for the three ensemble members and ensemble means of the 20C and the scenario simulations, respectively. Additionally, some of the model-based indices were calculated on a monthly basis (cf. section 2.4.3). For the comparison of the 20C model runs with observations, we used the indices for climate extremes based on data from worldwide weather observation stations as described in Alexander et al. (2006). The Hadley Centre for Climate Prediction and Research provides these indices on an annual basis for the time period 1951-2003 and gridded to a spatial resolution of $3.75°$ longitude by $2.5°$ latitude (HadleyCentre (2006)). Those indices will be referred to as HadEX indices in the following. It is important to note that all observation-based indices were first calculated for all weather stations and then interpolated onto the latitude-longitude grid, whereas the model-based indices were calculated from the variables representative for the whole grid-box area. These methodological differences are likely to cause systematic differences in the probability distribution of spatially inhomogeneous data such as precipitation, for example.

The present analysis is limited to a few key indices (indicated in bold letters in Table 1). The selection was based on the following criteria. The indices should be robust and plausible considering the comparably coarse model resolution and the information deducible from the indices should be useful for climate change impact studies. The minimum T2MIN (TNn) and maximum T2MAX (TXx) as well as the number of tropical nights (TR) represent the temperature indices for climate extremes in this paper. TNn and TXx correspond to the absolute temperature extremes within a year. Tropical nights are defined as days with T2MIN greater than $20°C$. TR was chosen to provide information about possible heat stress for organisms. During heat wave events, higher nighttime temperatures can increase the heat stress experienced by organisms. An increase in the frequency of tropical nights could thus be an indicator for more heat stress.

The selected key indices for precipitation are the maximum 5-day precipitation amount during a year (RX5day), the 95th percentile of precipitation on wet days (R95p), and the number of consecutive dry days during a year (CDD). Days with precipitation above (below) 1mm are defined as wet (dry) days, respectively. For spell indices (in Table 2.1 marked with a *), such as CDD and consecutive wet days (CWD), it has to be mentioned that if a spell lasts longer than a year, it is counted against the year in which the spell ends. RX5day can be used as a flood indicator because severe floods, on the space scales considered here, are generally not caused by a single heavy thunderstorm event, but more likely, by long-lasting heavy precipitation events that are extended over a large region. R95p characterizes the upper tail of the precipitation distribution. CDD is the only index that refers to the dry part of the year and can indicate regions vulnerable to droughts. Real drought conditions, however, are caused by more complex conditions than captured by CDD, e.g. interactions of precipitation deficits as well as soil and land use characteristics (Tebaldi et al. (2006)). The selected key indices were also chosen by Alexander et al. (2006); Tebaldi et al. (2006); Kiktev et al. (2003); Easterling et al. (1997), and Karl et al. (1993), thus enabling a comparison with their results.

2.4   Results

2.4.1   Comparison of model- and observation-based indices for extreme events

The comparison of model- and observation-based indices was carried out on the basis of global maps and 53-year time series (1951-2003). First, the model-based indices were interpolated onto the Hadley Center HadCM3 model grid (3.75° x 2.5°, 96 x 73 grid boxes). Furthermore, the time-dependent mask of missing grid values in the HadEX dataset was applied to the model-based indices when displaying global maps of time averages and calculating time series. All indices mentioned in Table 2.1 were analyzed on an annual basis. However, results are presented only for the key indices shown in boldface in Table 2.1. The global maps allow a comparison of the large-scale patterns of the individual indices. The time series show spatial averages of the indices for three European regions as defined in Table 2.2. When comparing the time series of HadEX and model-based indices, not only the ensemble mean is considered, but also the range of the three ensemble members of the 20C model simulations.

Temperature

In most regions, the maximum T2MAX (TXx) shown in figures 2.1 a, b is well captured by the model. However, TXx at high northern latitudes is systematically underestimated by typically 10°C and also on the Tibetan Plateau. Additional indices based on T2MAX reveal corresponding features at high northern latitudes. For example, the number of ice days (ID) is too high and the number of summer days (SU) is much too low. On the other hand, the minimum T2MAX (TXn) is in good agreement with the HadEX data (not shown). Similarly, both the spatial distribution and the absolute values of the minimum T2MIN (TNn) are very well simulated (Fig. 2.1 c, d). Other indices based on T2MIN, e.g. frost days (FD), also show good agreement between the model and HadEX data (not shown). The diurnal temperature range (DTR) (not shown), which is the difference between daily T2MAX and T2MIN, is generally underestimated, especially at high northern latitudes. However, the global spatial patterns of DTR in the model show a good agreement with the HadEX data. Although the large-scale distribution of tropical nights (TR) is reasonably well represented by the model, there are differences in the details (Fig. 2.1 e, f). For example, the area with TR > 150 days is more extended in the model (Southeast Asia, Australia, southern USA). Similarly, the cold regions with TR < 1 day are too widespread (western USA, southern Europe, Tibetan Plateau, southern part of South America) so that the transition zones cover a smaller area than in the observations.

For a more quantitative assessment of model errors, the temporal evolution of observed and simulated indices is shown in Fig. 2.2 for three European regions (cf., Table 2.2). Consistent with the spatial pattern of TXx (cf., Fig. 2.1 a, b) the model
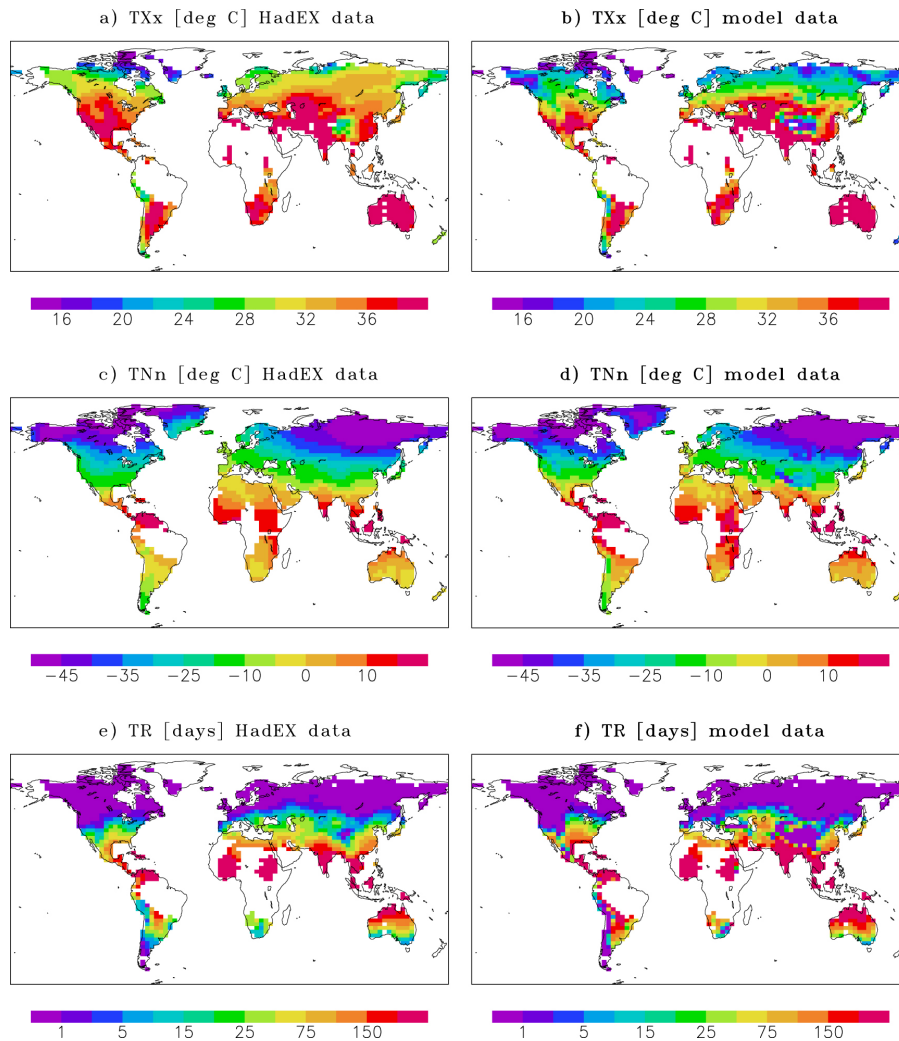
Figure 2.1— Time averaged temperature-based indices (1951-2003) for HadEX data (left) and model data (right). The model data represent the respective ensemble means of three 20C realizations. Missing values in the HadEX data are masked out in the model data as well.

simulation deteriorates with increasing northern latitude (Fig. 2.2 a-c). Whereas TXx is generally close to the observations in southern Europe, larger differences of about -2°C can be found in central Europe and, in particular, in northern Europe where the error becomes as large as -4°C. In comparison with the HadEX data, the model overestimates the number of ice days (ID) especially in northern Europe and underestimates the number of summer days (SU) in all European regions (not shown). Consistent with the spatial pattern of TNn (cf. Fig. 2.1 c, d), the HadEX data are mostly within the ensemble spread of the model data in all European regions (Fig. 2.2 d-f). In northern Europe, the model overestimates the number of frost days (not shown). The diurnal temperature range (DTR) (not shown) is underestimated
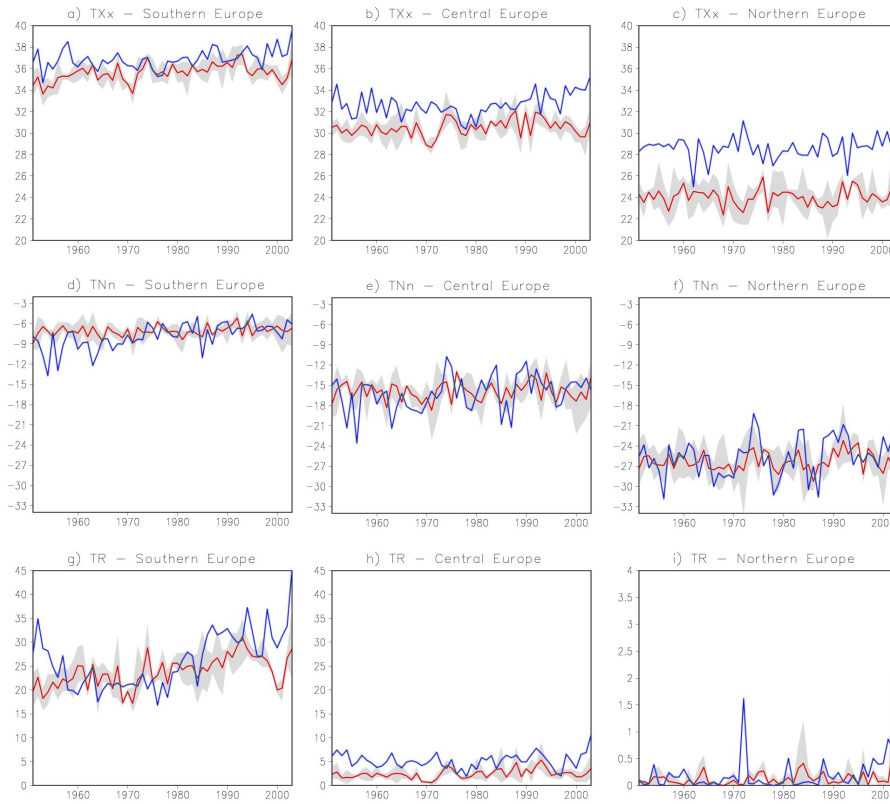
Figure 2.2— Time series (1951-2003) of spatially averaged (land only) temperature-based HadEX indices (blue) and the ensemble mean of the model-based indices (red) for three regions in Europe (cf., Table 2.2). Compared are the maximum T2MAX [$^\circ$C] in the three regions (a, b, c), the minimum T2MIN (d, e, f) [$^\circ$C] and the tropical nights (g, h, i) [days]. The shading indicates the spread of the three 20C realizations.

in all regions, but mostly in northern Europe (about 2.5°C on average). The number of tropical nights TR (Fig. 2.2 g-i) is just about 50% of the observed one in central Europe, whereas in northern Europe tropical nights are very rare events in both the observations and simulations. For southern Europe, the interpretation of the TR time series is more ambiguous. Here the simulated time-mean TR is close to the observed one, but the decline in the observed record until about 1970, and the marked increase thereafter, is missing in the model simulations. The question whether these multi-decadal changes are due to natural variability or induced by external forcing cannot be answered with confidence.

The model captures the threshold-based indices cool nights (TN10p), warm nights (TN90p), cool days (TX10p), and warm days (TX90p) (not shown) reasonably well in all European regions. However, since the actual thresholds needed to calculate these indices were not provided with the HadEX data, a meaningful comparison was not possible. Hence, these threshold-based indices are excluded from this study.
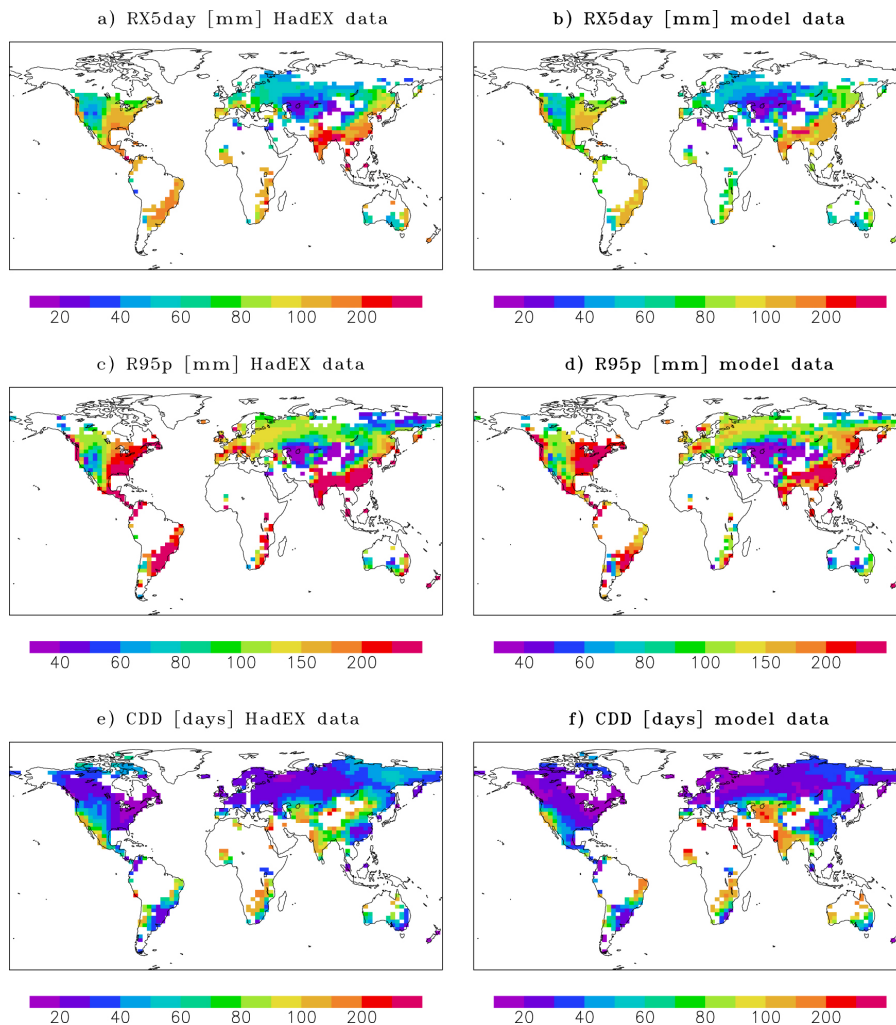
Figure 2.3— As figure 2.1, but for the precipitation-based indices, maximum 5-day precipitation (a, b), 95th percentile of precipitation on wet days (c, d), and maximum number of consecutive dry days (e, f).

Precipitation

The spatial distribution of the maximum 5-day precipitation (RX5day) is generally well represented in the model (Fig. 2.3 a, b). However, the model slightly underestimates the absolute values of RX5day in most regions, except in the western part of North America. The spatial pattern of the precipitation amount on very wet days (R95p) is very well captured (Fig. 2.3 c, d), but an overestimation of the absolute values can be seen in the western part of North America and Northeast Asia. Furthermore, the model underestimates R95p around the Mediterranean Sea, in India and Southeast Asia, and in the eastern parts of Africa and Brazil. Although the model represents the total annual wet-day precipitation (PRCPTOT) (not shown)
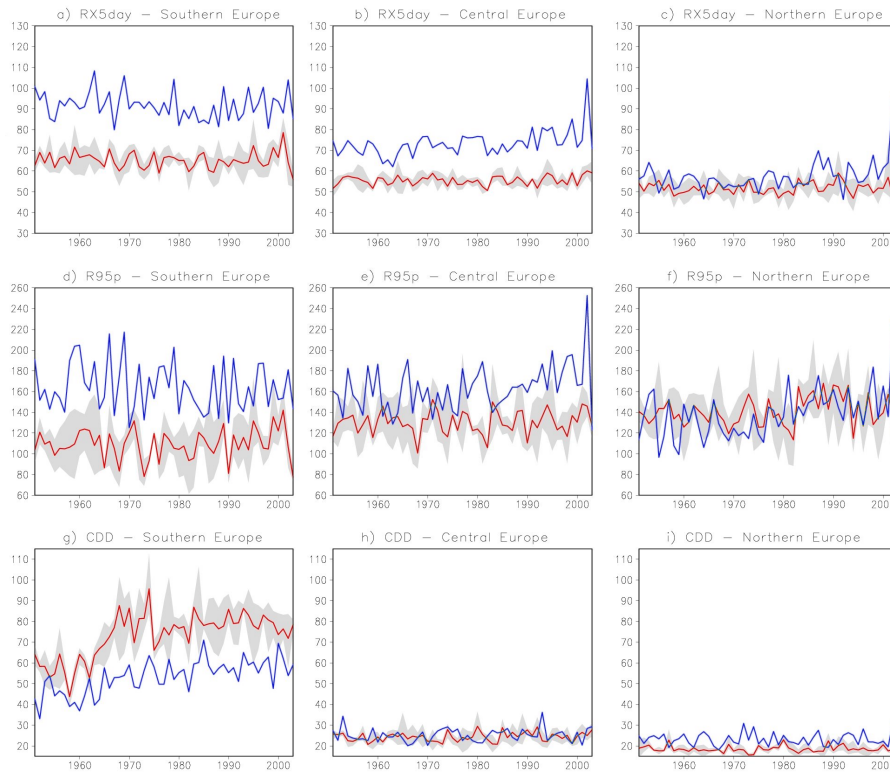
Figure 2.4— As figure 2.2, but for the precipitation-based indices maximum 5-day precipitation (a, b, c) [mm], 95th percentile of precipitation on wet days (d, e, f) [mm], and maximum number of consecutive dry days (g, h, i) [days].

well, it generally tends to underestimate extreme precipitation events as described by RX5day or R95p. This is also noticeable in other precipitation-based indices, such as maximum 1-day precipitation (RX1day) and very heavy precipitation days (R20) (not shown). In comparison with the HadEX data, the model reveals some problems in describing the precipitation distribution in terms of the number of wet days and the precipitation intensity on wet days. For instance, the model simulates too many consecutive wet days (CWD) while the actual amount of precipitation is too little on the individual wet day as indicated by the index SDII (simple daily intensity) (both not shown). The large-scale pattern of the number of consecutive dry days (CDD) is reasonably well captured (Fig. 2.3 e, f). However, at high northern latitudes, CDD is systematically lower than observed. Moreover, a significant underestimation of CDD can be seen in some dry regions, such as the northern part of Mexico, where the model and HadEX data differ by up to 60 days. In India and in the region west of the Caspian Sea, on the other hand, the model overestimates CDD by more than 50 days, on average.

The temporal evolution of RX5day for three European regions is shown in figures 2.4 a-c. In northern Europe, the HadEX time series generally falls within the en-

semble spread of the model, except in the 1990's where the observed upward trend is not simulated by the model. In regions further south, RX5day is systematically too low. For example, in central Europe this underestimation amounts to 15mm, corresponding to 20%, and in southern Europe it is about 25mm, corresponding to 28%, on average. Similar to RX5day, the R95p index is very well simulated in northern Europe (Fig. 2.4 f). Differences between the HadEX and the model data are more pronounced in central Europe (Fig. 2.4 e) and become even larger in southern Europe (Fig. 2.4 d), where the model underestimates R95p by approximately 50mm, corresponding to 30%, on average. The inter-annual variability of R95p increases towards southern Europe in both the HadEX data and model simulations. The underestimation of extreme precipitation, especially in southern Europe, can also be seen in other indices, such as the maximum 1-day precipitation (RX1day), the simple daily intensity index (SDII), the number of heavy precipitation days (R10), and the number of very heavy precipitation days (R20) (not shown). The consecutive wet days (CWD) (not shown) are well captured by the model in southern Europe but become increasingly overestimated at higher latitudes. The model represents the annual total wet-day precipitation (PRCPTOT) (not shown) best in central Europe, but overestimates this index in northern Europe and underestimates it in southern Europe. The consecutive dry days (CDD) index shown in figures 2.4 g-i is very well simulated in central Europe and reasonably well in northern Europe. The ensemble spread in northern Europe is very small and the model underestimates CDD by only a few days. In southern Europe, the model overestimates CDD by more than 20 days, corresponding to 30% on average, except in the 1950's when the simulated CDD is closer to the observed one. However, the abrupt change in the simulated CDD is not a real effect but can be attributed to a changed masking of missing values in the HadEX data (cf., section 2.4.1).

2.4.2   Changes in extremes in future climate projections

To detect changes in the indices for climate extremes in the climate projections of the 21st century, time intervals of 30 years at the end of the 20th and the 21st century, respectively, were chosen, and the time means for these periods were compared. The present-day climate state (1971-2000) was derived from the 20C ensemble, the future one (2071-2100) from the three ensemble members of the scenario runs A1B and B1, respectively. The statistical significance of the differences between these climate states was assessed through a non-parametric test as described in Roeckner et al. (2006c). The null hypothesis assumes that the difference (DIFF=Scenario-20C) is within the range of variations between randomly chosen 30-year segments of the control run (CON). This null hypothesis was tested against the alternative hypothesis that DIFF is larger than such random differences. The total of 500 years in CON was split into n = 16 chunks of 30 years length. By forming differences across all available chunks n(n-1)/2 = 120 differences were obtained. A Gaussian test was applied, where the distribution of these 120 differences for the individual indices in the control run were determined, and assessed whether the respective
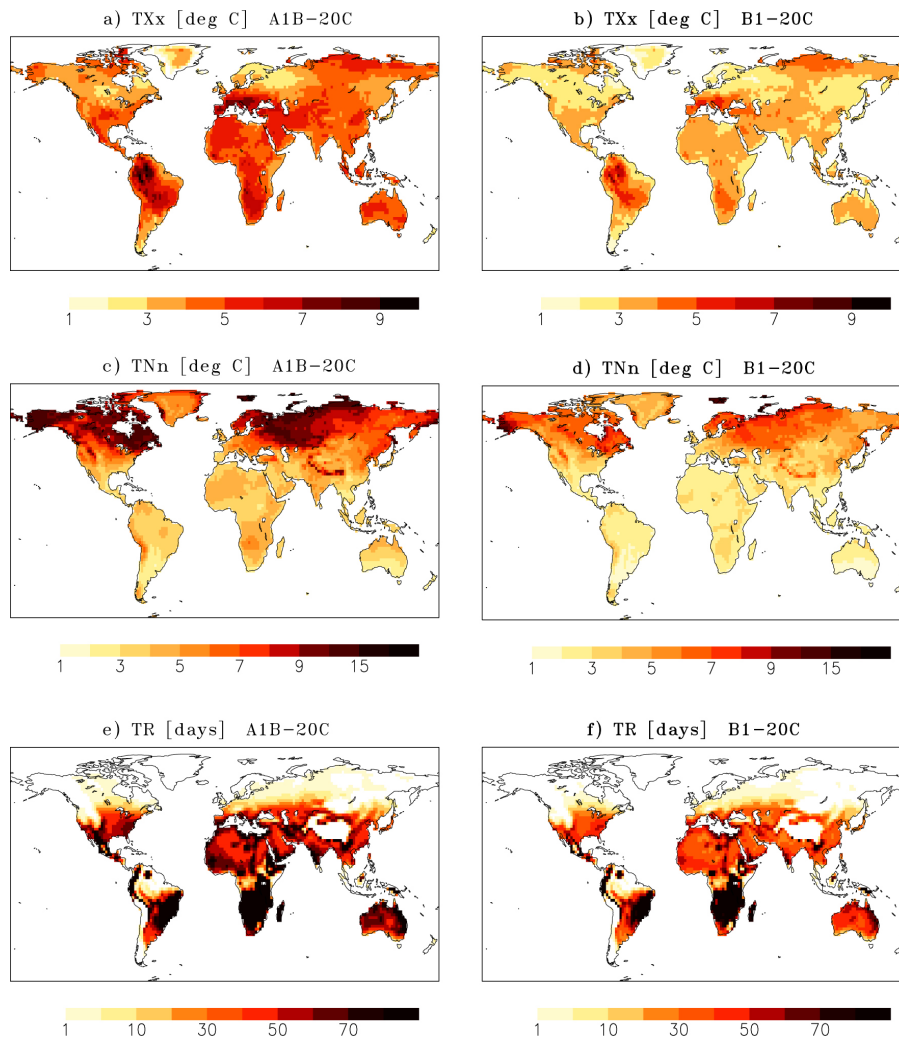
Figure 2.5—— Differences of temperature-based indices between the ensemble mean of (left) A1B (2071-2100) and 20C (1971-2000) as well as (right) B1 (2071-2100) and 20C (1971-2000) simulations. Shown are the respective differences for maximum T2MAX (a, b), minimum T2MIN (c, d) and tropical nights (e, f). All changes displayed in this figure are significant at the 95% confidence level.

DIFF was larger than the 95th percentile of the CON distribution. In that case the null hypothesis was rejected with a risk of less than 5%.

Temperature

The projected changes of temperature-based indices are shown in figure 2.5. In both scenarios, all changes in the displayed temperature indices are significant at the 95% confidence level, but the changes in A1B are generally more pronounced than in B1. The maximum T2MAX (TXx) reveals the largest increase around the

Mediterranean Sea, in southern Africa, in the northwestern part of South America but also in the far north of Siberia. Little increase can be seen in Scandinavia and in the adjacent part of Russia. The minimum T2MIN (TNn), on the other hand, reveals the largest increase at high northern latitudes, i.e., in those regions where the increase in TXx is comparatively small. In the southern hemisphere, TNn does not increase by more than 3-4°C, which is systematically smaller than the change in mean temperature (not shown). The tropical night index (TR) increases mostly around the Mediterranean Sea, in central America, central to southern Brazil, southern Africa and along the East coast of Australia. In both scenarios, tropical nights can be expected in regions like Canada and parts of Eurasia, which do not experience tropical nights under present climate conditions.
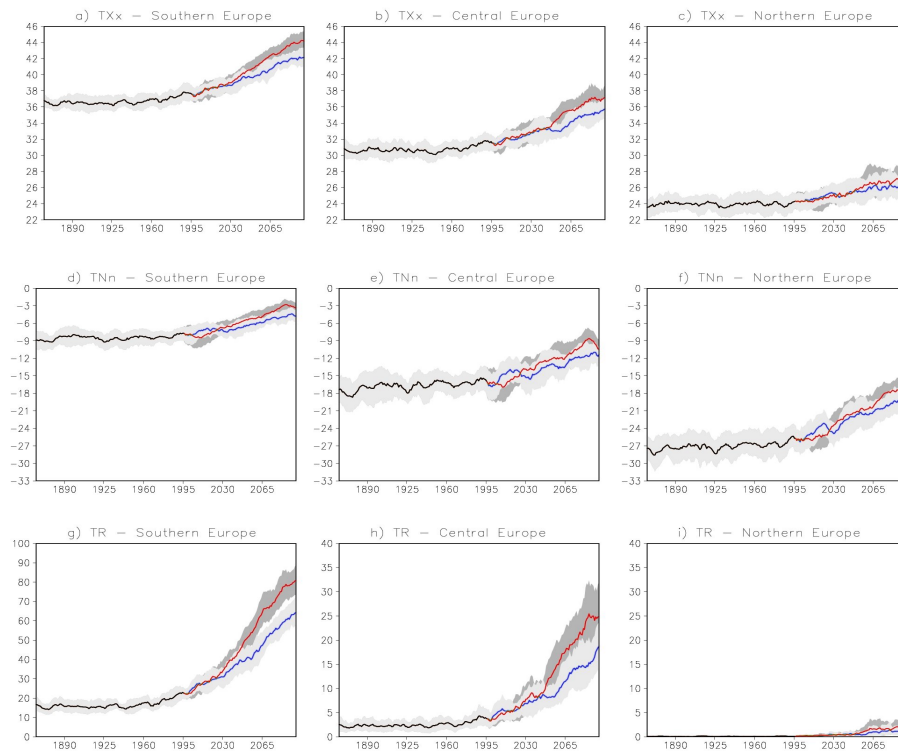
Figure 2.6— Time series (1860-2100) of spatially averaged (land only) temperature-based indices for three regions in Europe (cf., Table 2.2) in 20C (black), A1B (red) and B1 (blue) model simulations. Shown are the maximum T2MAX [°C] in the three regions (a, b, c), the minimum T2MIN (d, e, f; °C) and the tropical nights (g, h, i; days). Displayed are the respective ensemble means and the spread in the ensemble members is indicated by light (B1) and dark (A1B) shading. Data are smoothed by a 10-yr running mean.

In the time series of temperature-based indices for three European regions (Fig. 2.6), distinguishable differences between the two scenarios cannot be seen before year 2040, considering the ensemble spread indicated by shading around the ensemble mean. TXx increases mostly in southern Europe from about 37°C in the present

climate to 42°C (B1) and 44°C (A1B), respectively, in year 2100. In central Europe, the trend of TXx is similar with an increase of 5°C in B1 and 6°C in A1B until year 2100. In northern Europe, TXx rises by only 2-3°C, and the changes remain similar in both scenarios even beyond the year 2040. The regional changes of TNn are opposite to those of TXx. In contrast to TXx, the rise in TNn is most pronounced in northern Europe, from -27°C in the present climate to approximately -19°C in B1 and -18°C in A1B until the end of this century. In central and southern Europe, TNn rises by about 4°C in B1 and 6-7°C in A1B. It is interesting to note that, probably as a result of large natural variability on the regional scale, the ensemble mean changes of TNn until about year 2025 are larger in B1 than in A1B. Further it should be pointed out, that both TXx and TNn increase at a similar rate in southern and central Europe (about 4-5°C in B1 and 6-7°C in A1B). However, in northern Europe TNn increases much faster (by up to 9°C in A1B) than TXx (by only 3°C in A1B). The most striking increase of tropical nights is simulated for southern Europe, from about 15 nights per year in the present climate up to 65 nights in B1 and 80 nights in A1B until the end of this century. In central Europe, the TR increases from about 3 nights per year to 18 in B1 and 25 in A1B. A widening of the ensemble spread towards the end of the 21st century is also noticeable in that region, indicating that the inter-annual variability in the number of tropical nights is expected to increase. Even northern Europe, where no tropical nights occur in present climate, will experience a few tropical nights per year at the end of the 21st century.

Precipitation

As apparent from Fig. 2.7a-d, RX5day and R95p, which describe the wet part of precipitation extremes, show a significant increase in many regions of the world. The changes are more pronounced in A1B than in B1. The largest increase can be found at lower latitudes, in the eastern part of North America and along the West coast of Canada. Further, the R95p increases strongly in the northern part of Eurasia. A significant decrease of RX5day is found only in a few regions, for example, in southern Spain, Morocco and along the coast of southern Chile. The consecutive dry day (CDD) index increases significantly in regions around the Mediterranean Sea, especially along the African coast (Fig. 2.7 e, f). Further increases of CDD can be found in Australia, southern Africa, in the northeastern part of South America as well as along the Pacific coast of Central and South America (especially Chile). The CDD changes are systematically larger in A1B than in B1 and also the regions with significant changes are more extended in A1B than in B1 (e.g., Australia). In a few regions of the northern hemisphere, namely in parts of Alaska, Siberia and Greenland, the number of consecutive dry days tends to decrease in both scenarios.

According to the time series of precipitation-based indices for three European regions (Fig. 2.8) RX5day decreases slightly in the 21st century in southern Europe, whereas R95p shows hardly any trend. In northern Europe, however, there is a marked increase of both RX5day and R95p. In A1B, RX5day increases by about
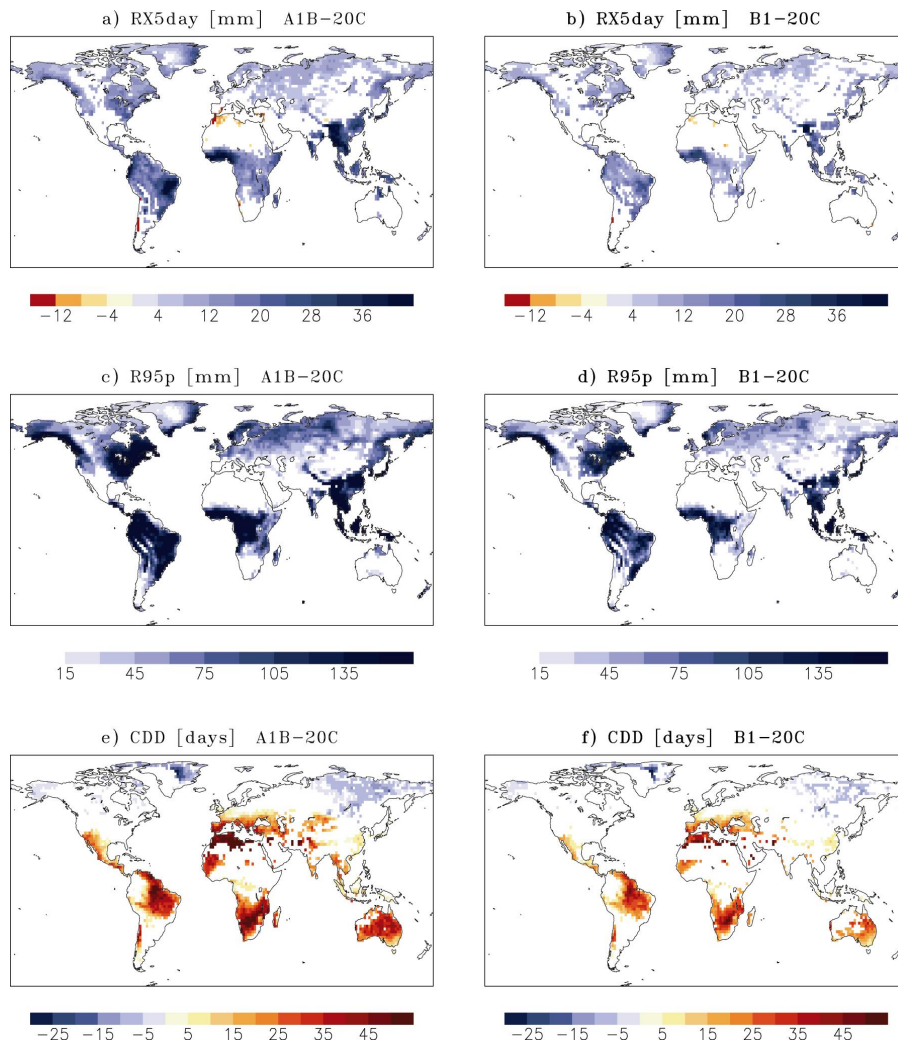
Figure 2.7— As figure 2.5, but for projected changes in the precipitation-based indices maximum 5-day precipitation (a, b), 95th percentile of precipitation on wet days (c, d), and maximum number of consecutive dry days (e, f). Changes that are statistically insignificant at the 95% confidence level are not displayed (white areas).

9mm until the end of this century, and the R95p rises by approximately 90mm. This corresponds to an increase of 17% in RX5day and 64% in R95p. In general, the RX5day differences between B1 and A1B are not pronounced in the three European regions. For R95p, differences in the ensemble means are visible in northern Europe from year 2040 onward, and in central Europe from year 2060 onward, but there is a large overlap of the respective ensemble spreads during the whole simulation period. In central Europe, RX5day and R95p increase as well, but not as strongly as in northern Europe. Distinguishable differences between the two scenarios cannot be seen until the very end of the scenario runs, where the indices undergo a sharp
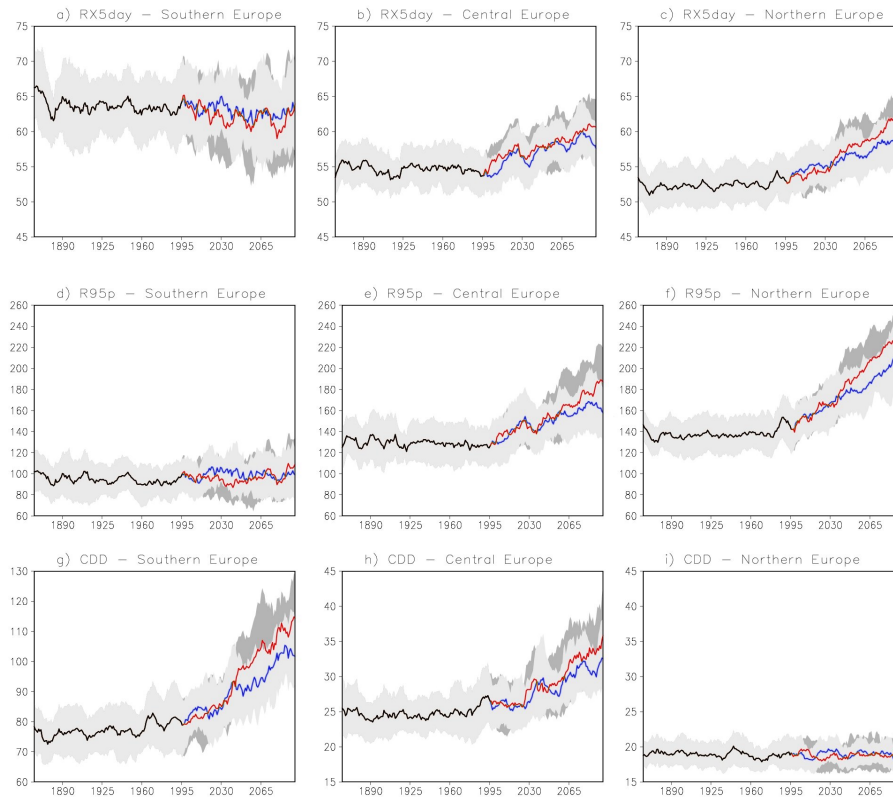
Figure 2.8—— As figure 2.6, but for the temporal evolution of the precipitation-based indices maximum 5-day precipitation (a, b, c; mm), 95th percentile of precipitation on wet days (d, e, f; mm), and maximum number of consecutive dry days (g, h, i; days).

decrease in the last 10 years of the B1 scenario. In the A1B scenario, RX5day and R95p continue to rise until the end of the 21st century whereas RX5day rises by about 7mm, corresponding to an increase of 13%, and R95p rises by about 60mm (46%). In contrast to the wet extreme precipitation events, CDD is projected to increase substantially in southern Europe, from approximately 75 days in the present climate to 105 days in B1 and 115 days in A1B. This means that the longest dry period within a year is prolonged by 1 (1.5) months at the end of this century in B1 (A1B). Differences between the scenarios do not emerge before the year 2040. In northern Europe, CDD has no trend and stays at about 19 days per year on average in both scenarios. In central Europe, CDD increases by approximately 7 days in B1 and 10 days in A1B, whereas significant differences between the scenarios cannot be distinguished since the respective ensemble ranges continue to overlap until the end of the 21st century.

2.4.3 Seasonal changes

In order to analyze seasonal changes in TXx, TNn and RX5day, 30-year monthly means of these indices were calculated at each grid point for the 20C simulations (1971-2000) and for the A1B and B1 scenarios (2071-2100), respectively, and the results for the three European regions were then obtained by spatial averaging (land only). Since three ensemble members are available for both the 20C experiments and the scenarios, it is possible to compute 32 differences between the respective scenario and the 20C experiment. Results are displayed for both the ensemble mean differences for every month and for the respective standard deviations obtained from all 9 individual differences.
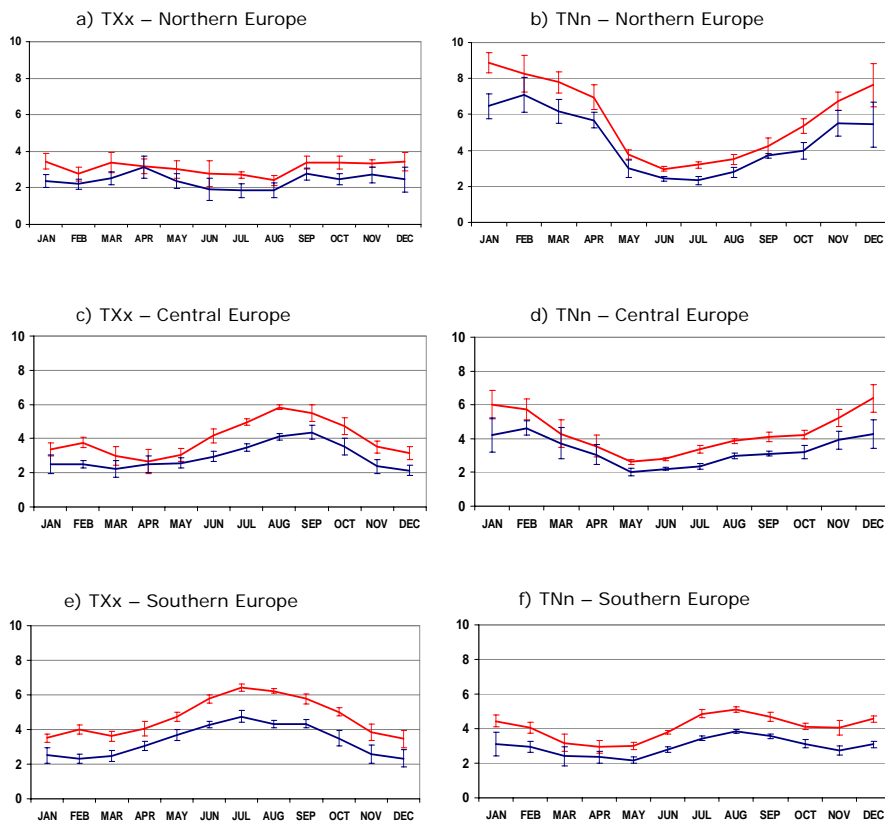
Figure 2.9— Simulated changes in the climatological annual cycle of maximum T2MAX (a, c, e; °C) and minimum T2MIN (b, d, f; °C) for three regions in Europe (cf., Table 2.2). Red: Differences between A1B (2071-2100) and 20C (1971-2000). Blue: Differences between B1 (2071-2100) and 20C (1971-2000). The standard deviation (1σ), calculated from 9 differences between the respective ensemble members, is indicated by vertical bars.

Temperature

Figure 2.9 shows the simulated changes in the climatological annual cycle of temperature-based indices for the three European regions. TXx and TNn increase in all months and in all European regions in both scenarios, but the changes are generally seasonally dependent. An exception is TXx in northern Europe, which increases more or less constantly throughout the year. In contrast, TNn in northern Europe shows the largest increase (up to 9°C in A1B) in the winter months, and the smallest increase (down to 3°C in A1B) in the summer months. The standard deviations are also largest in winter and smallest in summer. Significant differences between A1B and B1 are evident, as indicated by the separation of the blue and red bars in almost all months. In central Europe, the changes in the annual cycles of TXx and TNn are largely out of phase. TXx increases predominantly from July to October (above 5°C in A1B), whereas TNn reveals the largest increase in the winter months (around 6°C in A1B). The increase in TNn is relatively small in May and June (less than 3°C), where also the smallest standard deviations occur. The smallest increase of TXx can be found in spring (3°C in A1B) and from late autumn to spring (2.5°C in B1). Standard deviations of TXx overlap in January and in spring. The smallest standard deviations, in both scenarios, occur in July and August. In southern Europe, the changes in the annual cycles of TXx and TNn differ as well. The largest increase in TXx is found from June to September, which is around 6°C in A1B and around 4.5°C in B1. The standard deviations do not overlap throughout the year, i.e., the scenarios are well separated. In the winter months, the increase in TXx is substantially smaller than in summer (2.5°C in B1 and 3.5 - 4°C in A1B). The increase in TNn is smallest in spring (around 2.5°C in B1 and 3°C in A1B). The largest increase in TNn is found between July and September (almost 4°C in B1 and 5°C in A1B), but TNn remains relatively high in winter as well (about 4.5°C in A1B). The standard deviations of TNn do not overlap except for March and April. The standard deviations of TXx and TNn are, in general, smallest in southern Europe and largest in northern Europe due to the north-south gradient in inter-annual variability, especially in the winter months.

Precipitation

According to figure 2.10a, which shows the simulated changes in the climatological annual cycle of the precipitation-based index RX5day in northern Europe, the largest increase of about 6mm in A1B (corresponding to about 20% on average) can be found in late autumn to winter (October-February). In B1 the largest increase of 4-5mm, corresponding to 15% on average, occurs from October to December. The standard deviations in both scenarios do not overlap in January, February and November. In both scenarios, the smallest increase of about 2mm, corresponding to 6%, is found in August. In central Europe (Fig. 2.10b), RX5day increases between October and April by about 4mm (14%) in A1B and 2mm (7%) in B1, and it decreases in the summer months by up to 5mm (20%) in August (A1B). These changes are
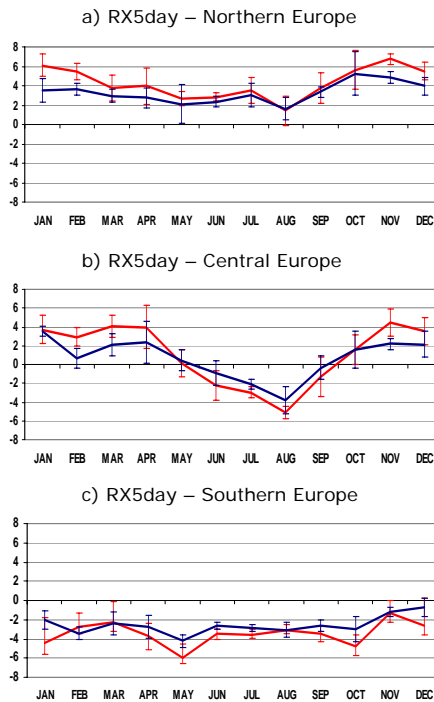
Figure 2.10— As figure 2.9, but for the precipitation-based index max. 5-day precipitation (mm).

more pronounced in A1B, but generally, except for February and November, the standard deviations in the scenarios do overlap. In May and September the changes of RX5day are insignificant. In southern Europe (Fig. 2.10c), RX5day decreases in both scenarios. In A1B, this decrease is more pronounced than in B1, but the standard deviations do overlap in all months. The largest decreases in A1B can be found in May (6mm or 32%) and October (4.8mm or 17%). In B1, the smallest decrease of RX5day is found in December (1mm or 3%) whereas the largest decrease, as in A1B, is found in May (4mm or 21%).

2.5   Discussion and concluding remarks

The comparison with the HadEX indices shows that the ECHAM5/MPI-OM model, in general, is able to capture the climatological large-scale patterns of extreme temperature and precipitation indices with good fidelity, although the quality of the simulations depends on the index and region under consideration. For example, the maximum summer temperatures, TXx, are severely underestimated by up to 10°C at high northern latitudes, whereas the minimum T2MIN (TNn) pattern is realistically simulated. The negative bias of TXx at high northern latitudes may be caused by an overly strong westerly flow in boreal summer (Roeckner et al. (2006b)) with enhanced advection of relatively wet and cold maritime air masses and, consequently,

high cloud amount and precipitation (Hagemann et al. (2006)). The simulated minimum winter temperatures TNn, on the other hand, are similar to those of HadEX due to the fact that the large-scale circulation in boreal winter is well simulated (Roeckner et al. (2006b)). In Europe, the biases mentioned above are obvious as well. Whereas TNn is very well simulated in southern, central, and northern Europe, TXx is slightly underestimated in central Europe but severely underestimated in northern Europe. As to be expected, there is a marked meridional gradient in TR with values close to zero in northern Europe and about 25 days in southern Europe in both the simulations and observations. At lower latitudes the temperature-based indices are in good agreement with the HadEX indices. This applies to both TXx and TNn, whereas the number of tropical nights, TR, is slightly on the high side.

The large-scale patterns of precipitation-based indices, i.e., the 5-day maximum (RX5day) and 95th percentile of precipitation (R95p) as well as the maximum number of consecutive dry days (CDD), are similar to the observed ones. However, in most regions both RX5day and R95p are smaller than observed. To some extent, this might be due to methodological differences in the computation of observation-based and model-based indices, respectively (see section 2.3). The model input available for calculating the indices represents averages for grid-box areas of up to some 40000 km^2, whilst the observed indices were computed from data at measurement sites and gridded thereafter. Very likely, the former method implies a stronger smoothing of extremes than the latter, in particular for spatially inhomogeneous variables like precipitation. In addition, regional biases in the simulated mean climate state do contribute to biases in precipitation extremes as well. For example, in the Mediterranean region, the dry bias in the mean state is reflected in the underrepresentation of RX5day and R95p and overestimation of CDD. In most regions, the number of consecutive wet days is higher than observed, whereas the mean rain intensity is too low.

In conclusion, the simulated broad-scale patterns of temperature- and precipitation-based indices are in good agreement with those obtained from the HadEX data, but the model biases can be substantial in certain regions (e.g., TXx at northern high latitudes, precipitation-based indices in the Mediterranean region).

In the climate projections for the 21st century, all temperature-based indices show a significant increase worldwide at the end of this century. Similarly, extreme precipitation (RX5day and R95p) is projected to increase significantly in most regions of the world, especially in those regions that are relatively wet already under present climate conditions (middle and high northern latitudes, Southeast Asia, Indonesia, Central Africa, South America). Analogously, CDD increases particularly in those regions that are already relatively dry under present climate conditions (Mediterranean countries, California and northern Mexico, Mauritania, South Africa, Australia). An exception is the northeastern part of South America where all precipitation indices, RX5day, R95p, and CDD, increase significantly. In general, the differences between humid and arid climate zones tend to increase under global warming. This has been found already for the changes in the mean state (e.g., IPCC (2001)) but it seems to apply to the changes in the precipitation extremes as well.

Northern high latitudes are affected by a strong increase of T2MIN, which causes an extension of the growing season length and a substantial reduction in the number of frost days in both climate scenarios. This has a major impact on the terrestrial biota (Parmesan et al. (2000)) and on the permafrost soils. The northern part of Siberia will be mostly affected since both extremes of the temperature distribution, TXx and TNn, increase substantially in that region. The fact that TNn increases faster than TXx, especially in northern Europe, can be related to a northward shift of the westerly wind regime during winter months causing enhanced advection of warm and moist maritime air, higher cloud amount and reduced nighttime cooling in the winter months. This finding is consistent with the results obtained by Easterling et al. (1997) and Giorgi et al. (2001). The substantial rise of TNn in winter in central and northern Europe leads to less snowfall and a shorter retention period of snow, especially in the low mountain ranges in central Europe. This will have a major impact on tourism in those regions. On the other hand, in southern and central Europe, TXx rises predominantly in summer and early autumn, which is consistent with the prolongation of dry spells in these regions.

Agriculture will be diversely affected in northern and southern Europe, respectively. In northern Europe, higher temperatures and a longer growing season length are favorable conditions for agriculture, whereas in southern Europe extensive irrigation will be required because of higher temperatures, less precipitation, and prolonged dry spells in the future climate.

There is also a significant increase worldwide in the number of tropical nights. At the end of this century, a tropical night will not be the exception in southern Europe, as in the present climate, but the rule in all summer months. This intensifies the heat stress on humans and other living organisms provoked by increasing heat waves or daytime temperatures (Meehl & Tebaldi (2004)). This heat stress is further enhanced by the increasing number of consecutive dry days. These changes in climate extremes will have a severe impact on living conditions, water supply, and agriculture in the regions around the Mediterranean Sea. Northern regions, where no tropical nights occur in the present climate, will face an increasing number of tropical nights as well, which will occur in summer during sporadic heat wave periods. This will demand socio-economic adaptation measures of northern populations that are not used to tropical nights, e.g. enhanced cooling systems and special health care for elderly people and children.

The regional analysis of the annual cycle indicates that the increase of maximum 5-day precipitation in central and northern Europe occurs predominantly in the winter months, caused primarily by a northward shift of the storm tracks (Bengtsson et al. (2006)). In central Europe, RX5day decreases during summer, especially in August, induced by an eastward extension of the Azores high, which leads to a reduction of moisture supply from the Atlantic and thus causes an intense drying in the Mediterranean region (Giorgi et al. (2001)). The prolongation of dry spells will also affect central Europe. In general, the regions with extended dry spells broaden and, therefore, regions endangered by desertification grow. In particular, the Mediterranean regions will face longer drought conditions lasting for more than

3 months, especially in summer. In some studies, heavy rainstorm events (smaller in scale than RX5day) will become more probable (Christensen & Christensen (2003)). This amplifies the risk of erosion of dried-out, uncovered soils in these regions. The northern part of Europe will not be endangered by longer dry periods, but the increase of RX5day enforces the risk of flooding.

A crucial point to ask is to what extent the simulated changes might be affected by the model biases identified in the comparison with the HadEX indices. For example, is the modest increase in TXx at high northern latitudes affected by the negative bias in these regions or is it just the result of enhanced advection of moist maritime air in the warmer climate? Similarly, is the enhanced warming and drying in the Mediterranean countries partially caused by the dry model bias in these regions? Is the projected increase in RX5day and R95p too small because these indices are generally underestimated compared to the HadEX data? To answer these questions, a multi-model study would be required allowing to investigate the impact of model biases on the robustness of the response. Nevertheless, it seems fair to conclude that more confidence should be placed in the projections of those indices that are realistically captured by the model under present-day climate conditions.

In many respects, the results found in our simulations are consistent with the multi-model study of Tebaldi et al. (2006) and other studies on changes in extremes of temperature and precipitation (e.g., Meehl et al. (2000); Meehl & Tebaldi (2004)). This study further showed that, in addition to the large-scale patterns, it is useful to focus on regional scales such as the three European regions, which show distinct differences in the temporal evolution of the extreme indices on both annual and seasonal time scales. Many of these changes are likely to be related to changes in the large-scale atmospheric circulation (e.g., Haylock & Goddess (2004); Cassou et al. (2005)). The robustness of the correlations between the large-scale flow and extreme indices will be investigated in a separate study.

Table 2.1— Excerpt of the extreme indices recommended by the ETCCDMI (http://cccma.seos.uvic.ca/ETCCDMI/list_27_indices.shtml). Indices that are described in detail in this study are highlighted in bold letters. * Spell indices

ID		Indicator name	Indicator definitions	Units
1	TN10p	Cool nights	Let TN_{ij} be the daily minimum temperature on day i in period j and let $TN_{in}10$ be the calendar day 10th percentile centered on a 5-day window. The percentage of days in a year is determined where $TN_{ij} < TN_{in}10$	%
2	TX10p	Cool days	Let TX_{ij} be the daily maximum temperature on day i in period j and let $TX_{in}10$ be the calendar day 10th percentile centered on a 5-day window. The percentage of days is determined where $TX_{ij} < TX_{in}10$	%
3	TN90p	Warm nights	Let TN_{ij} be the daily minimum temperature on day i in period j and let $TN_{in}90$ be the calendar day 90th percentile centered on a 5-day window. The percentage of days is determined where $TN_{ij} > TN_{in}90$	%
4	TX90p	Warm days	Let TX_{ij} be the daily maximum temperature on day i in period j and let $TX_{in}90$ be the calendar day 90th percentile centered on a 5-day window. The percentage of days is determined where $TX_{ij} > TX_{in}90$	%
5	**TXx**	**Max T2MAX**	**Let TXx be the daily maximum temperatures in month k, period j. The maximum daily maximum temperature each month is then: $TXx_{kj} = \max(TXx_{kj})$**	**°C**
6	TXn	Min T2MAX	Let TXn be the daily maximum temperature in month k, period j. The minimum daily maximum temperature each month is then: $TXn_{kj} = \min(TXn_{kj})$	°C
7	TNx	Max T2MIN	Let TNx be the daily minimum temperatures in month k, period j. The maximum daily minimum temperature each month is then: $TNx_{kj} = \max(TNx_{kj})$	°C
8	**TNn**	**Min T2MIN**	**Let TNn be the daily minimum temperature in month k, period j. The minimum daily minimum temperature each month is then: $TNn_{kj} = \min(TNn_{kj})$**	**°C**
9	FD	Frost days	Let TN be the daily minimum temperature on day i in period j. Count the number of days where $TN_{ij} < 0°\,C$	days
10	ID	Ice days	Let TX be the daily maximum temperature on day i in period j. Count the number of days where $TX_{ij} < 0\ °C$	days
11	SU	Summer days	Let TX be the daily maximum temperature on day i in period j. Count the number of days where $TX_{ij} > 25\ °C$	days
12	**TR**	**Tropical nights**	**Let TN be the daily minimum temperature on day i in period j. Count the number of days where $TN_{ij} > 20\ °C$**	**days**

Table 2.1— continued

ID		Indicator name	Indicator definitions	Units
13	GSL	Growing season length	Let T be the mean temperature on day i in period j. Count the number of days between the first occurrence of at least 6 consecutive days with T $>$ 5 °C and the first occurrence after 1st July (NH) or 1st January (SH) of at least 6 consecutive days with $T_{ij} <$ 5 °C	days
14	DTR	Diurnal temperature range	Let TN and TX be the daily minimum and maximum temperature respectively on day I in period j. If I represents the number of days in j, then: $DTR_j = \sum_{n=1}^{I} (TX_{ij} - TN_{ij})/ I$	°C
15	RX1day	Max 1-day precipitation amount	Let RR_{ij} be the daily precipitation amount on day i in period j. The maximum 1-day value for period j are: $RX1day_j = \max (RR_{ij})$	mm
16	**RX5day**	**Max 5-day precipitation amount**	**Let RR_{kj} be the precipitation amount for the 5-day interval ending k, period j. Then maximum 5-day values for period j are: $RX5day_j = \max (RR_{kj})$**	**mm**
17	SDII	Simple daily intensity index	Let RR_{wj} be the daily precipitation amount on wet days, RR $>=$ 1mm in period j. If W represents number of wet days in j, then: $SDII_j = (\sum_{w=1}^{W} RR_{wj}) / W$	mm/d
18	R10	Number of heavy precipitation days	Let RR_{ij} be the daily precipitation amount on day i in period j. Count the number of days where $RR_{ij} >$ 10mm	days
19	R20	Number of very heavy precipitation days	Let RR_{ij} be the daily precipitation amount on day i in period j. Count the number of days where $RR_{ij} >$ 20mm	days
20	**CDD***	**Consecutive dry days**	**Let RR_{ij} be the daily precipitation amount on day i in period j. Count the largest number of consecutive days where $RR_{ij} <$ 1mm**	**days**
21	CWD*	Consecutive wet days	Let RR_{ij} be the daily precipitation amount on day i in period j. Count the largest number of consecutive days where $RR_{ij} >$ 1mm	days
22	**R95p**	**Very wet days**	**Let RR_{wj} be the daily precipitation amount on a wet day w (RR $>=$ 1mm) in period i and let $RR_{wn}95$ be the 95th percentile of precipitation on wet days in the 1961-1990 period. If W represents the number of wet days in the period, then: $R95p_j = \sum_{w=1}^{W} RR_{wj}$, where $RR_{wj} > RR_{wn}95$**	**mm**
23	PRCP TOT	Annual total wet-day precipitation	Let RR_{ij} be the daily precipitation amount on day i in period j. If I represents the number of days in j, then: $PRCPTOT_j = \sum_{n=1}^{I} RR_{ij}$	mm

Table 2.2— Spatial definition of three European regions

Region	Longitudes	Latitudes
Southern Europe	12°W - 40°E	35°N - 45°N
Central Europe	12°W - 40°E	45°N - 55°N
Northern Europe	12°W - 40°E	55°N - 70°N

Chapter 3

Euro-Atlantic atmospheric blocking conditions and extreme events in present and future climate simulations[1]

Abstract

The impact of Euro-Atlantic blocks on the present and future (SRES A1B) European climate is studied. Composite maps show that blocking events are associated with anomalously dry and cold winters in Europe. Especially the extreme winter nighttime temperature is significantly anti-correlated with blocking events closed to Europe. In A1B the blocking frequency is slightly diminished but the influence on the European winter climate remains robust. Due to a northeastward shift of the blocking pattern from the northeastern North Atlantic towards the Norwegian Sea, a larger part of Europe will experience anomalously cold episodes during the winter months than under present climate conditions. In general, winter blocks tend to moderate the changes in both temperature and precipitation resulting from the anthropogenic increase in greenhouse gases. In summer, the correlations between blocking frequency and extreme events are statistically insignificant.

---

[1]submitted to *Geophysical Research Letters*, with M. Croci-Maspoli as co-author.

3.1   Introduction

Extreme temperature and precipitation events moved in the center of attention, since the susceptibility of human society to the destructiveness of extreme events is increasing due to advancing technology and living standards as well as rising population density (Meehl et al. (2000)). For a better understanding and improved prediction of extreme events it is of major importance to investigate their link to large-scale atmospheric circulation patterns. The latter are assumed to have an important effect on the occurrence of extreme events (Klein Tank & Koennen (2003)). In this respect atmospheric blocking acts as a prominent feature with considerable impacts on the Euro-Atlantic climate. It plays a key role in the European flow variability due to its capability to disturb predominant cyclonic westerly flow. Atmospheric blocking is in general defined as anti-cyclonic quasi-stationary high-pressure system persisting for several days up to weeks. Owing to its large spatial extent and temporal persistence, it can be responsible for dry and cold winter (Trigo et al. (2004)) and hot summer at its core and wet conditions around the block (Rex (1951)).

In the past, several studies have pointed to the lacking accuracy of coupled general circulation models (CGCMs) to represent atmospheric blocking, particularly in the Euro-Atlantic region (e.g., Tibaldi & Molteni (1990); D'Andrea et al. (1998); Pelly & Hoskins (2003a)). Therefore, we first investigate how well Euro-Atlantic blocks, represented by a Potential Vorticity (PV)-based blocking indicator, are simulated in the coupled atmosphere-ocean model ECHAM5/MPI-OM. We then analyze variables such as the 500hPa geopotential height, surface temperature and precipitation during blocking conditions close to the European continent to illustrate the anomalous climate associated with blocking events. Finally, we follow the argument that atmospheric blocking is associated with extreme precipitation and temperature and we investigate changes of Euro-Atlantic blocking frequency under future climate conditions and their associations to projected changes in extreme events.

3.2   Data and methodologies

3.2.1   Model experiments

In this study, the climate model ECHAM5/MPI-OM (Jungclaus et al. (2006)) is employed, hereinafter referred to as ECHAM5. The atmospheric component has a horizontal resolution of 63 wave numbers in spectral space ($1.875° \times 1.875°$ in grid-point space) and 31 vertical levels up to 10 hPa. The oceanic component has a nominal horizontal resolution of $1.5°$ and 40 vertical levels. The model does not employ flux adjustments. Greenhouse gases (GHG) and sulfate aerosols in the 20th century simulations (20C) are prescribed according to observations and chemical transport model results, respectively. For the analysis of the present-day climate, we use 6-hourly data generated from the 20C simulations consisting of an ensemble of three members. We compare the 20C results with ERA-40 re-analysis data (Up-

pala et al. (2005)), hereinafter referred to as ERA-40, for the time period 1961 to 2000. The analysis of the future climate is based on 6-hourly data generated from a three-member ensemble simulation of the IPCC SRES scenario A1B. We use the last 40 years (2160-2199) of the stabilization period, where the GHG and aerosol concentrations are kept constant at the level of year 2100. We concentrate our analyses on the winter (December to February, DJF) and summer season (June to August, JJA).

3.2.2 Blocking indicator

In recent years several attempts have been undertaken to objectively define atmospheric blocking events. They all tie in with the common characteristics of blocking such as enhanced sea level pressure, elevated geopotential height or anticyclonic wind field. The 500 hPa geopotential height (Z500)) is the most frequently applied base field for blocking indicators (e.g., Tibaldi & Molteni (1990) (hereinafter TM90), Dole & Gordon (1983); Sausen et al. (1995)). More recently, indices based upon the potential vorticity field have been developed (e.g., Pelly & Hoskins (2003a); Schwierz et al. (2004)). The climatological distribution (temporal, spatial and frequency) of blocks depends on the indicators applied and can differ in several aspects (some are described in Scherrer et al. (2006)). Nevertheless the overall distribution of these climatologies shows similarities and depending on the study's preferences a specific indicator is more or less adequate.

The blocking detection method used in this study is based upon the signature of the block in the three-dimensional potential vorticity (PV) field. The blocking detection algorithm is separated into two steps. First, regions of negative PV anomalies between 500 hPa and 150 hPa are identified. These anomalies are calculated with respect to the 1961-2000 and 2160-2199 periods, respectively. Second, these negative PV anomalies are temporally tracked and structures with a lifetime longer/equal than a specified time (here 10 days) are defined as blocking events. As a result we obtain a two-dimensional blocking representation for every instance of time (6-hourly resolution). For further details upon the blocking index and its climatological application to the ERA-40 data set, see Schwierz et al. (2004) or Croci-Maspoli et al. (2007b), respectively.

The here applied blocking index allows a wide spectrum of applications. It is highly accurate for dynamical blocking lifetime studies since the method is able to track a block from its genesis to its lysis. The method is particularly useful for model validation studies, and gives a better understanding of the dynamics of blocking in climate change experiments. Due to the fact that we concentrate on the analysis of extreme events in Europe, we focus on blocks occurring close to Europe in their life cycle (15°W-30°E, 50°N-70°N) as depicted by the black box in figure 3.1 (hereinafter referred to as European Blocks (EB)).

3.2.3   Indices for extreme events

Extreme events can be defined by selected indices, such as maximum 5-day precipitation (RX5day), minimum of the minimum 2-m temperature (TNn) and maximum of the maximum 2-m temperature (TXx) described in Frich et al. (2002). These indices characterize moderate but robust large-scale extreme events that are well captured by ECHAM5 (Sillmann & Roeckner (2008)). RX5day is a useful indicator for large-scale flooding events that are caused by long lasting and spatially extended heavy precipitation events. TXx and TNn represent the tails of the temperature distribution, corresponding to extreme day- and nighttime temperatures, respectively.

3.2.4   Composite maps

To depict the typical flow pattern as well as the typical temperature and precipitation fields associated with EB, we calculate composite maps for monthly means of 500 hPa geopotential height (Z500), 2m-temperature (TEMP2) as well as precipitation (PREC) for months with high blocking frequencies within the EB region. High blocking frequencies are defined as frequencies greater than one standard deviation above the respective monthly climatological means.

3.2.5   Correlation analysis

We determine the associations between the blocking indicator and the indices for extreme events by calculating the Spearman's rank correlation coefficient. This is a robust correlation index in terms of outliers and does not rely on a normal distribution. We test for correlations at the 5% significance level with a two-sided Spearman's rank correlation test according to Best & Roberts (1975). Due to the chosen significance level, at least 5% of the grid points with significant correlations could be falsely detected. For this reason we performed a field significance test (with a global test level of 5%) proposed by Wilks (2006), estimating the false discovery rate (FDR) of erroneously rejected null hypothesis (no correlation). This test is very conservative concerning potential spatial correlations.

For the correlation analysis, the field average of blocking frequency over the EB region is calculated. We concatenated the respective 40-year time slices (1961-2000) and (2160-2199) of the three ensemble members, thus receiving time series of 120 years for the analysis of blocking frequencies and extreme indices in the 20C and A1B climate, respectively. Correlations between the EB blocking indicator and the extreme indices are then calculated at each grid point in the Euro-Atlantic domain for a particular season.
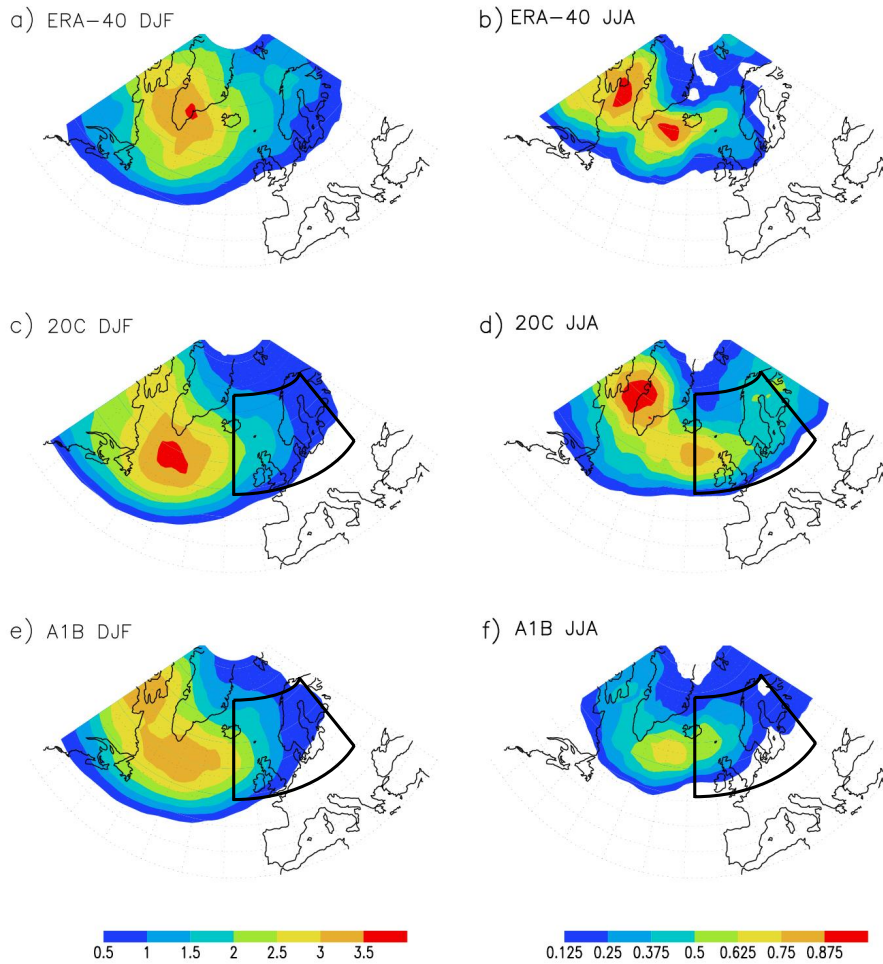
Figure 3.1— Climatologies of blocking frequency [%] for winter (DJF, left panels) and summer (JJA, right panels; note different scale). Shown are results for the present climate (1961-2000) in (a, b) ERA-40 and (c, d) ECHAM5 (ensemble means), and (e, f) for the A1B scenario (ensemble means 2160-2199). The black box frames blocking events in the EB region (15°W-30°E, 50°N-70°N), considered in the analyses.

3.3   Results

3.3.1   Blocking climatology

In figure 3.1, climatologies of blocking frequencies are compared for ERA-40, 20C, and A1B. Blocking frequencies are defined here as the percentage of time a particular grid point is blocked by a block with a lifetime ≥ 10 days. Hence, a blocking frequency of 1%, for example, corresponds to about one blocked day per season.

In general, there is good agreement between ECHAM5 and ERA-40 concerning the seasonal distribution and location of blocking. In the winter months, the location

of highest blocking frequency in ERA-40 is found over southeastern Greenland. In ECHAM5 the center is shifted southward and is more extended than in ERA-40. Studies based on the Z500 anomaly maxima (e.g., Dole & Gordon (1983); Bates & Meehl (1986); Sausen et al. (1995)) also found the winter maxima of blocking frequency to the southeast of Greenland, whereas studies based on the meridional Z500 gradient (e.g., TM90) find a maximum between the northern British Isles and Scandinavia (see Scherrer et al. (2006) for a discussion of these differences). In A1B, the DJF maximum blocking frequency decreases by about 15% relative to 20C and by about 8% on average in the EB region. There is little change in the pattern, but a slight increase west of Greenland and also in the western part of the EB region can be identified.

In summer (JJA) blockings are far less frequent than in winter. The area of high frequency in the Davies Strait is well captured, but the model misses the second maximum between Greenland and Iceland and overestimates the blocking frequency in the EB region. Summer blocking events experience a major decrease in A1B. The Davis Strait maximum disappears completely and a weak maximum appears southwest of Iceland. In the following we exclude the summer because the correlations between the EB index and extreme events are statistically insignificant as inferred from a field significance test.

3.3.2   Composite maps

To get additional information about the impact of blocking over the Euro-Atlantic region, we illustrate the mean height pattern as well as the mean surface temperature and precipitation patterns associated with EB in winter in figure 3.2. Positive Z500 anomalies (Fig. 3.2a) centered in the northeastern North Atlantic suggest northerly flow anomalies further east leading to anomalously cold and dry winter months over large parts of Europe. In A1B, the positive anomaly moves northeastward towards the Norwegian Sea, whereas the negative anomalies around the block combine into a single belt stretching from Newfoundland to the Black Sea and beyond.

The composite map of surface temperature (TEMP2) shows cold anomalies from northeastern to central Europe and positive anomalies over Greenland resulting from the southerly inflow of warm and humid air masses. In A1B, this pattern remains almost unchanged but the negative anomalies over Europe are more pronounced than in 20C.

The composite map of precipitation (PREC) depicts anomalously dry conditions over the eastern Atlantic and western Europe, in areas where the mean winter precipitation is also larger than in central and eastern Europe (not shown). Positive anomalies can be found around the block. The PREC pattern is very similar to that found by Trigo et al. (2004) in the NCEP/NCAR re-analysis, but using the TM90 index. In A1B the negative anomaly moves northeastward and the positive anomalies around the block are intensified and shifted eastward in the southern part, unisonous with the eastward extension of the cyclonic flow anomaly around 40°N.
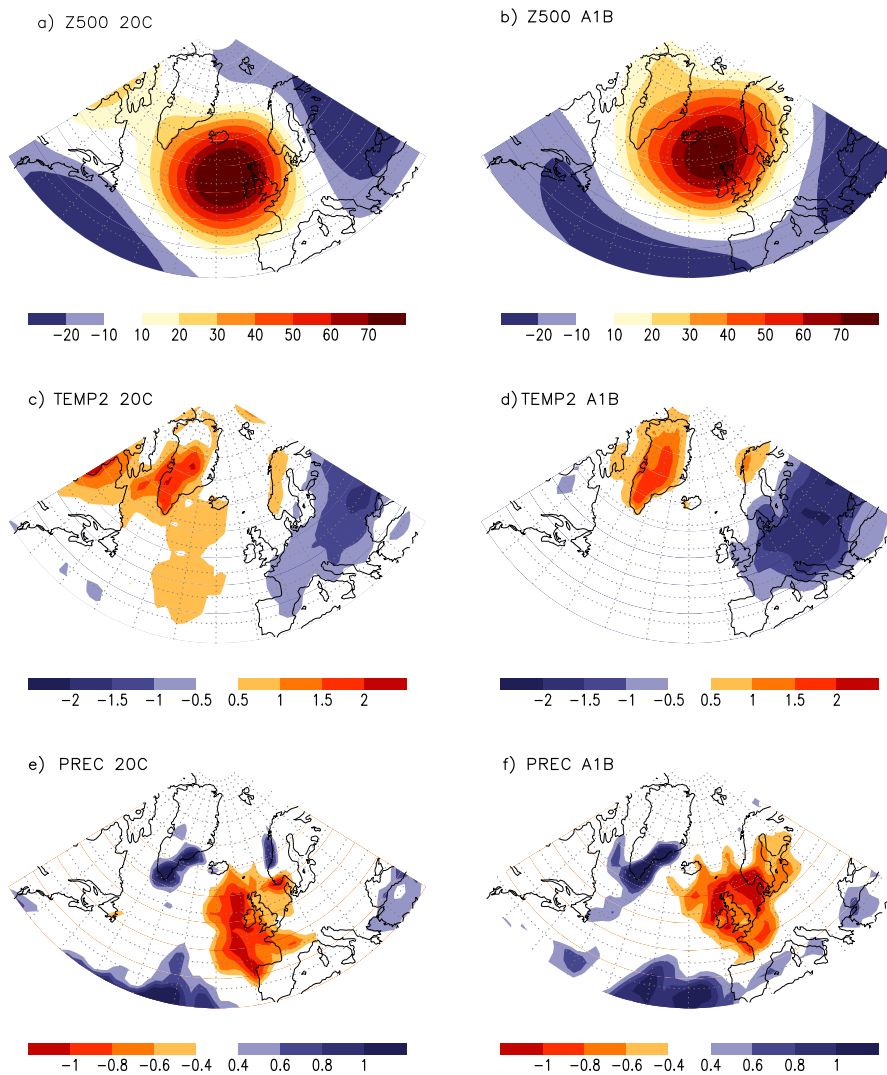
Figure 3.2— Composite maps of monthly anomalies of (a, b) 500hPa geopotential height [m], (c, d) 2m-temperature [K], and (e, f), precipitation [mm/d] for months with high blocking frequencies in the EB region averaged over the winter months. Shown are three-member ensemble means. Left panels: 20C (1961-2000); right panels: A1B (2160-2199).

3.3.3 Correlation analysis

In figure 3.3 we show associations between long lasting blocks close to Europe and selected temperature and precipitation extremes in 20C and A1B for winter (DJF). In 20C, a coherent pattern of anti-correlation between blocking frequency and seasonal minimum temperature (TNn) ranging from the Mediterranean Sea to northern Europe indicates very low nighttime temperatures in the presence of a block. In A1B, this pattern moves northeastward so that the Iberian Peninsula will be less affected by blocking episodes than in 20C. The seasonal maximum temperature (TXx) over
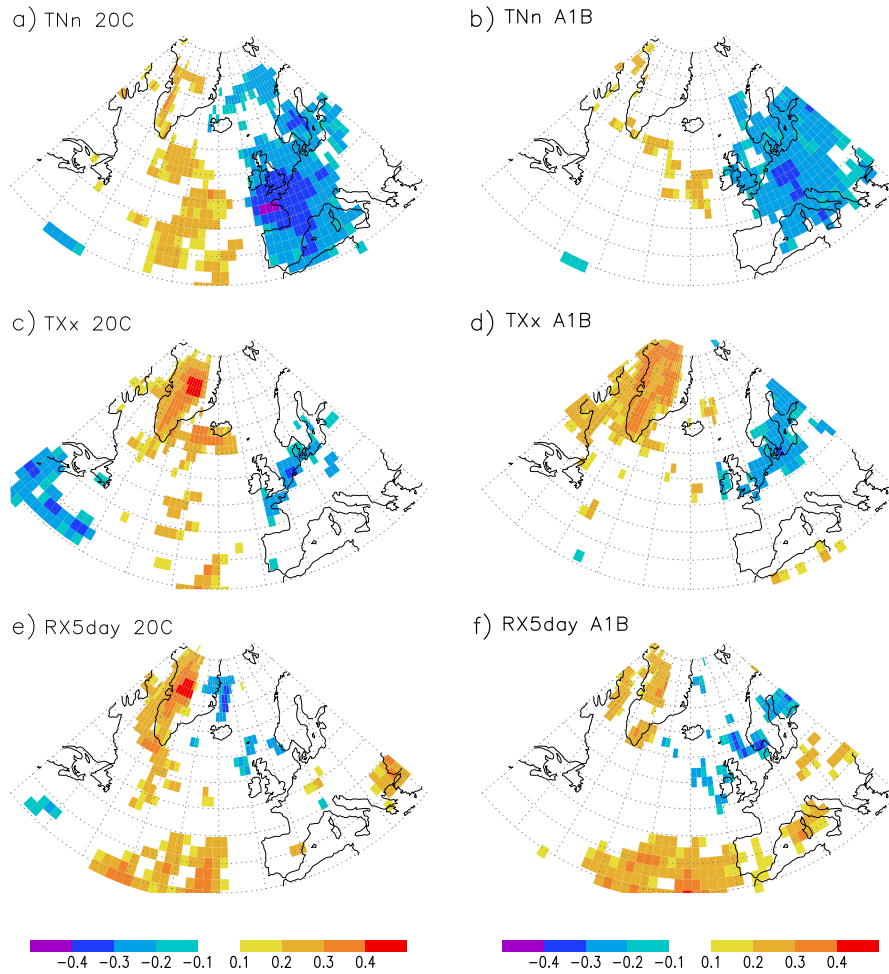
Figure 3.3— Spearman's rank correlation coefficients showing significant correlations at the 5% significance level for winter between blocking events in the EB region and extreme indices (a, b) TNn, (c, d) TXx and (e, f) RX5day. Left panels: 20C (1961-2000); right panels: A1B (2160-2199).

Europe is largely uncorrelated with the EB index but significant positive correlations are found over Greenland, as already suggested by the positive temperature anomalies in the composite pattern. In A1B, the positive correlations over Greenland persist while negative correlations over Europe cover a larger area than in 20C and are extended northeastward, similar to the TNn pattern.

The extreme precipitation index RX5day shows regions of positive correlation over Greenland and the North Atlantic, which bear some resemblance with the regions of positive anomalies in the composite maps. The Atlantic feature can be related to cyclonic systems at the southern flank of the block causing precipitation extremes in southern Europe. On the other hand, hardly any correlation is found in the core region where a coherent area of negative precipitation anomalies can be seen in the composite map. In A1B, more grid points showing anti-correlation appear over

northern Europe, but still no coherent pattern emerges. The positive correlations over Greenland diminish, but the pattern over the North Atlantic spreads eastward, impacting the coast of Portugal and part of the Mediterranean area.

The field significance test based on the FDR method reveals that the null hypothesis of no correlation can be rejected for all correlation patterns shown in figure 3.3, indicating that the correlations obtained with the Spearman's rank test are not an artifact of the chosen local test level.

3.4 Summary and concluding remarks

Using a dynamical PV-based blocking indicator we demonstrate that, compared to ERA-40, ECHAM5 simulates atmospheric blocking in the Euro-Atlantic region reasonably well with respect to location and frequency in both winter and summer. In winter, composite maps of 500hPa geopotential height, surface temperature and precipitation anomalies for high blocking frequencies close to Europe (15°W-30°E, 50°N-70°N) reveal a dipole structure with cold temperatures over Europe and warm temperatures over Greenland, in striking resemblance to the respective composites for the negative phase of the North Atlantic Oscillation index (Shabbar et al. (2001)). Furthermore, northerly flow anomalies to the east of the blocking core region and southerly flow anomalies to the west lead to dry (wet) conditions over Europe (Greenland).

These results are largely consistent with the correlations obtained between EB frequency and selected indices of extreme events. In particular, seasonal minimum temperatures over much of Europe are negatively correlated with EB frequency. This is primarily caused by the anomalous northerly flow but also by enhanced nighttime radiative cooling due to reduced humidity and cloudiness in the presence of blocking. The correlations for seasonal maximum temperature and seasonal maximum 5-day precipitation are somewhat weaker; but a field significance test shows that the correlation patterns in the Euro-Atlantic region are indeed significant. In summer, the null hypothesis of no correlation of the field significance test is accepted, probably due to the small sample size since blocking frequencies are well below 1% in the EB region.

In the A1B scenario, the frequency of winter blocks in the EB region is slightly diminished (by 8% on average). Fewer blocks are found in the southeastern sector of the domain but more in the northwestern sector. These changes in blocking frequency result in a shift of the associated Z500 anomaly from the northeastern North Atlantic to the Norwegian Sea so that a larger part of Europe is affected by anomalously cold and dry winter months, whereas the warm and wet anomalies over Greenland remain largely unchanged. In addition, a belt of negative Z500 anomalies evolves from Newfoundland to the Black Sea and beyond with enhanced precipitation relative to the A1B mean. Most of these results are reflected also in the correlation analysis between EB frequency and seasonal extremes of minimum temperature, maximum temperature and maximum 5-day precipitation during the

winter months. Compared to 20C, the respective correlation patterns move eastward and generally weaken due to the reduced number of blocks. As in 20C, positive correlations are found for the seasonal maximum temperature over Greenland, whereas the positive correlations between EB frequency and seasonal maximum 5-day precipitation around 40°N are spatially more coherent in A1B and affect also Mediterranean countries like Portugal, Spain and Italy.

In conclusion, although the frequency of Euro-Atlantic blockings is slightly diminished in A1B their influence on the European winter climate remains robust. Nevertheless, there are some systematic differences caused primarily by a northeastward shift of the European blocking pattern so that a larger part of Europe will experience anomalously cold events during the winter months than in the present climate. However, it is important to note that these anomalies are measured against the warmer mean winter climate simulated in the A1B scenario (Sillmann & Roeckner (2008)). The A1B projection also suggests a stronger indirect effect of European blocking episodes on the winter precipitation in southern Europe as a result of enhanced cyclogenesis at the southern flank of the block in a region where the mean precipitation is reduced compared to the present climate. Thus, in the A1B climate, blocking events tend to moderate the changes in both temperature and precipitation resulting from the anthropogenic increase in greenhouse gases. We should note, finally, that European blocking explains roughly 14% of the winter climate variability over Europe (cf. Pavan et al. (2000); Scherrer et al. (2006)). Thus changes in blocking occurrence can only be responsible for a small fraction of the projected changes in extremes events.

Chapter 4

Statistical modeling of winter temperature extremes in Europe including Euro-Atlantic atmospheric blocking as covariate[1]

Abstract

In this study, we apply a parametric approach to identify winter (DJF) temperature extremes in Europe using global climate model data. In particular, we fit the Generalized Extreme Value distribution (GEV) to monthly minima (maxima) of DJF minimum (maximum) temperatures in Europe. The behavior of the distribution's parameters and the 20-year return values are analyzed for 20th century and future climate ensemble simulations (represented by the SRES A1B emission scenario) using the ECHAM5/MPI-OM climate model. Furthermore, we test the hypothesis that climate extremes are influenced by certain large-scale atmospheric circulation patterns. We make an attempt to improve the fit of the GEV distribution to winter temperature extremes by conditioning the distribution's parameters on a covariate. In this respect atmospheric blocking acts as a prominent feature explaining parts of the European winter climate variability. We demonstrate that relating particularly the location parameter of the GEV distribution to atmospheric blocking improves the fit to the minimum temperature data in large areas of Europe with considerable impact on the 20-year return values. This relation remains robust under future climate conditions, however with less magnitude due to decreasing blocking frequency in A1B.

4.1   Introduction

In the last decades, changes in climate extremes became of major concern, because these events cause even higher financial and personal damages with growing population and technology standards in risk-prone areas than changes in the mean climate state (Beniston & Stephenson (2004)). It is thus of great interest to understand the mechanisms behind the occurrence of extreme climate events and to achieve reliable projections of their future changes (Meehl et al. (2000)). Coupled General Circulation Models (CGCM) are the state-of-the-art tools to simulate the present and future climate providing long data series necessary for the analyses of very rare extreme events (IPCC (2007)).

In this study, we make use of daily temperature data from climate simulations of a coupled atmosphere-ocean general circulation model to analyze global changes in the probability distribution of extreme climate events. We apply a parametric approach that considers the statistical behavior of the outermost tail of a climate variable's probability distribution. According to the extremal limit theorem (Fisher & Tippett (1928)), the maximum of a sample of independent and identically distributed (iid) variables converges asymptotically to one of three asymptotic extreme value distributions, which are combined in the Generalized Extreme Value (GEV) distribution, as sample length goes to infinity. This theorem holds for a wide class of distributions, and is therefore applicable to a lot of empirical time series. Leadbetter et al. (1983) extended this theory to non-stationary processes. Later, Coles (2001) proposed the inclusion of covariates in the GEV distribution. In the last years, this theory found application in climate research. Various studies (e.g., Kharin & Zwiers (2005); Nadarajah (2005); Nogaj et al. (2006, 2007); Kallache et al. (2007); Gaetan & Grigoletto (2007)) have implemented a time trend as covariate into the extreme value distribution to simulate the effects of anthropogenic climate change in the statistical modeling of extreme temperature and precipitation events.

In recent studies (e.g., Klein Tank & Koennen (2003); Haylock & Goddess (2004); Cassou et al. (2005)), it has been indicated that large-scale circulation patterns have an influence on the occurrence and distribution of extreme events. In this study we want to follow this argument by conditioning the GEV distribution on a covariate that is derived from a large-scale atmospheric circulation pattern. Katz et al. (2002) have emphasized that if one successfully applies the GEV distribution with an appropriate covariate arising from a large-scale atmospheric variable, this can be viewed as statistical downscaling approach for CGCM data. However in climate research, only very few attempts have been undertaken so far to include covariates other than time into the GEV distribution; most of them concentrating on hydrological applications (Coles (2001); Katz et al. (2002); Wang et al. (2004); Chavez-Demoulin & Davison (2005); El Adlouni et al. (2007)). Thus, with this study we are trying to make a step towards the approach proposed by Katz et al. (2002).

We particularly concentrate on the European continent and its winter climate that can be strongly influenced by atmospheric blocking conditions (e.g., Rex

(1950b); Beniston et al. (1994)). Atmospheric blocking disturbs the predominant westerly flow over Europe and the anti-cyclonic conditions associated with it allow a northeasterly inflow of cold and dry air masses. This leads to persistent clear sky conditions favoring increased out-going long wave radiation during winter nights, which result in a strong cooling of the earth surface and anomalous cold surface temperatures (e.g., Rex (1951); Trigo et al. (2004)). Sillmann & Croci-Maspoli (2008) further showed that atmospheric blocking conditions not only influence the mean winter climate, but also are associated with extreme temperature events in the Euro-Atlantic region. Hence, we want to investigate in this study, whether the fit of the GEV distribution to daily extreme winter temperature data can be improved by conditioning the GEV parameters on a covariate derived from an atmospheric blocking indicator.

The study is organized as follows. In section 4.2, we describe the model and data we have used for our analysis and introduce the blocking indicator in more detail. Section 4.3 concentrates on the methodology of the applied GEV distribution for stationary and non-stationary processes. The results of our analysis are shown and discussed in section 4.4. In the last section, we summarize the results and give an outlook for further studies that could complement our work.

4.2   Model simulations and blocking indicator

4.2.1   ECHAM5/MPI-OM model simulations

We use climate simulations from the CGCM ECHAM5/MPI-OM (Jungclaus et al. (2006)) developed at the Max Planck Institute for Meteorology (Hamburg, Germany). The atmospheric component of the model (ECHAM5: Roeckner et al. (2003)) has a horizontal resolution of T63 in spectral space (corresponding to $1.875°$ x $1.875°$ in grid point space) and 31 vertical levels. The oceanic component (MPI-OM: Marsland et al. (2003)) is a z-coordinate GCM with integrated sea-ice model and has a nominal horizontal resolution of $1.5°$ and 40 vertical levels. The coupling of the atmosphere to the ocean component requires no flux adjustments.

For our analyses, we use daily (2-meter) minimum (T2MIN) and maximum (T2MAX) temperature data generated from ensemble simulations (each with 3 ensemble members) of the ECHAM5/MPI-OM model for the present and future climate. For the 20th century simulations, greenhouse gases (GHG) and sulfate aerosols are prescribed according to observations and chemical transport model results, respectively. The scenario simulations are forced according to the SRES emission scenario A1B as described in Nakicenovic & Swart (2000). Each A1B ensemble member is a continuance of the corresponding 20C ensemble member.

We particularly concentrate on the winter months (DJF) in two 40-year time slices in this study. The first is taken from the present climate simulation ranging from 1961-2000 (hereinafter referred to as 20C). The second time slice, ranging from 2160-2199, is taken from the stabilization period of the SRES scenario A1B, where

a) ERA−40

b) 20C

c) A1B

0.5   1   1.5   2   2.5   3   3.5   4
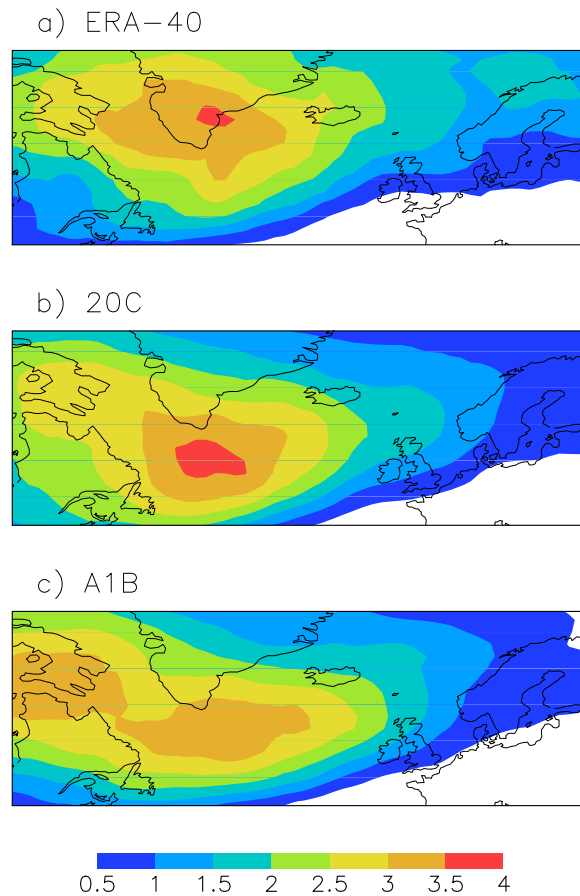
Figure 4.1— Climatology of the Euro-Atlantic (80°W-30°E, 45°N-75°N) atmospheric blocking frequencies [%] for a) ERA-40 and b) the ensemble mean of the 20C simulations (1961-2000) and c) the A1B simulations (2160-2199) of the ECHAM5/MPI-OM.

the atmospheric composition is kept constant at the level of year 2100. The latter is referred to as A1B hereinafter.

4.2.2   The blocking indicator

To capture atmospheric blocking conditions in the ECHAM5/MPI-OM model, we apply a dynamical blocking indicator introduced by Schwierz et al. (2004). It is based upon the three-dimensional potential vorticity (PV) anomaly field averaged on tropopause level. The blocking indicator is calculated in two steps: first by computing the vertically averaged PV between 500 and 150hPa and second by tracking the negative PV anomalies. Anomalies are calculated relative to the long-term climatology over the time period 1961-2000 and 2160-2199 for 20C and A1B, respectively. Structures of negative PV anomalies that have a minimum spatial extension of $1.8 \cdot 10^6 \text{km}^2$ and that persist longer than 10 days are captured as block at every in-

stance of time (6-hourly). The blocking frequency is then defined as the percentage of the number of blocked days at a given grid point compared to a total number of days considered. For more details about the blocking indicator and its application to ERA-40 re-analysis data (Uppala et al. (2005), ERA-40 hereinafter), the reader is referred to Croci-Maspoli et al. (2007a,b). A comparison between blocking events derived by the PV-based blocking indicator in ERA-40 and the present and future climate simulations of the ECHAM5/MPI-OM model can be found in Sillmann & Croci-Maspoli (2008).

In comparison to other blocking detection methods using the meridional gradient of the geopotential height (e.g., Lejenaes & Okland (1983); Tibaldi & Molteni (1990)) or surface pressure anomalies (e.g., Elliott & Smith (1949); Dole & Gordon (1983)), the PV-based blocking indicator is able to capture the dynamical features (e.g., spatial extension, life cycle, geographical location and movement) of the atmospheric blocking phenomenon in its entire range (Schwierz et al. (2004)).

The winter (DJF) blocking climatology of Euro-Atlantic blocks (80°W-30°E, 45°N-75°N) used in this study is shown in figure 4.1 for ERA-40 in comparison with the ensemble mean of the ECHAM5/MPI-OM simulations of 20C and A1B. The model agrees well with ERA-40 in respect to the spatial distribution and representation of blocking frequency in present climate. However, the center of maximum blocking frequency is located further south in the model leading to higher blocking frequencies between Iceland and the British Isles. Because of these differences we cannot limit or study to European blockings (15°W-30°E, 50°N-70°N) as proposed in Sillmann & Croci-Maspoli (2008), but have to consider the entire Euro-Atlantic blocking region to be able to compare the model results with ERA-40. In A1B (Fig. 4.1c), the blocking frequency is diminished south of Greenland, but increased towards north-western Canada compared to the present climate.

4.3 Methodology

4.3.1 GEV distribution for stationary processes

We briefly revisit the extreme value theory here to provide a basis to our assessment of extreme temperature events in climate model data. A detailed review on extreme value theory in climate research can be found e.g., in Palutikof et al. (1999); Coles (2001); Katz et al. (2002). In this study, we apply the Generalized Extreme Value (GEV) distribution as described in detail in Coles (2001) to seasonal and monthly extremes in time series of the minimum and maximum 2-meter temperature. We follow the block maxima approach,

$$M_n = max\{X_1, X_2, \cdots, X_n\} \tag{4.1}$$

where M_n are the maxima drawn from a series of random variables X_i, for i=1,,n, over a number of defined time blocks (e.g., month, season, year). In this study we chose the time blocks to be a winter month (December, January, and February) or
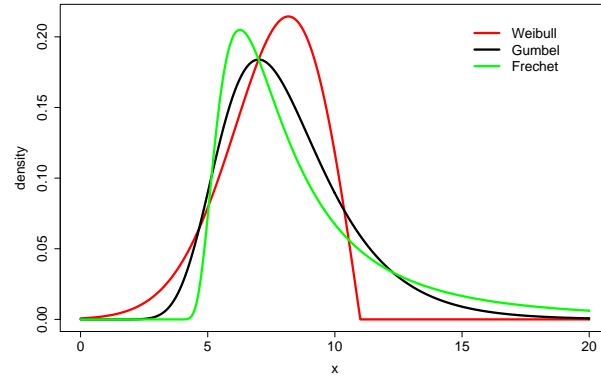
Figure 4.2—— GEV distribution with varying shape parameter (red: ξ = -0.5, black: ξ = 0, green: ξ = 0.5) for a location μ=7 and scale σ=2, consisting of the Weibull, Gumbel and Fréchet distribution, respectively.

a winter season (DJF). For the minima, we follow the approach outlined by Coles (2001), letting $Y_i = -X_i$, for i=1,...,n, thus modifying Eq. 4.1 to

$$M_n = max\{Y_1, Y_2, \cdots, Y_n\} \tag{4.2}$$

Small values of X_i, hence correspond to large values of Y_i due to the sign change.

According to the Fisher-Tippett theorem (Fisher & Tippett (1928)), the distribution of M_n asymptotically (i.e., as the block size n goes to infinity) converges towards the GEV distribution with a non-degenerate distribution function G, representing a member of the GEV family:

$$G(x) = exp\{-[1 + \xi(x - \mu)/\sigma]^{\frac{-1}{\xi}}\} \tag{4.3}$$

defined on $\{x: 1 + \xi(x - \mu)/\sigma > 0\}$, where $-\infty < \mu < \infty$, $\sigma > 0$ and $-\infty < \xi < \infty$. However, for values of ξ below -0.5, the maximum likelihood estimators become difficult or unlikely to obtain according to Coles (2001).

The GEV distribution has three parameters μ, σ and ξ, which denote the location, scale and shape of the distribution function, respectively. The shape parameter ξ distinguishes between three distribution functions, which are summarized by the GEV distribution. The influence of this parameter on the shape and particularly on the tail of the GEV distribution can be exemplarily seen in figure 4.2. The Gumbel distribution, for $\xi = 0$, is a special case of the GEV distribution. The Weibull (bounded tail) or Fréchet (heavy-tailed) distribution occurs if ξ is less or greater than zero, respectively. Generally spoken, the location parameter determines the overall position and the scale parameter the spread of the distribution. Changes in the location parameter, thus, imply a change in the mean value and changes in the scale parameter, being a measure of variability, stretch or shrink the distribution (cf. Fig. 2 in Goubanova & Li (2007)).

Parameter estimation

Most common methods for parameter estimation in climate research are the Maximum Likelihood (ML) estimation (e.g., Katz et al. (2002, 2005)) and the method of L-Moments (e.g., Hosking (1990); Zwiers & Kharin (1998)). A comparison of these methods is discussed in Coles & Dixon (1999). The ML method, although problematic when applied to very small samples (n<25), is the preferable method due to its universal applicability, i.e. for the presence of covariates in non-stationary data (Coles (2001); Katz et al. (2005)). Thus, the parameters of the GEV distribution are estimated by the ML estimation (see Coles (2001) for more details) in this study.

Goodness-of-fit test

To examine whether the GEV distribution is able to represent the extreme temperature data, a standard Kolmogorov-Smirnov (KS) test (Stephens (1970)) is applied. This test measures the overall differences between two (cumulative) distribution functions:

$$Diff = max|F(x) - G_N(x)|, \tag{4.4}$$

where F(x) is the theoretical distribution, which we fit to the data, and G_N(x) the empirical distribution function estimated from a sample of size N. When the maximum *Diff* exceeds a certain critical value, then the null hypothesis, that the observed extremes are drawn from the fitted distribution F(x), is rejected.

Because the theoretical distribution is not known, but has to be estimated by a fit to the data, the standard critical values of the KS test are not applicable here. Therefore, to obtain the significance levels for the distribution of *Diff*, we apply a parametric bootstrap procedure (e.g., Kharin & Zwiers (2000); Goubanova & Li (2007)). In this procedure, 1000 samples of the same size as the modeling series of extremes (120 for monthly DJF extremes) are generated from each fitted GEV distribution and *Diff* is derived from each generated sample. The 95th quantile of the resulting distribution of $Diff_i$, i=1:1000, is employed as the critical value for the rejection of the null hypothesis at the 5% significance level.

Return Values

Extremes can also be expressed by return values, which summarize the behavior of the parameters and can further describe the changes in extreme events. The T-year return value X_T, which is defined as the $(1\text{-}1/\text{T})^{th}$ quantile, can be derived from the quantile function by inverting the fitted GEV distribution function:

$$X_T = \begin{cases} \mu - \frac{\sigma}{\xi}\{1 - [-ln(1 - \frac{1}{T})]^{-\xi}\}, & \xi \neq 0 \\ \mu - \sigma ln[-ln(1 - \frac{1}{T})], & \xi = 0 \end{cases} \tag{4.5}$$

In this study, we calculate 20-year return values (RV20 hereinafter) for the 20C and A1B time slices. We chose 20-year return values as an example to illustrate the

influence of the covariate (cf. section 4.3.2) on the return values. The confidence intervals (thus sampling errors) are rather small compared to return periods (e.g. 100 years) that exceed the time slice length of 40 years, which can be chosen to extrapolate extreme events beyond the observed time period. In this study, however, we indicate future climate change by taking a time period of the 20C and compare it with a time period in the climate scenario A1B. Significant differences between the two periods are determined by calculating the 90% confidence intervals of the 20C RV20 using a parametric bootstrap approach, where 1000 samples (of size 120) are generated from the fitted GEV distribution. The 5th and 95th percentiles of the distribution of $RV20_i$, i=1:1000, derived from the generated samples are used as lower and upper bounds for the 90% confidence interval of the RV20 from the initial sample. Accordingly, changes in the A1B RV20 are statistically significant at the 10% significance level if the A1B RV20 does not fall within the 90% confidence interval of the 20C RV20. The significance of changes in the GEV parameters (location, scale, and shape) is defined in the same manner.

4.3.2   GEV distribution for non-stationary processes

The extreme value theory as described in section 4.3.1 can be extended to non-stationary processes by including covariates in the GEV distribution as shown exemplarily in the following equation (e.g. Coles (2001)):

$$F(x|COV(t) = z) \sim GEV(\mu(z), \sigma(z), \xi(z)) \tag{4.6}$$

where the parameters of the GEV distribution are conditioned on a (time varying) covariate (COV(t)). In climate research, commonly a linear time trend is applied as covariate in the extreme value distribution, as already referenced in section 4.1, to include anthropogenic climate change in the extreme value modeling. In this study however, we are making an attempt to include a large-scale atmospheric circulation pattern into the modeling of extreme temperature events in Europe to investigate whether this can improve the fit to the GEV distribution. We particularly concentrate on atmospheric blocking (see section 4.2.2) as covariate, since various studies have pointed out the importance of atmospheric blocking to the European winter temperatures (e.g., Rex (1951); Beniston et al. (1994); Trigo et al. (2004)). A field average over the Euro-Atlantic domain (80°W-30°E, 45°N-75°N) is calculated for the respective time slice (20C and A1B) to be able to use the information gained from the atmospheric blocking indicator (cf. section 4.2.2) as covariate.

We assume the relationship between the location (and the log-transformed scale parameter) and the covariate atmospheric blocking (CAB hereinafter) to be linear:

$$\mu(t) = \beta_0 + \beta_1 \cdot CAB(t) \tag{4.7}$$
$$ln\sigma(t) = \gamma_0 + \gamma_1 \cdot CAB(t) \tag{4.8}$$

The choice of a linear inverse link function can be justified by a study of Sillmann & Croci-Maspoli (2008) that implies the existence of a monotone association between

European blocking and temperature extremes in Europe. Following other studies (e.g., Katz et al. (2002); Kharin & Zwiers (2005)), we implement a log-transformed scale parameter to ensure that this parameter remains positive.

The rate of change in the mean of the analyzed temperature extremes per change in blocking frequency is described by parameter β_1 in Eq. 4.7. If we assume $\beta_1 = 0$, we receive a homogeneous model over time with $\mu(t) = \beta_0$.

The shape parameter will not be conditioned on CAB in this study, because of the difficulties in estimating and interpreting changes of this parameter with time correctly. A shape parameter that changes its sign over time would imply that the underlying distribution of the temperature values changes. Such behavior is not in the focus of this study. Thus, we restrict the shape parameter to be constant with time within each time slice (for 20C and A1B, respectively).

We set up a collection of nested models, where one or more parameters of the GEV distribution are conditioned on CAB. Table 4.1 summarizes the model collection. The degree of freedom (d.f.) for each model corresponds to the number of parameters in the respective GEV distribution function.

Table 4.1— Model collection of the GEV distribution for the stationary case (model 0) and the non-stationary case (model 1, 2), where one or more parameters are conditioned on CAB and their corresponding degrees of freedom (d.f.).

Model	μ	σ	ξ	GEV distribution function	d.f.
0	0	0	0	$F(x) \sim \text{GEV}(\mu, \sigma, \xi)$	3
1	CAB	0	0	$F(x\vert \text{ CAB}(t)=z) \sim \text{GEV}(\mu(z), \sigma, \xi)$	4
2	CAB	CAB	0	$F(x\vert \text{ CAB}(t)=z) \sim \text{GEV}(\mu(z), \sigma(z), \xi)$	5

Model selection

In the literature exist various methods to identify the best model out of a set of cautiously selected candidate models. One approach involves the information criteria, e.g. the Bayesian information criterion (BIC, e.g. Katz et al. (2005)), the Akaike information criterion (AIC, e.g. Burnham & Anderson (2003)), and the Hannan-Quinn information criterion (HIC, e.g. Grasa (1989)). All of these criteria are based on the Maximum Likelihood (ML) associated to each candidate model, but vary with the emphasis put on the number of parameters to be estimated and the sample size. Another approach is the deviance statistic (DEV), which is a statistical test based on the Maximum Likelihood ratio test (e.g. Coles (2001)). In contrast to the information criteria, we can associate a significance level to the results of this statistical test.

In this study we concentrate on DEV since it is appropriate for comparing nested models fitted by ML (Coles (2001)). We use DEV to find out whether the stationary model or one of the non-stationary models (cf. Table 4.1) is best to describe the

underlying data. According to our analysis (not shown), the HIC provided the most similar results compared to the DEV.

The deviance statistic (Eq. 4.9) distinguishes between the negative log-likelihood (nllh) of two models, M_0 and M_1 (likelihood ratio test):

$$D = 2\{nllh_0(M_0) - nllh_1(M_1)\} > c_\alpha \qquad (4.9)$$

Let model M_0 be a subset of model M_1 by limiting the d.f. in M_0 (e.g., by constraining some of the parameters to be zero). This means M_1 is the more complicated model with higher degrees of freedom. The simplest model would be the stationary case (model 0), where all 3 parameters are constant with time. The deviance (D) is, for a sufficient large sample size, approximately χ_k^2 distributed with k degrees of freedom. Here k is equal to the difference in degrees of freedom between the two models compared. As described in Coles (2001), we can test the validity of model M_0 relative to M_1 at the α level of significance and reject M_0 in favor of M_1 if $D > c_\alpha$, where c_α is the (1-α) quantile of this χ_k^2 distribution.

We estimate the parameters of each candidate model by the ML technique as described in section 4.3.1 and evaluate D for each candidate model. If D falls above c_α, with $\alpha = 0.1$ in this study, then model M_1 explains more variation in the data than model M_0 at the 10% significance level.

4.4   Results

4.4.1   Stationary GEV distribution

Here we compare the results of fitting the stationary GEV distribution to extreme winter minimum and maximum temperature data over land from the 20C ensemble simulation of the ECHAM5/MPI-OM model with data of the ERA-40 re-analysis. We decided to choose monthly instead of seasonal DJF block minima (maxima) of 40-year (1961-2000) minimum (maximum) temperature time series to receive 120 instead of 40 resulting blocks to which the GEV distribution is fitted. Compared to the seasonal DJF block minima (maxima), the standard error (s.e.) of the shape parameter ξ, which is the most delicate parameter to estimate, is reduced by a factor of 2 as also described in Parey (2008). Table 4.2 shows, exemplarily for the minimum temperature extremes, the beneficial effect of the reduction of block length on the GEV parameters for the 20C ensemble mean spatially averaged over Europe (resembling the behavior at each grid point).

Goodness-of-fit tests

To assess whether it is adequate to assume a GEV distribution for monthly maxima or minima, the Quantile-Plot (QQ-Plot) is exemplarily shown for one grid point as a typical result for European land areas in both 20C and A1B (Fig. 4.3). The QQ-Plot is a useful tool to visualize the goodness-of-fit of a distribution by comparing the

Table 4.2— GEV parameters and their standard errors (s.e.) for seasonal and monthly block length for the ensemble mean of the 20C model simulation averaged over land grid-points in Europe. The GEV distribution was fitted to block minima of T2MIN.

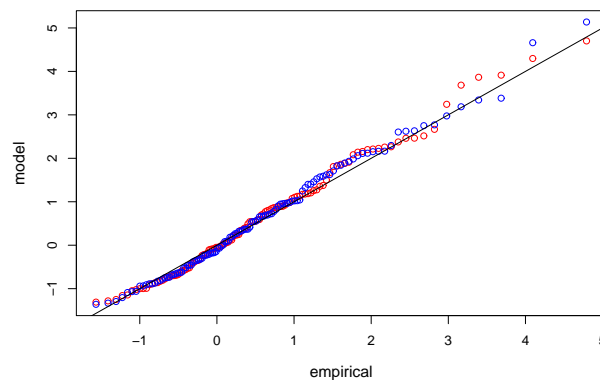| Block length	μ (s.e.)	σ (s.e.)	ξ (s.e.)
seasonal DJF ($\sim$90days)	-17.6 (0.580)	3.29 (0.418)	-0.233 (0.113)
monthly DJF ($\sim$30days)	-13.8 (0.435)	4.33 (0.306)	-0.247 (0.056)

Figure 4.3— Quantile- (QQ-) Plot of the empirical data and the fitted stationary (blue points) and Gumbel scaled non-stationary model (red points) for the extreme T2MIN of 20C at grid point 24°E and 53°N. In the non-stationary model, the location parameter is dependent on CAB (cf. Table 4.1, model 1)

quantiles of the fitted distribution to those of the empirical data. The quantiles of the fitted stationary and non-stationary GEV distribution (Gumbel scaled, according to Coles (2001)) are distributed closely around the diagonal line, indicating that the GEV distribution is a good fit to monthly T2MIN block minima even for the tails of the distribution.

Another goodness-of-fit test of the GEV distribution is the Kolmogorov-Smirnov test (cf. section 4.3.1). In figure 4.4 we show a comparison of the GEV parameters and the RV20 between the 20C ensemble mean and ERA-40 for the extreme T2MIN. Grid-points (over land), where the null hypothesis (extremes are drawn from the fitted distribution) of the KS test is rejected, remain blank. We keep this procedure also for the non-stationary GEV distribution in section 4.4.2. Since there are only very few points in figure 4.4, where the null hypotheses is rejected for the 20C model simulations, the GEV distribution can be considered as an overall good representation of the extreme winter minimum temperature in Europe. For ERA-40, the KS test failed at most grid-points over the Iberian Peninsula and northwestern France.
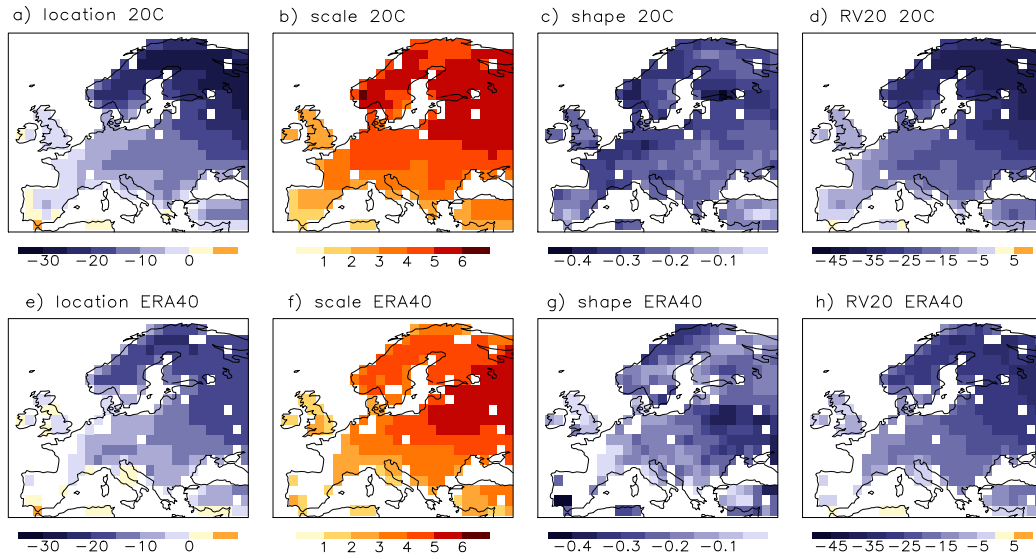
Figure 4.4— GEV parameters (location [°C], scale, and shape) and 20-year return values RV20 [°C] for the monthly minimum temperature extremes in DJF of the 20C ensemble mean and the ERA-40 data for the time period 1961-2000. Grid-points over land where the KS test failed are left blank.

GEV distribution parameters and RV20

As shown in figure 4.4, there is an overall good agreement in the spatial patterns of the GEV parameters and the RV20 between the 20C and ERA-40. A distinct north-south gradient can be seen with higher (lower) values in the south and lower (higher values) in the north for the location (scale) parameter (Fig. 4.4a, b (e, f)). This gradient reflects the overall spatial European temperature pattern with generally warmer temperatures and less variability in the south and colder temperatures and higher variability in northern Europe. In Scandinavia, however, the location parameter of the GEV distribution fitted to the 20C simulations is lower (-5°C on average) and the scale parameter higher than for the ERA-40 re-analysis. This indicates that the model simulates colder extreme T2MIN with higher variability in northern latitudes than ERA-40. The shape parameter is always negative (within the standard error), indicating a Weibull distribution, for both 20C and ERA-40 data.

The RV20, combining the information of the three individual GEV parameters, reveals also a north-south gradient with lower return values in the north and higher values in the south. The reduced location parameter over Scandinavia is also reflected in lower RV20 in that area for the 20C. For the extreme T2MAX, as depicted by figure 4.5, the GEV parameters and the RV20 of 20C and ERA-40 show a reversed gradient compared to T2MIN. The location parameter (Fig. 4.5a, e) is highest in southern Europe, decreasing northward. The same holds for the RV20 (Fig. 4.5d, h). The values for scale (Fig. 4.5b, f) and shape (Fig. 4.5c, g) parameters in
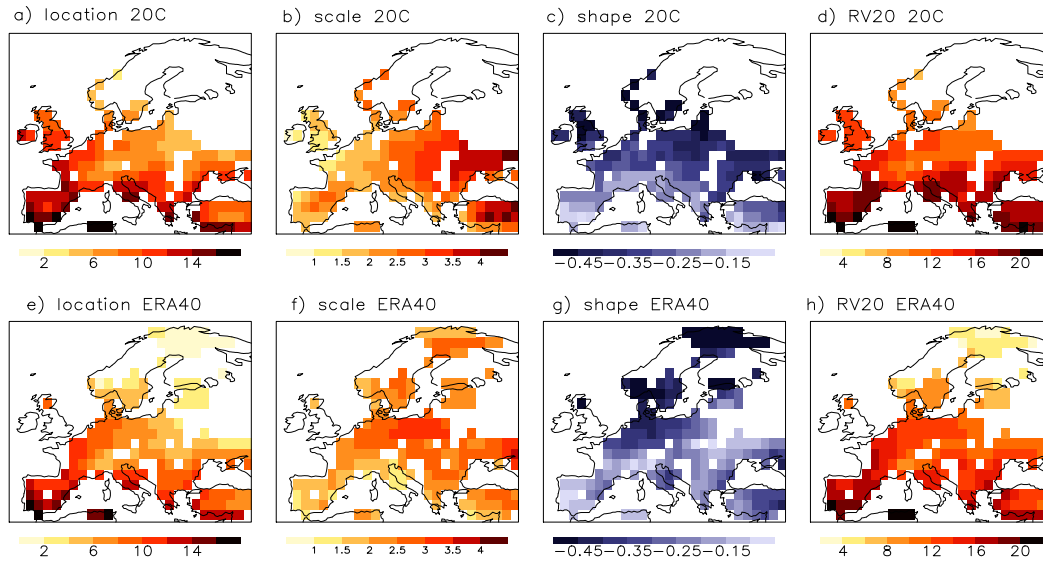
Figure 4.5— As figure 4.4, but for DJF maximum temperature extremes.

20C and ERA-40 are comparable and increase from south to north. However, since the null hypotheses of the KS test is rejected for most grid points in northeastern Europe (20C and ERA-40) and the British Isles (ERA-40), the GEV distribution cannot be considered as an overall good representation for extreme winter T2MAX. Thus, in the following, we will not further discuss the results for extreme T2MAX temperatures.

In figure 4.6, we illustrate significant changes (10% significance level) in the GEV parameters as well as in RV20 between 20C and A1B for extreme winter T2MIN. The changes in the location parameter (Fig. 4.6a) are significant almost all over Europe with large increase (12°C-14°C) in northeastern Europe and smaller increase (2°C-4°C) in southwestern Europe. The scale parameter (Fig. 4.6b) decreases significantly in parts of Europe reaching from the British Isles to southeastern Europe, indicating less variability in these regions under future climate conditions. The shape parameter (Fig. 4.6c) does not reveal significant changes in most parts of Europe and remains negative (-0.02) even for the greatest increase of 0.257 in central Europe. Thus, extreme T2MIN remain Weibull distributed in A1B.

The changes in the RV20 (Fig. 4.6d) are significant throughout Europe and are comparable with the changes in the location parameter. There is a large increase in the return values (up to 16°C) in northeastern Europe and smaller increase towards southwestern Europe (5°C on average). This overall increase of RV20 indicates also an increase in the waiting time of a certain T2MIN extreme event.
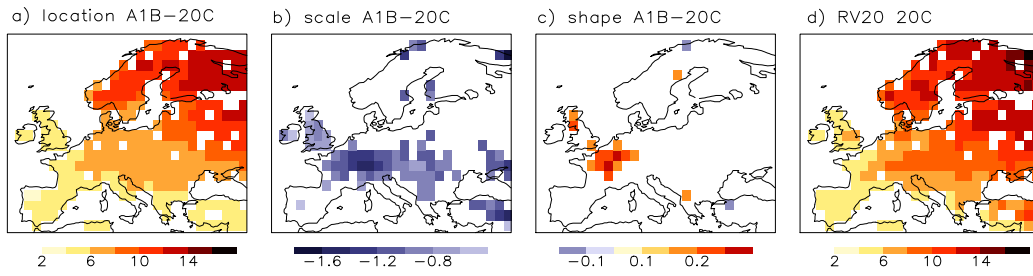
Figure 4.6— Significant difference of the GEV parameters (location [°C], scale, shape) and RV20 [°C] for T2MIN between the ensemble mean of the A1B (2160-2199) and 20C (1961-2000) model simulations.

4.4.2　Non-stationary GEV distribution

GEV distribution parameters

In this part, we include atmospheric blocking as covariate into the GEV distribution of monthly DJF extreme T2MIN. According to table 4.1, we have set up a collection of models, where one or more parameters of the GEV distribution are linked to the CAB. For each grid point over land in Europe, the best model is determined by means of the Deviance statistic (DEV, cf. section 4.3.2) taking into account the negative maximized log-likelihood (nllh) associated with each model.

As an example for this procedure, we show a summary of the results of fitting different models to the extreme T2MIN of ensemble member 20C1 at one grid-point (at 9°E, 53°N) in table 4.3. Model 1 was selected as best model at this grid point, although model 2 has a slightly smaller nllh. However, the difference D = $2\{\text{nllh(model2)-nllh(model1)}\} = 0.46$ is not significantly large enough on the scale of the χ^2_k distribution (for k=1) to explain substantially more of the variability in the data.

Table 4.3— Negative maximized log-likelihoods (nllh) and parameter estimates with standard errors (s.e.) for the model collection (cf. table 4.1) of the stationary (model 0) and non-stationary GEV distribution (model 1, 2) at grid point 9°E, 53°N.

Model	nllh	μ (s.e.)		σ (s.e.)		ξ (s.e.)
0	353.38	-9.23		4.51		-0.232
		(0.45)		(0.31)		(0.051)
1	349.17	-8.61	-0.36	4.33		-0.227
		(0.49)	(0.12)	(0.30)		(0.051)
2	348.94	-8.61	-0.35	1.49	-0.014	-0.22
		(0.48)	(0.09)	(0.075)	(0.021)	(0.056)

In figure 4.7 we display the results of the model selection via DEV for all land grid points in Europe for each 20C ensemble member (Fig. 4.7a-c) in comparison with ERA-40 (Fig. 4.7d). Grid points were the KS test (cf. section 4.3.1) failed
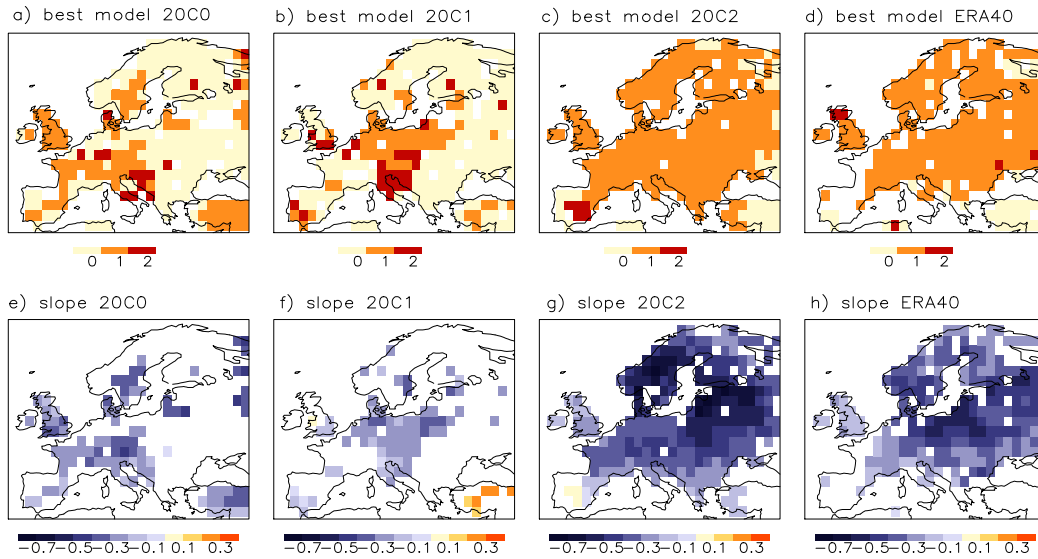
Figure 4.7— Best model (a-d) selected with the deviance statistic for each 20C ensemble member and ERA-40, and the corresponding slope of the location parameter (e-h). See text for more details.

are left blank. We can see large differences between the individual ensemble members. Only one ensemble member (20C2) agrees very well with ERA-40 with model 1 being selected as best model in most parts of Europe. This implies that atmospheric blocking (linked to the location parameter) explains a substantial part of the variability in the data. In the other two ensemble members 20C0 and 20C1, the stationary model (model 0) is predominantly the best model. In 20C0, model 1 is chosen as best in central western Europe, southern Scandinavia and on the British Isles, whereas in 20C1 only central Europe shows a coherent area with model 1 as best. Model 2 appears to be best at some scattered grid points in each 20C ensemble member and ERA-40, but does not reveal a preferred spatial pattern or location. Thus, the choice of model 2 might be an artifact of the chosen significance level α =0.1 for the DEV, which allows 10% of the test results to be erroneously correct. Consequently, the model selection for the 20C and ERA-40, as depicted in figure 4.7a-d, imply that either the stationary model or model 1 are best to describe the variability in the underlying data. This also indicates that atmospheric blocking influences primarily the location parameter of extreme T2MIN.

In model 1 the location parameter of the GEV distribution is linearly linked to the CAB as shown in Eq. 4.7. Hence, the parameter β_1 (Eq. 4.7) describes the slope of the linear association between the location parameter and atmospheric blocking. The slope is, in this particular analysis, an expression for the change in temperature [°C] per change in blocking frequency. Since blocking frequency does not have a unit, the unit of the slope is °C. Figure 4.7e-h illustrates that the slope is predominantly negative (except at very few grid points in southern latitudes) for both the 20C ensemble members and ERA-40. Here again, ensemble member 20C2
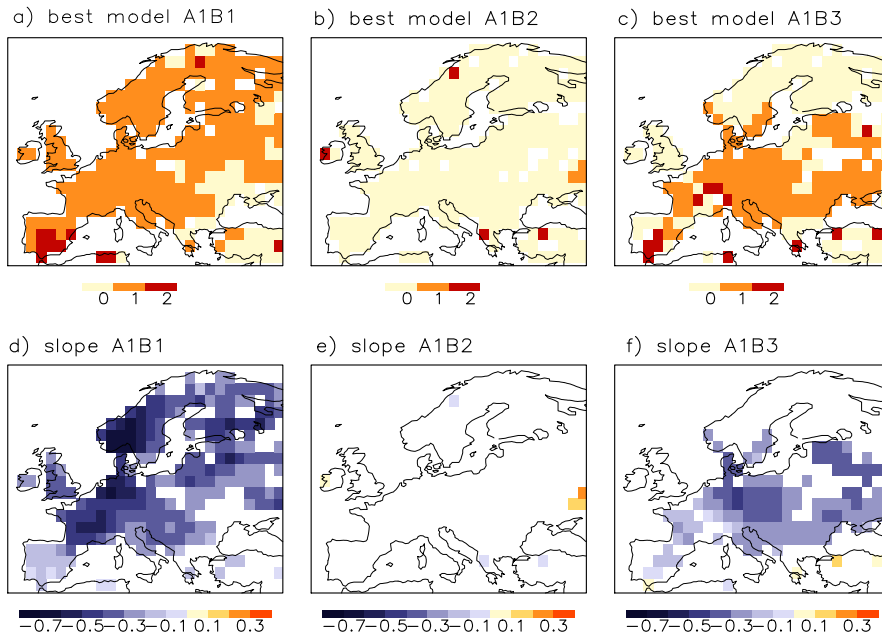
Figure 4.8— As figure 4.7, but for the A1B ensemble members.

and ERA-40 agree very well, although the values for the slope are less negative for ERA-40 (minimum at -0.57°C) than for 20C2 (minimum at -0.75°C). A negative slope implies that with increasing blocking frequency we can expect lower extreme T2MIN. For example, for a slope of 0.5°C we can expect a decrease in location parameter of 0.5°C per 1% increase in blocking frequency. The greatest absolute values for the slope can be found around the Baltic Sea in 20C2 and ERA-40. The other two ensemble members show comparably weaker values for the slope (20C0 minimum at 0.45°C; 20C1 minimum at 0.4°C).

In A1B, as depicted in figure 4.8a-c, model 1 is also selected as best model in large parts of Europe in 2 ensemble members, whereas in one ensemble member (A1B2) the stationary model represents the underlying data best. As already seen in the 20C ensemble, the slope for the location parameter in the A1B ensemble (Fig. 4.8d-f), in particular A1B1 (minimum at 0.64°C) and A1B3 (minimum at 0.41°C), is mainly negative within the same range as in 20C.

Return Values

In the following we will have a closer look on the influence of CAB on the 20-year return values (RV20) for ERA-40 and the 20C and A1B ensembles. Since RV20 for non-stationary GEV distribution varies over time according to the blocking frequency at each time step, we have to determine RV20 for a certain time step within the time period analyzed. Hence, we calculated RV20 at the time point where the maximum blocking frequency occurred in 20C or ERA-40 (1961-2000) and A1B
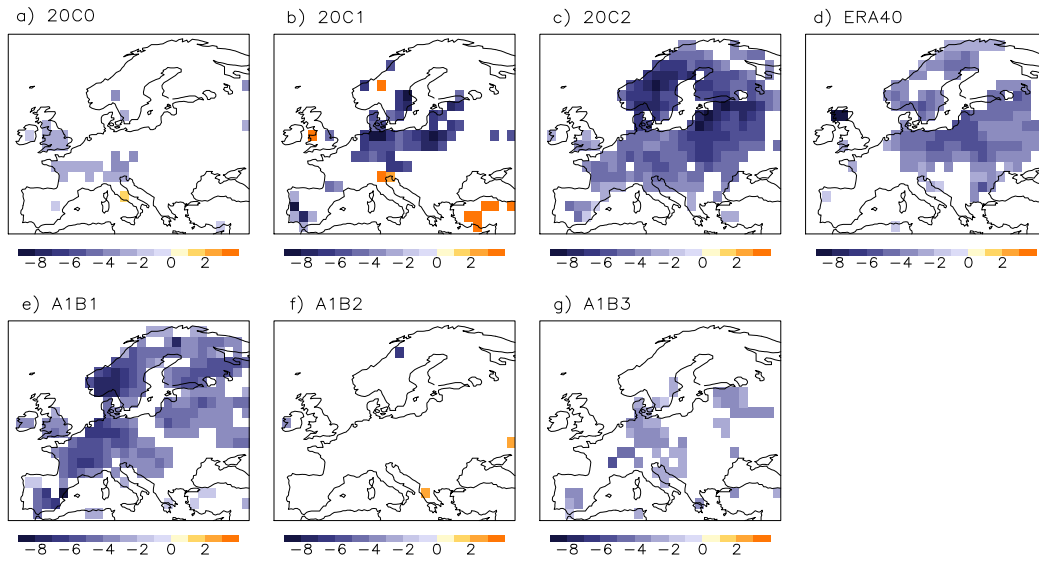
Figure 4.9— Significant differences between RV20nonstat [°C] and RV20stat [°C], considering the month with the highest blocking frequency within 1961-2000 for the 20C ensemble members (a-c) and ERA-40 (d) and within 2160-2199 for the A1B ensemble members (e-f).

(2160-2199), respectively.

To illustrate the influence of the covariate on the return values of a non-stationary model compared to a stationary model, we calculate the difference between RV20 from the stationary model (RV20stat hereinafter) and the non-stationary model (RV20nonstat hereinafter) at those grid points, where the non-stationary GEV distribution (model 1 or 2) was selected as best. Changes between RV20stat and RV20nonstat are only counted as significant if the change in RV20 is larger than the 90% confidence interval of the RV20stat (cf. section 4.3.1).

It becomes obvious from figure 4.9 that in 20C, ERA-40, and in A1B the RV20nonstat are generally reduced compared to RV20stat at those grid points where model 1 is selected as best model. This indicates that if considering a blocking event in a winter month, the waiting time for a particular extreme T2MIN event will be reduced compared to the stationary case. Hence, we can anticipate colder minimum temperatures in that month. The range of this reduction varies, however, considerably between the ensemble members of 20C and A1B as well as ERA-40. This result depends strongly on the maximum blocking frequency encountered in each ensemble member and ERA-40, because the stronger the blocking frequency the stronger the differences in RV20. For example, the maximum blocking frequency of 20C2 and A1B1 is 14% compared to 10% in 20C0 and A1B3 (where 10% blocking frequency means approx. 3 blocked days per month). The maximum blocking frequency in ERA-40 is 12%. The highest blocking frequency of 27% occurred in 20C1 (Fig. 4.9b). Here, we also see the largest differences ($> 9°$C) in RV20 in central Europe.

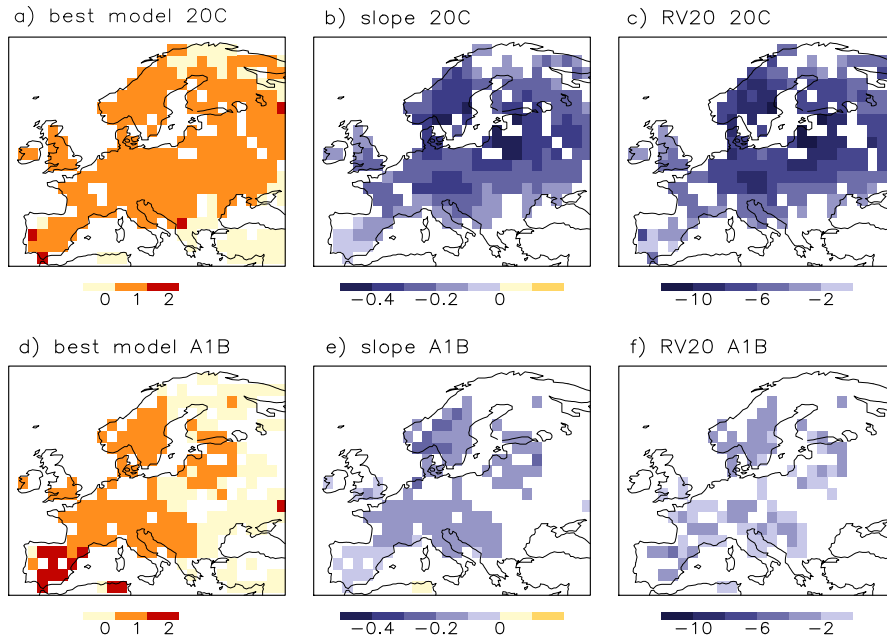At grid-points where model 2 is selected as best model (e.g., around the Gulf of

Figure 4.10—— Best model, slope of location parameter and the difference between RV20nonstat [°C] and RV20stat [°C] for the concatenated ensemble members of 20C (a-c) and A1B (d-f), respectively.

Venice in 20C1, cf. Fig. 4.7b), the RV20nonstat increases compared to RV20stat for maximum blocking frequency as depicted in figure 4.9b. This effect will be discussed in the following section 4.4.3.

To obtain a clearer picture of the changes between 20C and A1B, we concatenated the time slices (1961-2000 or 2160-2199) of the 3 ensemble members for each simulation, respectively. Thus, we receive a time series of 360 monthly DJF T2MIN to which the non-stationary GEV distribution is fitted. The resulting time series for A1B and 20C, respectively, include the variability of all three ensemble members considering the T2MIN and atmospheric blocking. This approach is justified since time trends within each time slice only play a minor role in explaining the variability in the underlying data.

Model 1 is selected as best for the concatenated ensemble members of 20C (20C-all hereinafter) in most of Europe, except in southeastern Europe and some grid points in northern Scandinavia as shown in figure 4.10a. The slope of the location parameter for model 1 in 20C-all (Fig. 4.10b) ranges from -0.02°C in southwestern Europe to -0.5°C around the Baltic Sea, indicating that atmospheric blocking has the strongest influence on central to eastern Europe and southern Scandinavia. Significant differences between RV20stat and RV20nonstat for the month with maximum blocking frequency (26.6%) within 20C-all (Fig. 4.10c) are also greatest in these areas reaching up to -10°C along the European Plain. It is important to note that the patterns for the best model and the slope depicted for 20C-all (Fig. 4.10a,
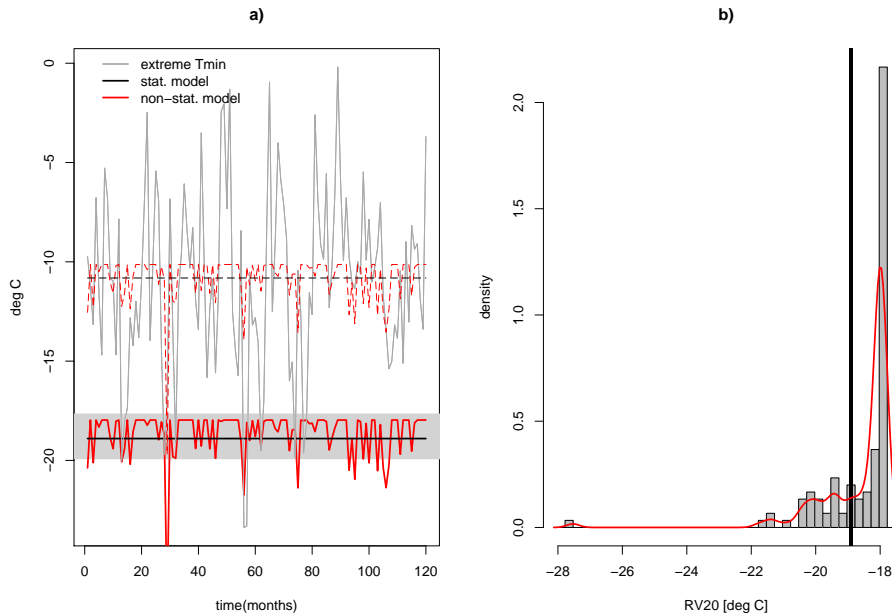
Figure 4.11— Grid-point at 9°E, 53°N (GP1): a) Median (dashed) and RV20 (solid) for the stationary (black) and non-stationary (red) GEV distribution fitted to the extreme T2MIN of 20C1 (grey line) for DJF months from 1961-2000. b) Histogram and density distribution (red line) of RV20 over time for the non-stationary GEV distribution in comparison to the stationary RV20 (solid black line).

b) correspond closely to the pattern found in ERA-40 (cf. Fig. 4.7d, h). The larger differences between RV20stat and RV20nonstat in 20C-all compared to ERA-40 (cf. Fig. 4.9d) result from the smaller blocking maximum in ERA-40 (12%).

For the concatenated A1B ensemble members (A1B-all hereinafter), model 1 is selected in a smaller area of Europe compared to 20C-all and ERA-40, ranging from the Balkans to southwestern Scandinavia (Fig. 4.10d). In eastern Europe mainly the stationary model was selected best, except in a small area along the European Plain. Model 2 is predominant on the Iberian Peninsula in A1B-all. The slope of the location parameter (Fig. 4.10e) is reduced compared to 20C-all with 0.27°C as maximum in southern Scandinavia. Also the significant differences between RV20stat and RV20nonstat (-1°C - -4°C) are reduced in A1B-all compared to 20C-all, which is mainly caused by the reduction of maximum blocking frequency to 16.3% in A1B-all and by the northwestward movement of the center of maximum blocking frequency (cf. Fig. 4.1c).

4.4.3 Grid-point examples

The results described in the previous sections have emphasized that including CAB into the GEV distribution improves the fit significantly in large parts of Europe. In this part we want to illustrate and explain the differences in RV20 between the
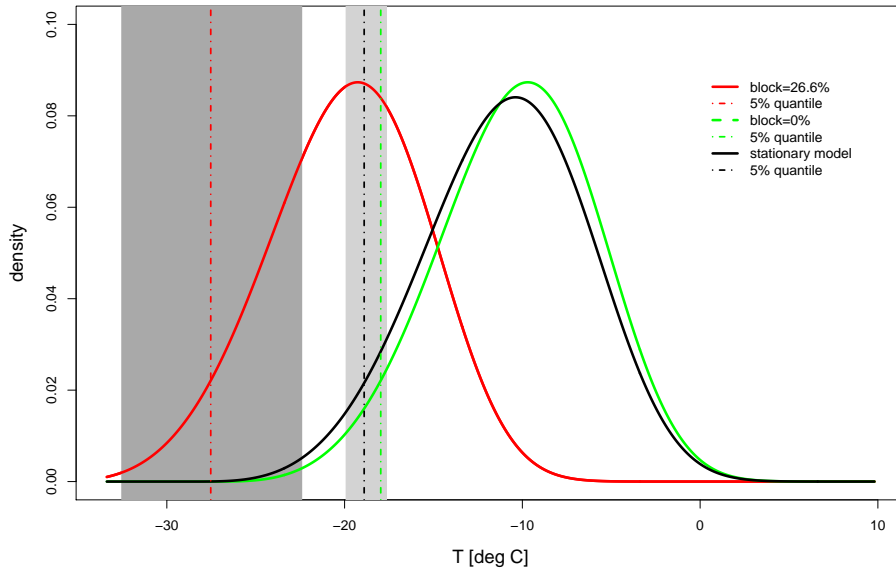
Figure 4.12— GEV distributions at GP1(20C1) for the stationary model (black) and the non-stationary model 1 for blocking frequencies of zero (green) and 26.6% (red) and the corresponding 5% quantiles (RV20, dashed lines) with their 90% confidence interval as grey shading.

stationary and non-stationary GEV distribution in more detail at two grid-points for one particular 20C ensemble member. We chose one grid-point (GP1 hereinafter) in central Europe (9°E, 53°N), where model 1 was selected as the best fitting model and another grid-point (GP2 hereinafter) in southern Europe (15°W, 46°N), where model 2 was best in the 20C1 ensemble member.

In fact, a stationary GEV distribution possesses stationary parameters and, consequently, stationary return values over time. On the contrary, non-stationary GEV distributions, where the parameters depend on a covariate, vary with the covariate (in our case atmospheric blocking) over time. This is also reflected in the return values. We illustrate this in figure 11a and 13a for GP1 and GP2, respectively. There we display the median (dashed) and the RV20 (solid) as black and red line for the stationary and non-stationary GEV distribution, respectively. The median is the 0.5 quantile of the GEV probability distribution and also stands for the 2-year return values. It is shown here for comparison with the underlying time series of extreme T2MIN (grey line) over 120 months (DJF) from 1961-2000, to which the GEV distributions were fitted.

We can see that the median and the RV20 for the stationary GEV distribution are generally lower than for the non-stationary distribution for very small (< 5%) or zero blocking frequencies within the 90% confidence interval as indicated by a grey band for the RV20stat in figure 4.11a. For those months where the blocking frequency is greater than 5%, RV20nonstat exceeds the 90% confidence interval and return values become significantly reduced compared to RV20stat.

The distribution of all RV20nonstat values is shown as histogram and overlaid
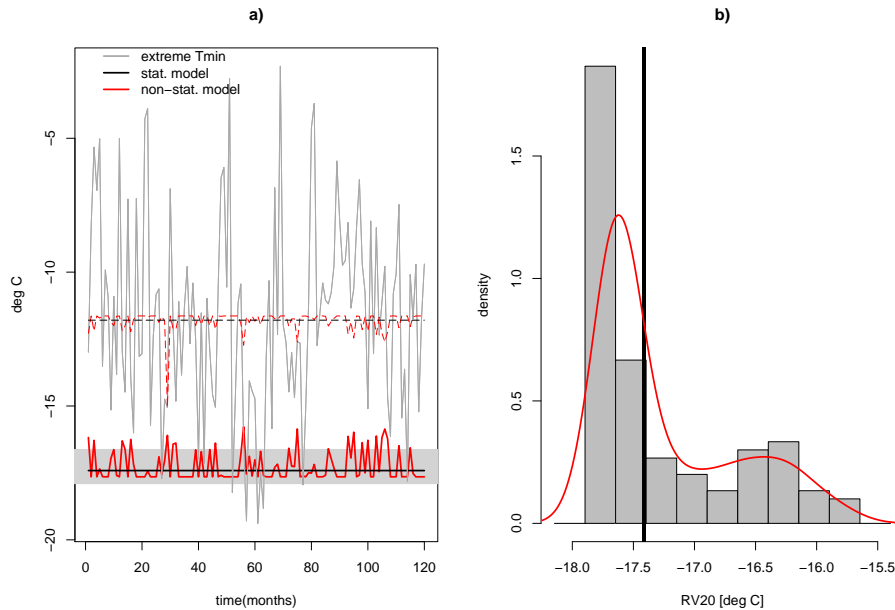
Figure 4.13— As figure 4.11, but for grid-point at 15°W, 46°N (GP2).

density distribution (red curve, Fig. 4.11b), ranging from 18.0°C to 27.6°C compared to RV20stat with a constant value at -18.9°C. Most RV20nonstat values are distributed around -18°C, because months with zero or small blocking frequencies occur much more often than months with a high blocking frequency.

Since for model 1 only the location parameter is dependent on CAB, the GEV distribution moves along the x-axis with changing blocking frequency as depicted in figure 4.12. For zero blocking frequency (green curve), the distribution is very close to the stationary GEV distribution, however not the same. With increasing blocking frequency the distribution curve moves to lower temperatures, as represented by the red curve for a maximum blocking frequency of 26.6% in 20C1.

Along with the mean change of the location of the GEV distributions for different blocking frequencies also their 5% quantile (dashed lines) changes, being equivalent to RV20. It can clearly be seen that the 90% confidence interval (light grey shading) of the RV20stat does not overlap with the RV20nonstat value (-27.6°C) for maximum blocking frequency, implying a significant change in RV20nonstat. In addition, also the 90% confidence interval of RV20nonstat (dark grey shading) for maximum blocking frequency does not overlap with the RV20stat confidence interval. Thus, for months with maximum blocking frequency, the RV20nonstat (red dashed line) is significantly reduced by -8.7°C or -9.6°C compared to the RV20stat (black) or RV20nonstat (green) for zero blocking frequency, respectively.

A different picture occurs when looking at GP2 (Fig. 4.13), where both the location and scale parameter are dependent on CAB, according to model 2. First, we can see that the median and the RV20 for the non-stationary GEV distribu-
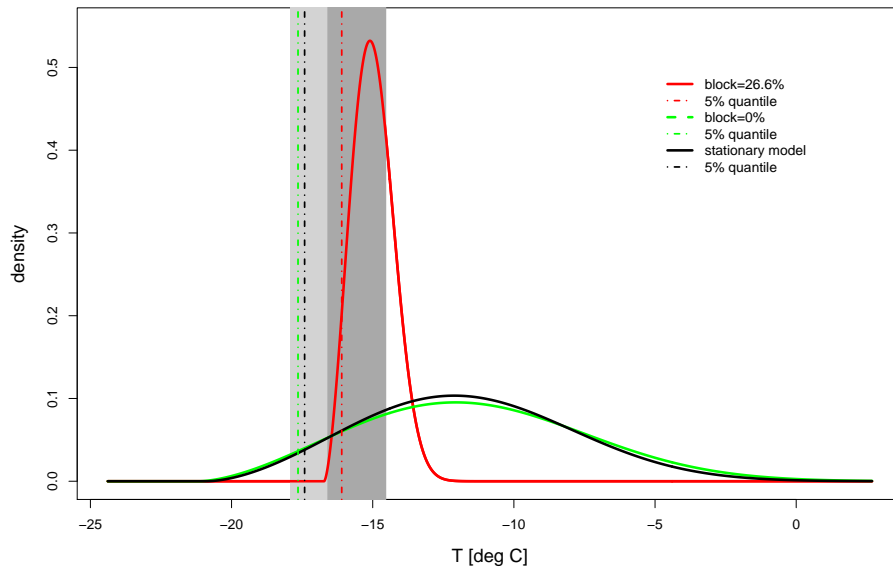
Figure 4.14— As figure 4.12, but for grid-point at 15°W, 46°N (GP2).

tion vary differently over time with changing blocking frequency. The median of
the non-stationary GEV distribution is remarkably reduced only in months with
very high blocking frequencies ($> 10\%$), while RV20nonstat for blocking frequen-
cies above 5% is significantly increased compared to the 90% confidence interval of
RV20stat. Values for RV20nonstat range from -17.6°C to -15.8°C, but most val-
ues for RV20nonstat are distributed around -17.6°C, which is slightly lower than
the constant value -17.4°C for RV20stat. On the contrary, for model 1 at GP1
(cf. Fig. 4.11a, b), RV20nonstat for zero and small blocking frequencies is higher
than RV20stat, and RV20nonstat values for high blocking frequencies are reduced
in comparison to RV20stat.

The dependence of the scale parameter on CAB seems to have a considerable
impact on the variability of the extreme T2MIN distribution. In figure 4.14, the
stationary GEV distribution (black) is very similar to that of the non-stationary
GEV distribution for zero blocking frequency (green), but with increasing block-
ing frequency the non-stationary GEV distribution shrinks, implying less variabil-
ity in the extreme T2MIN, as shown here for the maximum blocking frequency
in 20C1. This leads to the above-mentioned phenomenon that the median of the
non-stationary GEV distribution (cf. Fig. 4.13) decreases with increasing blocking
frequency, whereas the RV20nonstat (red dashed line) increases compared to the
RV20stat (black dashed line). This leads to an increase in RV20nonstat at grid
points where model 2 is selected as best (cf. section 4.4.2).

Figure 4.14 illustrates that RV20nonstat (-15.8°C) for maximum blocking fre-
quency lies outside of the 90% confidence interval of RV20stat (light grey shading).
However, the latter is overlapping with the 90% confidence interval of RV20nonstat
(dark grey shading, Fig. 4.14). Thus, even for maximum blocking frequency, a signif-
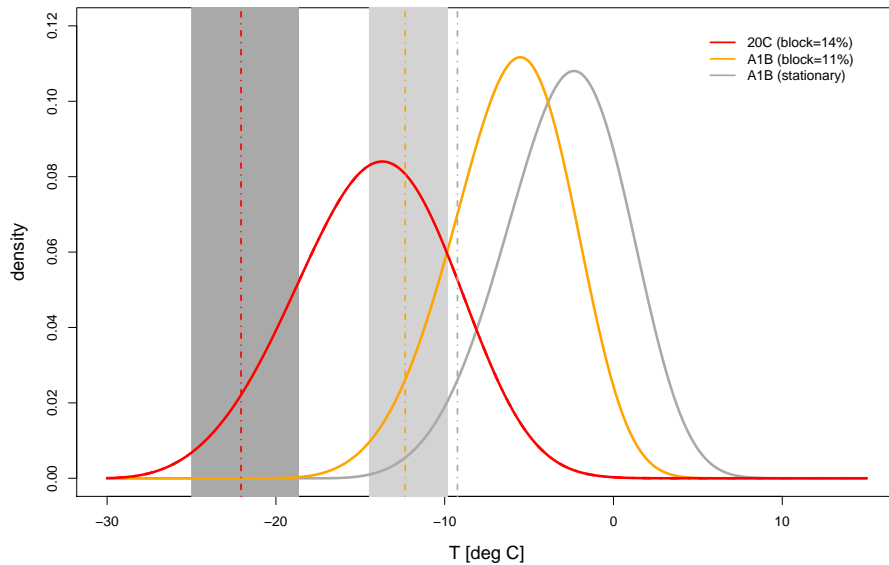
Figure 4.15—— GEV distributions at GP1 of the stationary model in A1B3 (grey) in comparison to the non-stationary model 1 for maximum blocking frequency in 20C2 (red) and in A1B3 (orange) and the corresponding 5% quantiles (RV20, dashed lines) with their 90% confidence interval as grey shading.

icant difference between RV20nonstat and RV20stat for model 2 cannot be detected. This finding supports our statement that atmospheric blocking has a considerable influence primarily on the location parameter of the GEV distribution of extreme T2MIN.

In A1B, the influence of atmospheric blocking on the location parameter of extreme T2MIN is similar to the findings for 20C, as can be seen exemplarily for GP1 in figure 4.15. The GEV distribution of the non-stationary model 1 (orange) for maximum blocking frequency (11%) in the ensemble member A1B3 is shifted to lower temperature values in comparison to the stationary model (grey). Consequently, also RV20nonstat (orange dashed line) is reduced to -12.3°C compared to -9.2°C for RV20stat. However, RV20nonstat of A1B is shifted to warmer temperatures in comparison to the RV20nonstat of 20C (red dashed line) for maximum blocking frequency (14%). This is consistent with the general warming trend in A1B (cf. Fig. 4.6). The difference between RV20nonstat in 20C (-22.1°C) and RV20nonstat in A1B (-12.3°C) is very large and can be considered as significant, since their 90% confidence intervals (grey shading) do not overlap (Fig. 4.15).

4.5 Summary and conclusion

In this study, we fit the GEV distribution to extreme winter minimum and maximum temperatures, respectively. We found that the GEV distribution is a good choice for representing extreme winter T2MIN in Europe, but fails to represent extreme winter

T2MAX. This is mainly due to the fact that extreme T2MAX occur in summer and block maxima taken from winter months do not represent real extreme values of T2MAX, thus cannot be correctly described by the GEV distribution.

In a comparison of the 20C ensemble simulations with ERA-40 re-analysis for the time period 1961 to 2000, we further showed that the model generally performs well with respect to the simulation of temperature extremes expressed by the parameters and return values of the stationary GEV distribution. In general, temperature extremes in Europe are Weibull distributed, which is in agreement with other studies (e.g., Kharin & Zwiers (2005); Parey (2008)). The model and ERA-40 reveal a distinct north-south gradient in the location and scale parameter with increasing (warmer) temperature extremes (indicated by the location parameter) and decreasing variability (indicated by the scale parameter) from north to south. In northeastern Europe, however, the model tends to simulate colder (on average 5°C lower) extreme T2MIN and higher variability than ERA-40. The difference in location parameter can be up to 9°C in northern Russia. Compared to ERA-40, the model overestimates winter sea level pressure in the Norwegian Sea and farther eastward (e.g., Van Ulden & van Oldenborgh (2006)), which leads to a weaker westerly flow and anomalous easterly winds in high northern latitudes. This misrepresentation of surface pressure patterns in the model results in anomalous cold winter temperature extremes in northeastern Europe. However, it has to be noted that, compared to observations, ERA-40 has a warm surface air temperature bias in winter at northern latitudes (Hagemann et al. (2005)). Thus, the model bias in T2MIN might not be as large as suggested from the comparison with ERA-40.

We also assessed differences between 20C and A1B scenario for the distribution parameters and RV20 of the stationary GEV distribution. For the extreme T2MIN, we identified significant differences in the location parameter and RV20 all over Europe. Both show similar patterns with a strong temperature increase in northeastern Europe (e.g. 14°C for location parameter) that decreases towards southwestern Europe (e.g. 3.5°C for location parameter). Goubanova & Li (2007) and Kharin & Zwiers (2000) have also identified this pattern for other models, giving further confidence to our results. In addition, we found a significant decrease in the scale parameter in parts of Europe, reaching from the British Isles and France to southeastern Europe. These results imply that future changes in extreme T2MIN in Europe are mainly governed by changes in the location parameter, which agrees with results of Kharin & Zwiers (2005). However in some regions, such as central Europe, changes in the scale parameter have to be considered as well.

Furthermore, we included a large-scale atmospheric circulation pattern, namely atmospheric blocking frequency, as covariate in the GEV distribution to improve the fit to extreme T2MIN. We set up a collection of models, where one or more parameters of the GEV distribution were linearly linked to the covariate atmospheric blocking.

In ERA-40 and in one 20C ensemble member we found that the fit of the GEV distribution can be significantly improved in large parts of Europe when the location

parameter is dependent on CAB. In the other two 20C ensemble members, the fit was improved by including CAB only in parts of central Europe. The differences between the ensemble members in the response to CAB reflect the natural variability at decadal and longer timescales. The spatial distribution of blocks as well as the length and the number of blocking events within the considered time slice vary between the ensemble members leading to different patterns in the response to the extreme T2MIN. Especially variations in blocking frequencies close to Europe (EB) between the ensemble members seem to play an important role for these differences. We tried to reduce the impact of the natural variability by concatenating the three ensemble members of 20C and A1B, respectively. The results for the concatenated 20C ensemble concerning the best model and the slope of the location parameter are very similar to ERA-40, thus giving confidence to our approach. Other reasons for the differences could be the length of time series considered for the analysis or systematic errors due to the short block length.

In those European regions, where linking the location to CAB improved the fit of the GEV distribution, we demonstrated a consistently decreasing slope of the location parameter for the 20C ensemble members and ERA-40. This implies a decrease in extreme T2MIN with increasing blocking frequency (up to -0.7°C per 1% blocking), meaning that we can expect colder nighttime temperatures for more persistent blocks within a month. RV20 is also significantly affected if the location parameter is dependent on CAB. Compared to the stationary GEV distribution it decreases with increasing blocking frequency. Especially for blocking frequencies above 5%, the RV20nonstat is significantly reduced with respect to RV20stat. Since we have calculated RV20nonstat for the month with maximum blocking frequency within the 20C and A1B time slice of each ensemble member, we receive the strongest response in the ensemble member with the highest blocking frequency (e.g. 27% in 20C1). This in turn corresponds with our statement mentioned above that we can expect even colder nighttime temperatures with increasing the blocking frequency.

We could only detect few scattered grid-points in 20C, where linking the scale parameter to CAB in addition to the location parameter, could further improve the fit. Thus, we conclude that a linear relation of the location parameter to atmospheric blocking frequency is sufficient to represent the variations in the underlying data. However, since atmospheric blocking explains only part of the variability of the European winter climate, the inclusion of other large-scale atmospheric circulation patterns (e.g. NAO (Scaife et al. (2008))) could probably further improve the fit of the GEV distribution to extreme T2MIN and explain more of the variation in the data.

The relationship between atmospheric blocking and extreme T2MIN remains robust also under future climate conditions. We still can expect colder extreme T2MIN when atmospheric blocking occurs in A1B. However, along with the general warming trend under anthropogenic climate change also the extreme T2MIN and their return values will increase, thus waiting times for a particular cold extreme event will be increased in a warmer climate. Due to the northwestward movement of Euro-Atlantic blocking and the reduced blocking frequency in A1B, as indicated

by several climate simulations (e.g., Sillmann & Croci-Maspoli (2008); Lupo et al. (1997); Bates & Meehl (1986)), an association between the location parameter and CAB is found over a smaller area in Europe. Furthermore, the cooling effect of atmospheric blocking on European winters will also diminish, because we can expect less blocking events in future climate.

We conclude that conditioning of the location parameter on atmospheric blocking improves the fit of the GEV distribution in present and future simulations. This enables us to statistically simulate colder extreme winter nighttime temperatures and to receive a distribution of possible return values. Since this relationship remains robust under future climate conditions, we can also use atmospheric blocking as predictor for extreme T2MIN in Europe in the context of statistical downscaling.

Chapter 5

Summary and Outlook

5.1 General summary

The objective of this dissertation was the assessment of extreme climate events in CGCM simulations of the present and future climate. Furthermore, associations between climate extremes and large-scale atmospheric circulation patterns were investigated to enable a better understanding of the mechanisms behind the occurrence of extreme climate events. In the beginning (section 1.5) several questions had been raised, which were answered throughout this study and will be summarized in the following:

Is the model able to realistically represent extreme climate events in the present climate?

Indices for extreme temperature and precipitation events were calculated from ECHAM5/MPI-OM data and compared with the Hadley Centre Observational Datasets (HadleyCentre (2006); Alexander et al. (2006)). This comparison revealed that the model is in general able to represent broad-scale patterns of the analyzed extreme indices under present climate conditions. However, the model bias can be substantial in certain regions. In a more detailed analysis of three European regions (northern, central, and southern Europe), distinct differences between the model and the observations could be found e.g., a cold bias in high northern latitudes and a dry bias in the Mediterranean region. These misrepresentations of extreme events in the model are mainly caused by shortcomings in the model simulation of large-scale atmospheric flow patterns in the respective regions. Furthermore, the coarse spatial resolution of the model can lead to biases in mountainous regions. The latter could be resolved by dynamical or statistical downscaling methods.

In addition, the GEV distribution of extreme winter temperatures in Europe was analyzed in respect to the distribution's parameters and 20-year return values for model and ERA-40 re-analysis data. This analysis supported the argument that the model is able to realistically simulate extreme temperature events, but also exhibited the aforementioned cold bias in northeastern Europe. This can partly be

explained by a positive surface pressure bias in the model northeast of the Norwegian Sea resulting in an anomalous northeasterly flow, which brings cold Arctic air into northeastern Europe.

What changes regarding extreme climate events can we expect under anthropogenic climate change in future climate model simulations? Are there regional and seasonal differences attached to these changes?

In the course of anthropogenic climate change, we can expect changes in extreme temperature and precipitation events as well. Depending on the chosen emission scenario (A1B or B1), the changes will be more or less pronounced. The increase in temperature extremes is found to be significant worldwide. Extreme precipitation events tend to significantly increase in regions that are already wet in present climate, and presently dry regions tend to dry out even more under future climate conditions.

A regional and seasonal assessment of extreme climate events is essential to analyze changes in extremes (e.g., Moberg & Coauthors (2006)). The study of three European regions could show distinct differences in the changes of extremes under future climate conditions (A1B scenario). In particular, the minimum temperature extremes rise faster than the maximum temperature extremes in northern latitudes. Furthermore, the minimum temperature extremes increase particularly in winter and early spring in central and northern Europe whereas the maximum temperature extremes increase predominately in summer in southern Europe together with a prolongation of dry spells in the Mediterranean region. An intensification of precipitation extremes is concentrated on central and northern Europe in winter and early spring, whereas precipitation extremes decrease throughout the year in southern Europe and particularly in summer in central Europe.

The patterns of changes determined in the future climate simulations are in general agreement with the observed changes in climate extremes of recent decades (e.g., Easterling et al. (1997); Moberg & Jones (2005); Alexander et al. (2006); Caesar et al. (2006)) and constitute a continuance of the observed trends. However, model biases as mentioned before can prejudice the quantitative assessment of future changes in extremes.

Can we find associations between large-scale atmospheric circulation patterns, in particular atmospheric blocking, and present and future climate extreme events? Do these associations change under anthropogenic climate change?

A composite analysis and studies by e.g., Rex (1950b, 1951) and Trigo et al. (2004), have indicated a physical coherence between the occurrence of Euro-Atlantic blocking events in winter and anomalous cold temperatures and less precipitation in central Europe. Based on that knowledge, statistical analyses were performed in this study to further investigate the association between atmospheric blocking (captured by a PV-based blocking indicator) and extreme temperature and precipitation events in the Euro-Atlantic region. In particular in winter, significant negative correlations

could be determined for the extreme minimum temperature in large parts of Europe, which denote colder nighttime temperatures during winter blocking events in present climate. Negative correlations with winter maximum temperature extremes and maximum 5-day precipitation amounts and blocking events also exist, but are less pronounced or not spatially coherent.

Under future climate conditions (A1B scenario), the correlation patterns remain robust, but become less in magnitude due to the decrease in blocking frequency in the analyzed A1B scenario. A reduction of winter blocking frequency was also found in future climate simulations of other studies (e.g., Bates & Meehl (1986); Lupo et al. (1997)) as well as in ERA-40 re-analysis data (Croci-Maspoli et al. (2007b)). Furthermore, the northwestward movement of blocking action and changes in the spatial extension of blocking frequency in the Euro-Atlantic domain results in a change of the spatial patterns of correlations over Europe.

The impact of blocking events onto European climate extremes seems to be very sensitive to the location of blocking occurrence. Long-lasting blocking events reaching Europe (e.g., between Iceland and the British Isles as well as around the North Sea) have a stronger influence on European climate extremes than blocking events restricted to the northwestern North Atlantic. According to a study by Croci-Maspoli et al. (2007a), the latter is the primary genesis and lysis region of blocking events during the negative NAO phase, whereas blocking events reveal a distinctive lysis region over Northern Europe during the positive phase of the NAO.

Recent studies have also pointed out associations between European temperature and precipitation extremes with the NAO index (e.g., Haylock & Goddess (2004); Santos & Corte-Real (2006); Santos et al. (2007); Scaife et al. (2008)). Changes in the predominant circulation regimes in Europe will thus have a considerable impact on the changes in extreme events. However, these considerations should be explored separately for different regions (e.g., southern, northern, western, and eastern Europe) since the influence of circulation regimes on the extremes may vary substantially over the regions (e.g., Bardin (2007)).

The full spatial and temporal description of the blocking phenomenon also with respect to other circulation regimes (e.g., NAO) and its influence on extreme events is facilitated by the use of the dynamical PV-based blocking indicator used in this study and motivates its preference compared to blocking indicators based on geopotential height.

Can we use the associations between large-scale atmospheric circulation patterns and climate extremes for the improvement of the statistical modeling of extreme values?

In this study, Euro-Atlantic atmospheric blocking events were linearly related to extreme winter minimum temperatures by including atmospheric blocking as covariate in the Generalized Extreme Value distribution. It is shown that especially linking the location parameter to atmospheric blocking could improve the fit of the GEV distribution to extreme minimum temperature data in present as well as in

future climate simulations. The spatial representation of these results varies among the ensemble members. However when taking into account the natural variability of all three ensemble members by concatenating them (20C and A1B, respectively) to one time series, a robust pattern could be obtained, which for the present climate is in agreement with the ERA-40 re-analysis. In the latter, the fit was improved in most areas of Europe (except the Iberian Peninsula). In A1B the area got reduced to western Europe due to the northwestward movement of blockings in the Euro-Atlantic domain.

In those areas where the fit for 20C and A1B could be improved by linking atmospheric blocking to the location parameter, a decreasing slope was determined. This particularly indicates decreasing nighttime temperatures with increasing blocking frequency. Including atmospheric blocking into the GEV distribution also has a considerable impact on the 20-year return values of minimum temperature extremes. In the presence of high blocking frequencies, the return values are significantly reduced in comparison to no blocking, which implies a reduced waiting time for a particular extreme nighttime temperature event. Without including atmospheric blocking into the GEV distribution, it was impossible to statistically model these very low nighttime temperature events.

In general, the relationship between the covariate atmospheric blocking and the extreme minimum temperature remains robust also in the A1B scenario, however, with less magnitude due to diminishing blocking frequencies compared to 20C. Consequently, also the cooling effect of atmospheric blocking events is reduced. In future climate, colder nighttime temperatures can still be expected during blocking events. However, along with the general warming trend under anthropogenic climate change, also the extreme minimum temperatures and their return values will be increased compared to present climate even when blocking occurs.

5.2   Conclusion and outlook

It has been shown in this study that the ECHAM5/MPI-OM is able to represent observed patterns of large-scale temperature and precipitation extremes, however with regional exceptions as, for example, the high northern latitudes and areas with complex orography. These findings are very important also for regional climate model (RCM) studies, which perform much better than a CGCM in areas with complex orography. However, the skill of a RCM to realistically represent climate extremes also strongly depends on the skill of the driving CGCM to represent the prognostic variables (e.g. wind, temperature, etc.), which serve as boundary conditions for the RCM. A misrepresentation of these variables would also be reflected in an erroneous simulation of extreme climate events simulated in both the CGCM and RCM. Thus, it is essential to improve the representation of large-scale atmospheric and oceanic flow patterns in CGCMs to be able to simulate extreme climate events correctly. On top of that also an increase in the spatial resolution of CGCMs could improve their representation of distinct regional and local features of extremes.

Furthermore, large-scale atmospheric circulation patterns are important for the understanding and interpretation of changes in extreme climate events. This study has shown that the inclusion of atmospheric blocking in the statistical modeling of extreme nighttime temperatures in European winter can explain more of the variability in the underlying data. Thus, Euro-Atlantic blocking could be used as predictor for extreme winter temperatures in the context of statistical downscaling.

Nevertheless, the statistical modeling can further be expanded and improved in various ways. For example, longer time series of temperature or precipitation data could be used, e.g. from a 500-year pre-industrial control simulation of the ECHAM5-MPI-OM model, to further test the statistical significance of the results presented in this study. Other circulation regimes derived by, e.g., EOF analysis (e.g., Pavan et al. (2000); Scherrer et al. (2006)) and also time trends could be included in the statistical models to be able to simulate more of the variability in the underlying data and to improve the estimates of return values. The statistical modeling can further be expanded to precipitation extremes or dry spells given a physical coherence between the considered circulation regime and the extreme event.

Besides the GEV distribution also the Generalized Pareto Distribution (GPD) can be applied to threshold models (c.f. section 1.3), which could further improve the results of the statistical modeling of extreme values. It would be a very interesting task to compare the results derived from fitting block maxima of extreme climate events to the GEV distribution with results from the threshold models fitted to the GPD.

Regarding the usage of atmospheric blocking as predictor for statistical downscaling, further testing and improvement of the methodology is also required. The method should be tested not only with ERA-40 re-analysis data but also with observational data sets. A comparison with re-analysis data is helpful when validating gridded CGCM data, but cannot represent the true story since ERA-40 contains model biases as well (e.g., Simmons et al. (2004); Hagemann et al. (2005); Uppala et al. (2005)).

A good representation of the entire blocking phenomenon in the model including its spatial and temporal characteristics forms an important basis for the usage of blocking events as predictor in the statistical downscaling of CGCM data. An improvement of the representation of blockings in models could be achieved by e.g., using a CGCM with higher resolved stratosphere. Stratospheric influences have already been discovered in respect to a more realistically representation of NAO in a CGCM by Scaife et al. (2005, 2008).

The PV-based blocking indicator used in this study has emerged to be a valuable tool for representing the dynamical features and the evolution of the blocking phenomenon. Thus, using this indicator can be helpful to investigate, which spatial dimension, geographical location, and time persistence of a blocking event is most prominent to the occurrence of extreme events in Europe.

PV is already used as operational forecast tool in studies of cyclone development (e.g., Mansfield (1996); Georgiev (1999)), because it has two major advantages.

First, PV is a conserved quantity of an air mass evolving under adiabatic conditions. Thus significant features that are related to synoptic scale weather systems can be identified and followed in space and time. Secondly, due to its invertibility one can obtain familiar meteorological fields (e.g., geopotential, wind, temperature and static stability), when the distribution of the PV and the boundary conditions (potential temperature at the surface) are known. Furthermore, with the help of the invertibility it is possible to quantify the importance of PV-anomalies and the strength of their associated circulation and temperature patterns. Thus, due to the fact that the blocking indicator is based on the potential vorticity and not geopotential height, important prediction skills are attached to it. For example, the evolution of a blocking event could be predicted to a certain extent (which has yet to be investigated) and consequently also its impact on European climate or weather.

Appendix A

Software

The correlation analysis as well as the statistical modeling of extreme events have been performed with the statistical software R. R is available as free software under the terms of the Free Software Foundation's GNU General Public License and can be obtained at *http://www.r-project.org/*.

For the extreme value analysis the packages ***ismev*** from Stuart Coles and Alec Stephenson and ***evd*** also from Alec Stephenson have been applied in my statistical programs. Furthermore the package ***fdrtool*** from Korbinian Strimmer has been used to calculate the false discovery rate in my correlation analyses. All packages can be obtained via *http://www.r-project.org/*.

Bibliography

ALEXANDER, L., ZHANG, X., PETERSON, T., CAESAR, J., GLEASON, B., KLEIN TANK, A., HAYLOCK, M., COLLINS, D., TERWIN, B., RAHIMZADEH, F., TAGIPOUR, A., AMBENJE, P., RUPA KUMAR, K., REVADEKAR, J., GRIFFITHS, G., VINCENT, L., STEPHENSON, D., BURN, J., AGUILAR, E., BRUNET, M., TAYLOR, M., NEW, M., ZHAI, P., RUSTICUCCI, M., AND VAZQUEZ-AQUIRRE, J. (2006). Global observed changes in daily climate extremes of temperature and precipitation. *Journal of Geophysical Research* **111**, D05109.

BARDIN, M. Y. (2007). Quasi-stationary circulation and its effect on air temperature anomalies and extremes over western Russia. *Russian Meteorology and Hydrology* **32**, 75–84.

BATES, G. AND MEEHL, G. A. (1986). The effect of CO_2 concentration on the frequency of blocking in a general circulation model coupled to a simple mixed layer ocean. *Monthly Weather Review* **114**, 687–701.

BENGTSSON, L., HODGES, K., AND ROECKNER, E. (2006). Storm tracks and climate change. *Journal of Climate* **19**, 3518–3543.

BENISTON, M., REBETEZ, M., GIORGI, F., AND MARINUCCI, M. R. (1994). An analysis of regional climate change in Switzerland. *Theoretical and Applied Climatology* **49**, 135–159.

BENISTON, M. AND STEPHENSON, D. B. (2004). Extreme climatic events and their evolution under changing climatic conditions. *Global and Planetary Change* **44**, 1–9.

BENISTON, M., STEPHENSON, D. B., CHRISTENSEN, O. B., FERRO, C. A. T., FREI, C., GOYETTE, S., HALSNAES, K., HOLT, T., JYLH, K., KOFFI, B., PALUTIKOF, J., SCHLL, R., SEMMLER, T., AND WOTH, K. (2007). Future extreme events in European climate: An exploration of regional climate model projections. *Climatic Change* **81**, 71–95.

BEST, D. J. AND ROBERTS, D. E. (1975). Algorithm AS89: The upper tail probabilities of Spearman's rho. *Applied Statistics* **24**, 377–379.

BURNHAM, K. P. AND ANDERSON, D. R. (2003). *Model Selection and Multimodel Inference: A Practical-Theoretic Approach*. 2nd Edition. Springer-Verlag, New York, NY, USA, 488pp.

CAESAR, J., ALEXANDER, L., AND VOSE, R. (2006). Large-scale changes in observed daily maximum and minimum temperatures: Creation and analysis of a new gridded data set. *Journal of Geophysical Research* **111**, D05101.

CASSOU, C., TERRAY, L., HURRELL, J. W., AND DESER, C. (2004). North Atlantic winter climate regimes: Spatial asymmetry, stationarity with time, and ocean forcing. *Journal of Climate* **17**, 1055–1068.

CASSOU, C., TERRAY, L., AND PHILLIPS, A. (2005). Tropical Atlantic influence on European heat waves. *Journal of Climate* **18**, 2805–2811.

CHAVEZ-DEMOULIN, V. AND DAVISON, A. C. (2005). Generalized additive modelling of sample extremes. *Applied Statistics* **54**, 207–222.

CHRISTENSEN, J. AND CHRISTENSEN, O. B. (2003). Climate modelling: Severe summertime flooding in Europe. *Nature* **421**, 805–806.

COLES, S. (2001). *An Introduction to statistical modeling of extreme values*. 1st Edition. Springer Verlag, London, Department of Mathematics, University of Bristol, Bristol, BS8 1TW, UK.

COLES, S. G. AND DIXON, M. J. (1999). Likelihood-based inference for extreme value models. *Extremes* **2**, 5–23.

CORTI, S., MOLTENI, F., AND PALMER, T. (1999). Signature of recent climate change in frequencies of natural atmospheric circulation regimes. *Letters to Nature* **398**, 799–802.

CROCI-MASPOLI, M. (2005). Atmospheric blocking: Patterns and trends over the last 44 years. Presentation at the scientific assembly of the International Association of Meteorology and Atmospheric Sciences (IAMAS), Beijing, China.

CROCI-MASPOLI, M., SCHWIERZ, C., AND DAVIES, H. C. (2007a). Atmospheric blocking: space-time links to the NAO and PNA. *Climate Dynamics* **29**, 713–725.

CROCI-MASPOLI, M., SCHWIERZ, C., AND DAVIES, H. C. (2007b). A multifaced climatology of atmospheric blocking and its recent linear trend. *Journal of Climate* **20**, 633–649.

D'ANDREA, F., TIBALDI, S., BLACKBURN, M., BOER, G., DEQUE, M., DIX, M. R., DUGAS, B., FERRANTI, L., IWASAKI, T., KITOH, A., POPE, V., RANDALL, D., ROECKNER, E., STRAUS, D., STERN, W., VAN DEN DOOL, H., AND WILLIAMSON, D. (1998). Northern hemisphere atmospheric blocking as simulated by 15 atmospheric general cirulation models in the period 1979-1988. *Climate Dynamics* **14**, 385–407.

Davison, A. C. and Smith, R. L. (1990). Models for exceedances over high thresholds. *Journal of the Royal Statistical Society* **B 52**, 393–442.

Doblas-Reyes, F. J., Casado, M. J., and Pastor, M. A. (2002). Sensitivity of the northern hemisphere blocking frequency to the detection index. *Journal of Geophysical Research* **107**, D2.

Dole, R. M. and Gordon, N. D. (1983). Persistent anomalies of the extratropical northern hemisphere wintertime circulation: Geographical distribution and regional persistence characteristics. *Monthly Weather Review* **111**, 1567–1586.

Easterling, D. R., Horton, B., Jones, P. D., Peterson, T. C., Karl, T. R., Parker, D. E., Salinger, M. J., Razuvayev, V., Plummer, N., Jamason, P., and Folland, C. K. (1997). Maximum and minimum temperature trends for the globe. *Science* **277**, 364–367.

El Adlouni, S., Ouarda, T. B. M. J., Zhang, X., Roy, R., and Bobee, B. (2007). Generalized maximum likelihood estimators for the non-stationary generalized extreme value model. *Water Resources Research* **43**, W03410.

Elliott, R. D. and Smith, T. B. (1949). A study of the effects of large blocking highs on the general circulation of the northern hemisphere westerlies. *Journal of Meteorology* **6**, 67–85.

Fisher, R. A. and Tippett, L. H. C. (1928). Limiting forms of the frequency distributions of the largest or smalest number of a sample. *Proceedings of the Cambridge Philosophical Society* **24**, 180–190.

Folland, C. K., Miller, C., Bader, D., Crowe, M., Jones, P., Plummer, N., Richman, M., Parker, D. E., Rogers, J., and Scholefield, P. (1999). Workshop on indices and indicators for climate extremes, Asheville, NC, USA, 3-6 June 1997 Breakout Group C: Temperature indices for climate extremes. *Climatic Change* **42**, 31–43.

Frei, C. (2003). Statistical limitations for diagnosing changes in extremes from climate model simulations. *AMS annual meeting* **14**, 1–6. 14th Symposium on Global Change and Climate Variations.

Frich, P., Alexander, L., Della-Marta, P., Gleason, B., Haylock, M., Klein Tank, A., and Peterson, T. (2002). Observed coherent changes in climate extremes during the second half of the twentieth century. *Climate Research* **19**, 193–212.

Friederichs, P. and Hense, A. (2007). Statistical downscaling of extreme precipitation events using censored quantile regression. *Monthly Weather Review* **135**, 2365–2378.

GAETAN, C. AND GRIGOLETTO, M. (2007). A hierarchical model for the analysis of spatial rainfall extremes. *Journal of Agricultural, Biological, and Environmental Statistics* **12**, 434–449.

GEORGIEV, C. (1999). Quantitative relationship between meteosat WV data and positive potential vorticity anomalies: a case study over the Mediterranean. *Meteorological Applications* **6**, 97–109.

GIORGI, F., WHETTON, P. H., JONES, R. G., CHRISTENSEN, J. H., MEARNS, L. O., HEWITSON, B., VONSTORCH, H., FRANCISCO, R., AND JACK, C. (2001). Emerging patterns of simulated regional climatic changes for the 21st century due to anthropogenic forcings. *Geophysical Research Letters* **28**, 3317–3320.

GNEDENKO, B. V. (1943). Sur la distribution limite du terme maximum d'une serie aletoire. *Annals of Mathematics* **44**, 423–453.

GOUBANOVA, K. AND LI, L. (2007). Extremes in temperature and precipitation around the Mediterranean basin in an ensemble of future scenario simulations. *Global and Planetary Change* **57**, 27–42.

GRASA, A. A. (1989). *Econometric Model Selection: A new approach*. Kluwer Academic Publishing, New York, 260pp.

GUMBEL, E. J. (1958). *Statistics of Extremes*. Columbia University Press, New York, NY, USA. 375pp.

HADLEYCENTRE (2006). *Hadley Centre Observational Datasets*. Met Office, Hadley Center for Climate Prediction and Research, http://www.hadobs.org, Devon, UK.

HAGEMANN, S., ARPE, K., AND BENGTSSON, L. (2005). *Validation of the hydrological cycle of ERA-40*. Reports on Earth System Science 10, Max Planck Institute for Meteorology, Bundesstr. 53, Hamburg, Germany.

HAGEMANN, S., ARPE, K., AND ROECKNER, E. (2006). Evaluation of the hydrological cycle in the ECHAM5 model. *Journal of Climate* **19**, 3810–3827.

HAYLOCK, M. AND GODDESS, C. (2004). Interannual variability of European extreme winter rainfall and links with mean large-scale circulation. *International Journal of Climatology* **24**, 759–776.

HOSKING, J. R. M. (1990). L-moments: analysis and estimation of distributions using linear combinations of order statistics. *Journal of the Royal Statistical Society B* **52**, 105–124.

IPCC (2001). *Climate Change 2001: The Scientific Basis*. Intergovernmental Panel on Climate Change. Cambridge University Press, Cambridge, England.

IPCC (2007). *Climate Change 2007: The Physical Science Basis. Contribution of Working Group I to the Fourth Assessment Report of the Intergovernmental Panel on Climate Change*. Solomon, S., Qin, D., Manning, M., Chen, Z., Marquis, M., Averyt, K. B., Tignor, M., and Miller, H. L. Eds. Cambridge University Press, Cambridge, UK and New York, NY USA, 996pp.

Jungclaus, J. H., Botzet, M., Haak, H., Keenlyside, N., Luo, J.-J., Latif, M., Marotzke, J., Mikolajewicz, U., and Roeckner, E. (2006). Ocean circulation and tropical variability in the coupled model ECHAM5/MPI-OM. *Journal of Climate* **19**, 3952–3972.

Kallache, M., Rust, H. W., Lange, H., and Kropp, J. P. (2007). *Extreme value analysis considering trends*. in: In Extremis: Extremes, trends and correlations in hydrology and climate. Springer, Berlin, (forthcoming).

Karl, T., Jones, P., R.W., K., Kukla, G., Plummer, N., Razuvayev, V., Gallo, K., Lindseay, J., Charlson, R., and Peterson, T. (1993). A new perspective on recent global warming: Asymmetric trends of daily maximum and minimum temperature. *Bulletin of the American Meteorological Society* **74**, 1007–1023.

Karl, T. R., Nicholls, N., and Ghazi, A. (1999). CLIVAR/GCOS/WMO workshop on indices and indicators for climate extremes workshop summary. *Climatic Change* **42**, 3–7.

Katz, R., Brush, G., and Parlange, M. (2005). Statistic of extremes: Modeling ecological disturbances. *Ecology* **86**, 1124–1134.

Katz, R., Parlange, M., and Naveau, P. (2002). Statistics of extremes in hydrology. *Advances in Water Resources* **25**, 1287–1304.

Katz, R. W. and Brown, B. G. (1992). Extreme events in a changing climate: variability is more important than averages. *Climatic Change* **21**, 289–302.

Kharin, V. and Zwiers, F. (2005). Estimating extremes in transient climate change simulations. *Journal of Climate* **18**, 1156–1173.

Kharin, V. V. and Zwiers, F. W. (2000). Changes in the extremes in an ensemble of transient climate simulations with a coupled atmosphere-ocean GCM. *Journal of Climate* **13**, 3760–3788.

Kiktev, D., Sexton, D. M. H., Alexander, L., and Folland, C. K. (2003). Comparison of modeled and observed trends in indices of daily climate extremes. *Journal of Climate* **16**, 3560–3571.

Klein Tank, A. and Koennen, G. (2003). Trends in indices of daily temperature and precipitation extremes in Europe, 1946-99. *Journal of Climate* **16**, 3665–3680.

LEADBETTER, M. R., LINDGREN, G., AND ROOTZN, H. (1983). *Extremes and related properties of random sequences and processes*. Springer Verlag, New York, NY, USA. 336pp.

LECKEBUSCH, G. C., KOFFI, B., ULBRICH, U., PINTO, J. G., SPANGEHL, T., AND ZACHARIAS, S. (2006). Analysis of frequency and intensity of European winter storm events from a multi-model perspective, at synoptic and regional scales. *Climate Research* **31**, 59–74.

LEJENAES, H. AND OKLAND, H. (1983). Characteristics of northern hemisphere blocking as determined from a long time series of observational data. *Tellus* **35A**, 350–362.

LUPO, A. R., OGLESBY, R. J., AND MOKHOV, I. I. (1997). Climatological features of blocking anticyclones: a study of northern hemisphere CCM1 model blocking events in present-day and double CO_2 concentration atmospheres. *Climate Dynamics* **13**, 181–195.

LUPO, A. R. AND SMITH, P. J. (1995). Climatological features of blocking anticyclones in the northern hemisphere. *Tellus* **47**, 439–456.

MANSFIELD, D. A. (1996). The use of potential vorticity as an operational forecast tool. *Meteorological Applications* **3**, 195–210.

MARSLAND, J. S., HAAK, H., JUNCLAUS, J. H., LATIF, M., AND ROESKE, F. (2003). The Max Planck Institute global ocean/sea ice model with orthogonal curvilinear coordinates. *Ocean Model* **5**, 91–127.

MCGREGOR, G. R., FERRO, C. A. T., AND STEPHENSON, D. B. (2005). *Projected changes in extreme weather and climate events in Europe*. KIRCH, W., MENNE, B., AND BERTOLLINI, R. Eds., vol. 13-23 of *Extreme weather and climate events and public health responses*. Springer, Berlin Heidelberg New York, Dresden.

MEARNS, L. O., KATZ, R. W., AND SCHNEIDER, S. H. (1984). Extreme high-temperature events: Changes in their probabilities with changes in mean temperature. *Journal of Applied Meteorology* **23**, 1601–1613.

MEEHL, G., ZWIERS, F., EVANS, J., KNUTSON, T., MEARNS, L., AND WHETTON, P. (2000). Trends in extreme weather and climate events: Issues related to modeling extremes in projections of future climate change. *Bulletin of the American Meteorological Society* **81**, 427–436.

MEEHL, G. A. AND TEBALDI, C. (2004). More intense, more frequent, and longer lasting heat waves in the 21st century. *Science* **305**, 994–997.

MOBERG, A. AND COAUTHORS (2006). Indices for daily temperature and precipitation extremes in Europe analyzed for the period 1901-2000. *Journal of Geophysical Research* **111**, D22106.

MOBERG, A. AND JONES, P. D. (2005). Trends in indices for extremes in daily temperature and precipitation in central and western Europe, 1901-99. *International Journal of Climatology* **25**, 1149–1171.

MUNICHRE (2002). *An Annual Review of Natural Catastrophes*. Topics. Munich Re-insurance Company Publications, 49 pp.

NADARAJAH, S. (2005). Extremes of daily rainfall in West Central Florida. *Climatic Change* **69**, 325–342.

NAKICENOVIC, N. AND SWART, R. (2000). *Special Report on Emission Scenarios*. NAKICENOVIC, N. AND SWART, R. Eds. Cambridge University Press, Cambridge, UK, ISBN 0521804930, 612pp.

NICHOLLS, N. AND MURRAY, W. (1999). Workshop on indices and indicators for climate extremes: Asheville, NC, USA, 3-6 June 1997 Breakout Group B: Precipitation. *Climatic Change* **42**, 23–29.

NOGAJ, M., PAREY, S., AND DACUNHA-CASTELLE, D. (2007). Non-stationary extreme models and a climatic application. *Nonlinear Processes in Geophysics* **14**, 305–316.

NOGAJ, M., YIOU, P., PAREY, S., MALEK, F., AND P. NAVEAU, P. (2006). Amplitude and frequency of temperature extremes over the North Atlantic region. *Geophysical Research Letters* **33**, L10801.

PALUTIKOF, J. P., BRABSON, B. B., LISTER, D. H., AND ADCOCK, S. T. (1999). A review of methods to calculate extreme wind speeds. *Meteorological Applications* **6**, 119–132.

PAREY, S. (2008). Extremely high temperatures in France at the end of the century. *Climate Dynamics* **30**, 99–112.

PARMESAN, C., ROOT, T. L., AND WILLIG, M. R. (2000). Impacts of extreme weather and climate on terrestrial biota. *Bulletin of the American Meteorological Society* **81**, 443?450.

PAVAN, V., MOLTENI, F., AND BRANKOVIC, C. (2000). Wintertime variability in the Euro-Atlantic region in observations and in ECMWF seasonal ensemble experiments. *Quarterly Journal of the Royal Meteorological Society* **126**, 2143–2173.

PELLY, J. L. AND HOSKINS, B. J. (2003a). How well does the ECMWF ensemble prediction system predict blocking? *Quarterly Journal of the Royal Meteorological Society* **129**, 1683–1702.

PELLY, J. L. AND HOSKINS, B. J. (2003b). A new perspective on blocking. *Journal of Atmospheric Sciences* **60**, 743–755.

PETERSON, T. C. (2005). Climate change indices. *WMO Bulletin* **54**, 83–86.

REX, D. F. (1950a). Blocking action in the middle troposphere and its effects upon regional climate, I: An aerological study of blocking. *Tellus* **2**, 196–211.

REX, D. F. (1950b). Blocking action in the middle troposphere and its effects upon regional climate, II: The climatology of blocking action. *Tellus* **2**, 275–301.

REX, D. F. (1951). The effect of Atlantic blocking action upon European climate. *Tellus A* **3**, 1–16.

ROECKNER, E., BAEUML, G., BONVENTURA, L., BROKOPF, R., ESCH, M., GIORGETTA, M., HAGEMANN, S., KIRCHNER, I., KORNBLUEH, L., MANSZINI, E., RHODIN, A., SCHLESE, U., SCHULZWEIDA, U., AND TOMPKINS, A. (2003). *The atmospheric general circulation model ECHAM5. Part 1: Model description*. MPI Report 349, Max Planck Institute for Meteorology.

ROECKNER, E., BRASSEUR, G., GIORGETTA, M., JACOB, D., JUNGCLAUS, J., REICK, C., AND SILLMANN, J. (2006a). Climate projections of the 21st century. MPI Brochure, MPI for Meteorology, Hamburg, Germany, available from http://www.mpimet.mpg.de/fileadmin/grafik/presse/ClimateProjections2006.pdf.

ROECKNER, E., BROKOPF, R., ESCH, M., GIORGETTA, M., HAGEMANN, S., KORNBLUEH, L., MANZINI, E., SCHLESE, U., AND SCHULZWEIDA, U. (2006b). Sensitivity of simulated climate to horizontal and vertical resolution in the ECHAM5 atmosphere model. *Journal of Climate* **19**, 3771–3791.

ROECKNER, E., STIER, P., FEICHTER, J., KLOSTER, S., ESCH, M., AND FISCHER-BRUNS, I. (2006c). Impact of carbonaceous aerosol emissions on regional climate change. *Cimate Dynamics* **27**, 553–571.

SANTOS, J. A. AND CORTE-REAL, J. (2006). Temperature extremes in Europe and wintertime large-scale atmospheric circulation: HadCM3 future scenarios. *Climate Research* **31**, 3–18.

SANTOS, J. A., CORTE-REAL, J., ULBRICH, U., AND PALUTIKOF, J. (2007). European winter precipitation extremes and large-scale circulation: a coupled model and its sceanrios. *Theoretical and Applied Climatology* **87**, 85–102.

SAUSEN, R., KOENIG, W., AND SIELMANN, F. (1995). Analysis of blocking events from observations and ECHAM model simulations. *Tellus* **47A**, 421–483.

SCAIFE, A., FOLLAND, C. K., ALEXANDER, L., MOBERG, A., AND KNIGHT, J. R. (2008). European climate extremes and the North Atlantic Oscillation. *Journal of Climate* **21**, 72–83.

SCAIFE, A. A., KNIGHT, J. R., VALLIS, G., AND FOLLAND, C. K. (2005). A stratospheric influence on the winter NAO and North Atlantic surface climate. *Geophysical Research Letters* **32**, L18715.

SCHERRER, S. C., CROCI-MASPOLI, M., SCHWIERZ, C., AND APPENZELLER, C. (2006). Two-dimensional indices of atmospheric blocking and their statistical relationship with winter climate patterns in the Euro-Atlantic region. *International Journal of Climatology* **26**, 233–249.

SCHWIERZ, C., CROCI-MASPOLI, M., AND DAVIES, H. (2004). Perspicacious indicators of atmospheric blocking. *Geophysical Research Letters* **31**, L06125.

SHABBAR, A., HUANG, J., AND HIGUCHI, K. (2001). The relationship between the wintertime North Atlantic Oscillation and blocking episodes in the North Atlantic. *International Journal of Climatology* **21**, 355–369.

SHUKLA, J. AND MO, K. C. (1983). Seasonal and geographical variation of blocking. *Monthly Weather Review* **111**, 388–404.

SILLMANN, J. AND CROCI-MASPOLI, M. (2008). Euro-Atlantic blocking and extreme events in present and future climate simulations. *Geophysical Research Letters* Submitted.

SILLMANN, J. AND ROECKNER, E. (2008). Indices for extreme climate events in projections of anthropogenic climate change. *Climatic Change* **86**, 83–104.

SIMMONS, A. J., JONES, P. D., DA COSTA BECHTOLD, V., BELJAARS, A. C. M., KÅLLBERG, P. W., SAARINEN, S., UPPALA, S. M., VITERBO, P., AND WEDI, N. (2004). *Comparison of trends and variability in CRU, ERA-40 and NCEP/NCAR re-analyses of monthly-mean surface air temperature*. ERA-40 Project Report Series 18, ECMWF, Reading, UK.

STEPHENS, M. A. (1970). Use of Kolmogorov-Smirnov, Cramer-von-Mises and related statistics without extensive tables. *Journal of the Royal Statistical Society* **32B**, 115–122.

TEBALDI, C., HAYHOE, K., ARBLASTER, J., AND MEEHL, G. (2006). Going to extremes. An intercomparison of model-simulated historical and future changes in extreme events. *Climatic Change* **79**, 185–211.

TERRAY, L., DEMORY, M.-E., DEQUE, M., DE COETLOGON, G., AND MAISONNAVE, E. (2004). Simulation of late-twenty-first-century changes in wintertime atmospheric circulation over Europe due to anthropogenic causes. *Journal of Climate* **17**, 4630–4635.

TIBALDI, S. AND MOLTENI, F. (1990). On the operational predictability of blocking. *Tellus* **42A**, 343–365.

TRIGO, R., I. TRIOGO, C. D. C., AND OSBORN, T. J. (2004). Climate impact of the European winter blocking episodes from the NCEP/NCAR Re-analysis. *Climate Dynamics* **23**, 17–28.

TYRLIS, E. AND HOSKINS, B. J. (2008). Aspects of a northern hemisphere atmospheric blocking climatology. *Journal of Atmospheric Sciences* **65**, 1638–1652.

UPPALA, S. M., KÅLLBERG, P. W., SIMMONS, A. J., ANDRAE, U., DA COSTA BECHTOLD, V., FIORINO, M., GIBBSON, J. K., HASELER, J., HERMANDEZ, A., KELLY, G. A., AND LI, X. (2005). The ERA-40 Re-analysis. *Quarterly Journal of the Royal Meteorological Society* **131**, 2961–3012.

VAN ULDEN, A. P. AND VAN OLDENBORGH, G. J. (2006). Large-scale atmospheric circulation biases and changes in global climate model simulations and their importance for climate change in central Europe. *Atmospheric Chemistry and Physics* **6**, 863–881.

WANG, X. L., ZWIERS, F. W., AND SWAIL, V. R. (2004). North Atlantic Ocean wave climate change scenarios for the twenty-first century. *Journal of Climate* **17**, 2368–2383.

WILBY, R., WIGLEY, T., CONWAY, D., JONES, P., HEWITSON, B., MAIN, J., AND WILKS, D. (1998). Statistical downscaling of general circulation model output: A comparsion of methods. *Water Resources Research* **34**, 2995–3008.

WILKS, D. S. (2006). On "field significance" and the false discovery rate. *Journal of Applied Meteorology and Climatology* **45**, 1181–1189.

WOTH, K., WEISSE, R., AND VON STORCH, H. (2006). Climate change and North Sea storm surge extremes: an ensemble study of storm surge extremes expected in a changed climate projected by four different regional climate models. *Ocean Dynamics* **56**, 3–15.

YIOU, P. AND NOGAJ, M. (2004). Extreme climatic events and weather regimes over the North Atlantic: When and where? *Geophysical Research Letters* **31**, L07202.

YIOU, P., VAUTARD, R., NAVEAU, P., AND CASSOU, C. (2007). Inconsistency between atmospheric dynamics and temperatures during the exceptional 2006/2007 fall/winter and recent warming in Europe **34**, L21808.

ZHANG, X., HEGERL, G., ZWIERS, F., AND KENYON, J. (2005). Avoiding inhomogeneity in percentile-based indices of temperature extremes. *Journal of Climate* **18**, 1641–1651.

ZWIERS, F. AND KHARIN, V. (1998). Changes in the extremes of the climate simulated by CCC GCM2 under CO_2 doubling. *Journal of Climate* **11**, 2200–2222.

List of Acronyms

20C	20th century simulations (3 ensemble members)
20C-all	concatenated 20C ensemble members
A1B	A1B scenario simulations (3 ensemble members)
A1B-all	concatenated A1B ensemble members
AIC	Akaike information criterion
AOGCM	Atmosphere-Ocean General Circulation Model
BIC	Bayesian information criterion
CAB	Covariate atmospheric blocking
CCI	Commision of Climatology
CGCM	Coupled General Circulation Model
CLIVAR	Climate Variability and Predictability project
CON	Control run
COV	Covariate
d.f.	degrees of freedom
DEV	Deviance statistic
DJF	climatological winter (December, January, February)
EB	European Blockings (15°W-30°E, 50°N-70°N)
ERA-40	ERA-40 re-analysis
ETCCDMI	Expert Team on Climate Change Detection Monitoring and Indices
FclimDex	computer software to calculate indices for extremes in FORTRAN
FDR	False Discovery Rate
GCM	General Circulation Model
GEV	Generalized Extreme Value
GHG	Greenhouse gases
GP1	grid point at 9°E, 53°N (central Europe)
GP2	grid point at 15°W, 46°N (southern Europe)
GPD	Generalized Pareto Distribution

HadEX	indices for extreme events based on the Hadley Centre observational datasets
HIC	Hannan-Quinn information criterion
iid	independent and identical distributed
IPCC (AR4)	Intergovernmental Panel on Climate Change (Fourth Assessment Report)
JJA	climatological summer (June, July, August)
KS	Kolmogorov-Smirnov
ML	Maximum Likelihood
NAO	North Atlantic Oscillation
nllh	negative log-likelihood
POT	Peaks over Threshold
PREC	daily precipitation
PV	Potentail vorticity
pvu	potential vorticity unit $[10^{-6} \text{ m}^2 \text{ s}^{-1} \text{ K kg}^{-1}]$
QQ-Plot	Quantile-Quantile Plot
RCM	Regional Climate Model
RV20	20-year return values
RV20nonstat	20-year return values for the non-stationary GEV distribution
RV20stat	20-year return values for the stationary GEV distribution
s.e.	standard error
SRES	Special Report on Emission Scenarios
T2MAX	daily 2-meter maximum temperature
T2MIN	daily 2-meter minimum temperature
TEMP2	daily mean 2-meter temperature
WMO	World Meteorological Organization
Z500	Geopotential height at 500m

Acknowledgements

Die gesamten Veröffentlichungen in der Publikationsreihe des MPI-M

„Berichte zur Erdsystemforschung",

„Reports on Earth System Science",

  ISSN 1614-1199

sind über die Internetseiten des Max-Planck-Instituts für Meteorologie erhältlich:

http://www.mpimet.mpg.de/wissenschaft/publikationen.html